Steady-state tokamak research: Core physics

M. Kikuchi*

Japan Atomic Energy Agency, 801-1 Mukoyama, 311-0193, Naka, Ibaraki, Japan

M. Azumi

AZM Techno Science Soft, Chitosedai-6, Setagaya, Tokyo, Japan

(published 28 December 2012)

Tokamaks have demonstrated excellent plasma confinement capability because of their symmetry but has an intrinsic drawback because of their pulsed inductive operation. Efforts have been made in the past 20 years to realize steady-state operation, the most successful utilizing a bootstrap current. In this review, progress in understanding tokamak physics related to steady-state operation is described to investigate the scientific feasibility of a steady-state tokamak fusion power system.

DOI: 10.1103/RevModPhys.84.1807 PACS numbers: 52.25.Fi, 52.55.Fa, 52.35.Ra, 52.30.Gz

CONTENTS

I. Introduction 1807
II. Magnetic Confinement Fusion 1808
A. Magnetic confinement topology 1808
B. Integrability and symmetry 1808
III. Steady-state Tokamak Regime 1809
A. Steady-state tokamak reactors 1809
B. Advanced tokamak research 1810
1. Weak-shear operation 1810
2. Negative-shear operation 1811
3. Current-hole operation 1812
IV. Parallel Transport in Tokamaks 1812
A. Collisional moment equation 1812
1. Moment equation 1812
2. Friction and viscous forces 1813
B. Current drive physics 1814
1. Generalized Ohm's law 1814
2. Electrical conductivity 1815
3. Bootstrap current 1815
4. Neutral beam current drive 1817
5. Electron cyclotron current drive 1818
C. Rotation physics 1820
1. Neoclassical rotations 1820
2. Neoclassical toroidal viscosity 1821
3. Intrinsic rotation 1822
V. Magnetohydrodynamics in the Advanced Tokamak Regime 1823
A. Progress in linear ideal magnetohydrodynamics 1823
1. Spectral properties in magnetohydrodynamics 1824
2. Two-dimensional Newcomb equation 1824
3. Flow effect on ideal magnetohydrodynamics 1825
B. Resistive magnetohydrodynamics 1826
1. Classical tearing mode 1826
2. Neoclassical tearing mode 1827
3. Double tearing mode 1828
4. Resistive wall modes 1830
C. Localized magnetohydrodynamics 1831
1. Infernal mode in advanced tokamak operation 1831
2. Peeling, ballooning, and edge localized modes 1833
3. Barrier localized mode 1835
D. Alfvén eigenmodes 1835
1. Shear Alfvén gap 1835
2. Stability of Alfvén eigenmodes 1836
3. Nonlinear Alfvén eigenmodes 1836
E. Stability of the current hole 1837
1. Equilibrium bifurcation 1837
2. Resistive stability and the β limit 1837
F. Magnetohydrodynamics summary 1838
VI. Perpendicular Transport in Tokamaks 1838
A. Turbulent transport 1838
1. Self-organized criticality 1838
2. Ion temperature gradient turbulence 1839
3. Electron temperature gradient turbulence 1842
4. Trapped-electron mode and multiscale turbulence 1844
5. Electromagnetic turbulence 1845
B. Transport barriers 1845
1. Turbulence suppression 1845
2. Edge and internal transport barriers 1846
VII. Control Issues of Advanced Tokamak Operation 1847
A. Density profile control 1847
B. Control of internal transport barrier strength 1848
C. Edge bootstrap current 1848
VIII. Summary 1848
List of Symbols and Abbreviations 1848
Appendix 1849
1. Friction and viscosity matrix 1849
2. Viscosity coefficients for fast ions 1849
Acknowledgments 1849
References 1850

I. INTRODUCTION

The tokamak (Artsimovich, 1972) is a front runner in fusion research. The tokamak has geometrical symmetry in the toroidal direction, which makes the nested flux surface robust against various changes of parameters, and good confinement, leading to the achievement of equivalent break-even conditions in large tokamaks such as JT-60U

*kikuchi.mitsuru@jaea.go.jp

(Kishimoto *et al.*, 2005) and JET (Keilhacker *et al.*, 2001), and significant deuterium-tritium (D-T) fusion power production (Hawryluk *et al.*, 1998). While the tokamak shows superiority in plasma confinement, its symmetry is created by inducing a current in the high-temperature plasma through transformer action. Therefore, the operation of the reactor becomes pulsed if we cannot develop efficient noninductive methods to sustain the plasma current. Since present power sources such as oil-, coal-, and natural-gas-fired and fission plants operate continuously, it is highly desirable for the tokamak reactor to be a steady-state power station.

The intriguing physical process called the bootstrap current can be utilized for steady-state operation of the tokamak (Bickerton *et al.*, 1971). Use of the bootstrap current is a fundamental requirement for the efficient steady-state operation of a tokamak reactor (Kikuchi, 1990a) and an operational scenario with a hollow current has been proposed (Ozeki *et al.*, 1993a; Kessel *et al.*, 1994). Since then, extensive research initiatives to advance the tokamak physics relevant for steady-state operation have been started in tokamak facilities such as JT-60U (Kikuchi *et al.*, 1995a), DIII-D (Stambaugh *et al.*, 1995), JET (Hugon *et al.*, 1992), and TFTR (Levinton *et al.*, 1995). Much experimental and theoretical work has appeared over the last two decades. Experiments at JET using D-T fuel also used an advanced scenario (JET team, 1997).

After a brief introduction to magnetic confinement in Sec. II, the steady-state tokamak reactor and advanced tokamak operating regimes are introduced in Sec. III. Section IV summarizes the parallel transport in a tokamak critical for steady-state operation. Ideal, resistive, and kinetic magnetohydrodynamic (MHD) instabilities related to a high bootstrap current fraction are described in Sec. V. The perpendicular transport in advanced tokamak (AT) regimes is described in Sec. VI and control issues for the AT operation in Sec. VII. Section VIII gives a summary. To keep the length of the article reasonable, we do not discuss divertor physics, which becomes more and more important in moving toward fusion energy production. The Appendix gives the normalized friction and viscosity matrices.

II. MAGNETIC CONFINEMENT FUSION

A. Magnetic confinement topology

In the natural fusion reactor the Sun, dense and hot plasma is confined by the gravitational field. This is a central force field and the force acts in the direction of the field line. For this reason, the confinement closed surface has the topology of a sphere. In a man-made fusion reactor, high-temperature plasma is confined by trapping charged particles with the Lorentz force in a magnetic field to sustain reaction in a volume of small dimension of 100 millionth of that of the Sun. This force acts in the direction perpendicular to the field line. For this reason, the confinement closed surface has the topology of a torus.

The French mathematician Henri Poincaré proved the theorem that a closed surface that can be covered with a vector field without a fixed point is restricted to a torus, which is called the "Poincaré theorem" (Poincaré, 1885) [see Kikuchi (2011b) for details]. The meaning of the Poincaré theorem is important. Consider the boundary surface of a magnetically confined plasma; the plasma will leak from the zero point of the magnetic field vector. The surface must be covered by a nonzero magnetic field to confine the hot plasma. This is why we use toroidal geometry for the magnetic confinement.

B. Integrability and symmetry

The magnetic field is characterized by its incompressibility ($\nabla \cdot \boldsymbol{B} = 0$). This leads to the existence of the vector potential $\boldsymbol{A}$ ($\nabla \times \boldsymbol{A} = \boldsymbol{B}$) given by $\boldsymbol{A} = \phi \nabla\theta - \psi\nabla\zeta + \nabla G$ (θ and ζ are arbitrary poloidal and toroidal angles, and G is a gauge term). This leads to the Hamiltonian structure for the magnetic field evolution in the toroidal direction ζ. The magnetic field line trajectory is given by $d\theta/d\zeta = \partial\psi/\partial\phi$, $d\phi/d\zeta = -\partial\psi/\partial\theta$ and can be regarded as a Hamilton equation if we regard ψ as the Hamiltonian, θ as the canonical coordinate, ϕ as the canonical angular momentum, and ζ as time (Cary *et al.*, 1983).

A variational principle of the field line is given by the analogy to the Hamiltonian action integral $S = \int L dt = \int [\boldsymbol{p} \cdot d\mathbf{x}/dt - H] dt$. By substituting the relationships $\boldsymbol{p} \rightarrow \phi$, $d\boldsymbol{x}/dt \rightarrow d\theta/d\zeta$, $H \rightarrow \psi$, and $t \rightarrow \zeta$, we have $S = \int [\phi d\theta/d\zeta - \psi] d\zeta$. So the Lagrangian of the magnetic field line becomes $L = \phi d\theta/d\zeta - \psi$ if we regard ζ as "time."

In plasma equilibrium, the plasma's expansion force ($-\nabla P$) is balanced by the Lorentz force ($\boldsymbol{J} \times \boldsymbol{B}$). In this case, the magnetic field $\boldsymbol{B}$ lies on the constant-pressure surface ($\boldsymbol{B} \cdot \nabla P = 0$) and the surface is called the "flux surface." This means that $\boldsymbol{B}$ is a linear combination of tangent vectors $\partial\boldsymbol{x}/\partial\theta$ and $\partial\boldsymbol{x}/\partial\zeta$ on the flux surface. The incompressibility condition of $\boldsymbol{B}$ leads to the existence of the flow function, and the coordinate transformation of θ by which $\boldsymbol{B}$ becomes a straight line gives a Clebsch form for the magnetic field $\boldsymbol{B} = \nabla\psi \times \nabla\alpha$, where $\alpha = q\theta - \zeta$ and $q = d\phi/d\psi$ is the safety factor (Boozer *et al.*, 2005). Then ϕ and ψ become $[1/2\pi]$ of the toroidal and poloidal fluxes inside the constant-P surface and $P = P(\psi)$. The coordinates (ϕ, θ, ζ) and (ψ, θ, ζ) are called flux coordinates. The Lagrangian of the magnetic field line becomes $L = \phi(d\theta/d\zeta) - \psi(\phi)$. The Lagrangian has no explicit dependence on the canonical coordinate θ nor on time ζ and they are ignorable coordinates. The existence of such ignorable coordinates is essential for plasma equilibrium.

The tokamak has geometrical symmetry in the toroidal direction, ensuring the existence of a flux surface under a wide range of operating conditions, whose poloidal cross section is shown in Fig. 1. The force balance equation in an axisymmetric torus leads to the so-called Grad-Shafranov equation (Shafranov, 1958) as follows:

$$\frac{\partial^2\psi}{\partial R^2} - \frac{1}{R}\frac{\partial\psi}{\partial R} + \frac{\partial^2\psi}{\partial^2 Z} = -\mu_0 R^2 \frac{dP}{d\psi} - F\frac{dF}{d\psi}. \tag{1}$$

Here $F = RB_\zeta$ where B_ζ is the toroidal component of the magnetic field, and $P(\psi)$ and $F(\psi)$ are functions of ψ and are called flux functions.

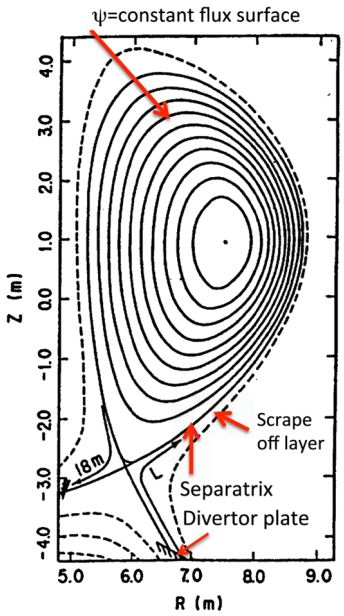

FIG. 1 (color online). Poloidal cross section of a tokamak with divertor. The plasma is vertically elongated and is also triangular.

III. STEADY-STATE TOKAMAK REGIME

A. Steady-state tokamak reactors

The observation of the large bootstrap current fraction up to 80% in JT-60 high-β_p discharges (Kikuchi, 1990b) in 1990 immediately stimulated the development of the concept of the steady-state tokamak reactor (SSTR) (Kikuchi, 1990a) and its design (Seki *et al.*, 1991a) to clarify the scientific and technical capabilities of electric power generation by a tokamak with minimum extrapolation from the knowledge at that time. Conn *et al.* (1991) also developed another power reactor study with more aggressive technical provisions, ARIES-I. The SSTR design whose layout is given in Fig. 2 was made with strong involvement of industry (Seki *et al.*, 1991b).

A major feature of the SSTR is the maximum utilization of the bootstrap current for efficient steady-state operation. Since the bootstrap current fraction is proportional to the poloidal beta $\beta_p = 4\int PdV/\mu_0 I_p^2 R_p$ [or $f_{\rm boot} \sim (a/R)^{0.5}\beta_p$], the reactor should operate in the high-β_p regime. An important constraint comes from the so-called Troyon scaling $\beta_t[\%] = 100\beta_N I_p[\mathrm{MA}]/a_p[\mathrm{m}]B_t[\mathrm{T}]$ (Troyon *et al.*, 1984), where

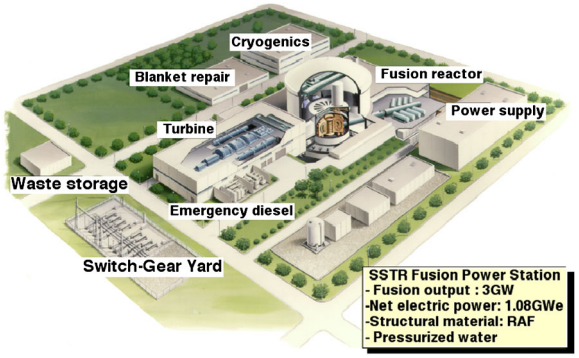

FIG. 2 (color online). Layout of steady-state tokamak reactor.

$\beta_t = \langle P\rangle/(B_t^2/2\mu_0)$ is the volume-averaged toroidal beta, I_p is the plasma current, a_p is the plasma horizontal minor radius, B_t is the toroidal magnetic field, and β_N is a constant called the normalized beta. The combination of Troyon scaling with the definition of the poloidal beta $\beta_p = 4\int PdV/\mu_0 I_p^2 R_p$ gives the relation between β_t and β_p as $\beta_t\beta_p = \kappa\beta_N^2/4$, where κ is the vertical plasma elongation. This scaling is confirmed in DIII-D (Stambaugh *et al.*, 1985).

Figure 3 shows the (β_t, β_p) diagram. The curve corresponds to $\beta_N = 3.5$ and $\kappa = 1.8$, in which the steady-state fusion power concepts SSTR and ARIES-I ($\beta_p = 2$–2.1) as well as the current ITER steady-state design ($\beta_p \sim 1.5$) adopt high-β_p operation to increase the bootstrap current fraction. Since $\beta_p \sim 1/\beta_t$ for fixed β_N and κ, the steady-state tokamak reactor should sacrifice β_t to achieve high β_p and hence a high bootstrap current fraction.

When the SSTR and ARIES-I concepts were proposed in 1990, world fusion research was directed toward increasing the plasma current to improve energy confinement, an effort typically represented by the design change from the International Tokamak Reactor to the ITER-CDA (where CDA indicates conceptual design activity). Also the research frontier was directed toward achieving a high-β_t value close to 10% with high normalized current $I_p/a_p B_t$ in DIII-D (Ferron *et al.*, 1990). If we are searching for a steady-state tokamak reactor, it is evident that we have to change our research direction from low-q and high-β_t to high-q and high-β_p research.

This change in the research direction was proposed (Kikuchi *et al.*, 1991) as joint work between SSTR and ARIES-I design activities. The SSTR design is based on current profile control with elevated central q (q_0) to suppress sawtooth oscillations and improve stability against ballooning modes and wall stabilization against kink modes, while ARIES-I optimizes the current profile without wall stabilization, resulting in modest enhancement of q_0. This is called the weak-shear (WS) scenario. Here shear is given by $s = R(dq/dr)/q$.

Ozeki *et al.* (1993a) proposed to utilize a hollow current profile which is a natural current profile with a bootstrap

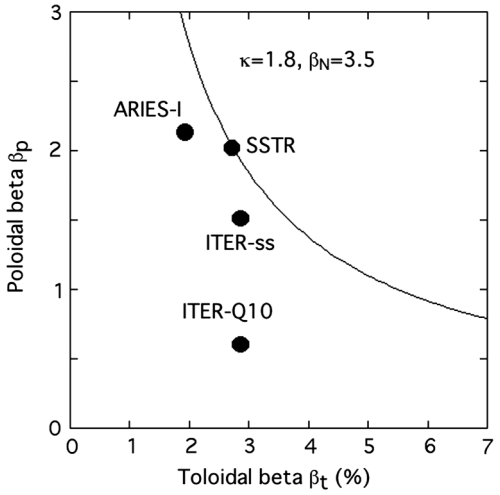

FIG. 3. (β_t, β_p) diagram and operating points of ITER, SSTR, and ARIES-I. ITER-Q10 stands for an inductive operation, and ITER-ss stands for a steady-state operation.

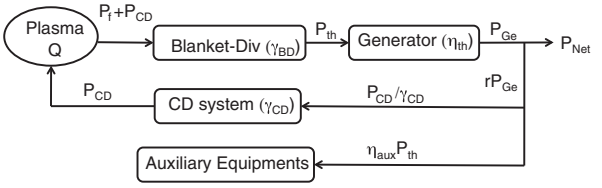

FIG. 4. Energy flow diagram of steady-state tokamak reactor. The plant efficiency $\eta_{\rm plant} = P_{\rm net}/P_{\rm th}$, and the ratio of net electric power output to thermal power output is given by $\eta_{\rm plant} = \eta_{\rm th} - \eta_{\rm aux} - 1/\gamma_{CD}\gamma_{BD}(1+Q)$.

current and is now called the negative-shear (NS) scenario. The effectiveness of the NS scenario was also investigated by Kessel *et al.* (1994). Later, tokamak reactor concepts based on NS scenarios were developed in the United States, ARIES-RS (Najmabadi *et al.*, 1998), and in Japan, CREST (Okano *et al.*, 1998).

Reactor power balance is an important aspect in the steady-state tokamak reactor. The useful-energy flow diagram is shown in Fig. 4. Here P_f is the fusion power from plasma, $P_{\rm CD}$ is the heating and current drive (CD) power, Q is the energy gain of the confined plasma, $Q = P_f/P_{\rm CD}$, $\gamma_{\rm BD}$ is the energy multiplication factor in the blanket-divertor system, $P_{\rm Ge}$ is the gross electric power, $P_{\rm net}$ is the net electric power to the grid, $rP_{\rm Ge}$ is the recirculating power (r is the recirculating power fraction), $\gamma_{\rm CD}$ is the overall efficiency of the CD system, and $\eta_{\rm aux}P_{\rm th}$ is the power required for auxiliary equipment. The thermal conversion efficiency $\eta_{\rm th}$ is 0.345 for water cooling in the fission light-water reactor, while it is 0.49 for the advanced high-temperature He cooling system. $\eta_{\rm aux}$ is the reduction of plant efficiency due to auxiliary equipment and is in the range 0.03–0.06 depending on the coolant.

The ($\eta_{\rm plant}$, Q) diagram is shown in Fig. 5 for pressurized-water cooling and high-temperature helium gas cooling. It must be noted that $\eta_{\rm plant}$ depends weakly on Q around $Q =$ 30–50; $\eta_{\rm plant} \sim 0.3$ for pressurized water, and $\eta_{\rm plant} \sim 0.4$ for high-temperature helium. It is difficult to achieve the required Q level of $Q =$ 30–50 by using only a noninductive current drive by external means. This is a fundamental reason why we have to utilize a bootstrap current to realize efficient steady-state operation of the tokamak reactor.

Current drive by noninductive means such as neutral beam CD (NBCD), electron cyclotron CD (ECCD), lower hybrid

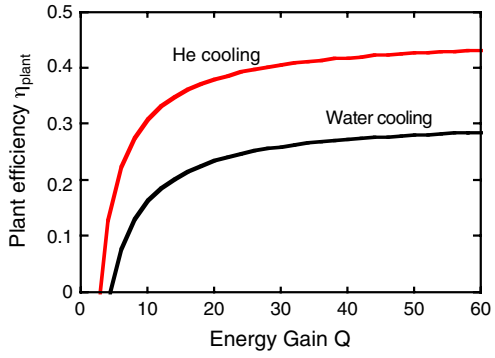

FIG. 5 (color online). The plant efficiency ($\eta_{\rm plant}$) as a function of plasma energy gain (Q) for He-cooled and water-cooled systems in the steady-state tokamak reactor.

CD (LHCD), and fast-wave CD (FWCD) has been developed (Fisch *et al.*, 1987). The efficiency of the noninductive CD is expressed by the CD efficiency $\eta_{\rm CD}$ defined as $\eta_{\rm CD} = I_p^{\rm CD}R_p\langle n_e\rangle/P_{\rm CD}$ and has certain limits, $\eta_{\rm CD} \sim 5 \times 10^{19}$ A/W m^2 for N-NBI (negative-ion-based NBI) at $\langle T_e\rangle =$ 17 keV and $E_{\rm beam} = 2$ MeV, which is much lower than that of inductive CD.

B. Advanced tokamak research

After the development of the basic concepts of the WS and NS operational scenarios during 1990–1992, a reviews of the prospects for steady-state tokamak reactors were given by Kikuchi (1993) with an emphasis on the importance of current profile control and by Goldston *et al.* (1994) on the requirements of a superconducting advanced tokamak device, which was later built in Korea as the KSTAR tokamak (Kwon *et al.*, 2011) and in China as the EAST tokamak (Li *et al.*, 2011). The first systematic experimental studies addressing steady-state tokamak regimes were reported in 1994 from JT-60U (Kikuchi *et al.*, 1995a) and from DIII-D (Stambaugh *et al.*, 1995). Since then, steady-state tokamak research has been called advanced tokamak research. Reviews of advanced tokamak research have been given by Taylor *et al.* (1997), Gormezano *et al.* (2004), and Kishimoto *et al.* (2005).

1. Weak-shear operation

To compensate the hollow bootstrap current profile [$J_{\rm bs} \sim \sqrt{r/R}(dP/dr)/B_p$], an active central current drive is essential to achieve a monotonically increasing q profile. An active central current drive can be produced by either NBCD, ECCD, or FWCD.

Figure 6 shows a WS profile using central NBCD for the SSTR (Kikuchi, 1993). The ballooning mode becomes stable when $q(0)$ becomes higher than 2. While global magnetic shear is weak in such a case, local shear has a stabilizing effect (Seki *et al.*, 1987). Ideal MHD stability calculations using the ERATO-J code show that $n = 1$, 2, and 3. Ideal MHD modes also become stable with increasing $q(0)$ above 2 if the wall stabilization is effective at $r_{\rm wall}/a = 1.2$, as shown in Fig. 6. The effectiveness of this wall stabilization for the steady-state tokamak operation is discussed in Sec. V.

While the WS scenario with $q(0) > 2$ is effective in enhancing the beta limit with wall stabilization, the ideal MHD stability limit without wall stabilization is reduced with increasing $q(0)$ [$\beta_N \sim 1/q(0)$] (Ramos, 1991). So it is reasonable to stay at $q(0) \geq 1$ to ensure stability in the case of the loss of wall stabilization, as shown in Fig. 7. While $\beta_N \sim 4$ is stable with wall stabilization, the bootstrap current fraction stays at 0.4. Without wall stabilization, the stability limit is $\beta_N \sim 3.5$. All these scenarios are based on smooth pressure profiles without a local transport barrier. The formation of edge and internal transport barriers brings other issues associated with excitation of localized bootstrap currents, which will be discussed in Sec. V.

This WS regime has been investigated in many tokamaks and called by different names, such as the high-β_p regime (Ishida *et al.*, 1992) and the high-β_p H-mode regime (Koide *et al.*, 1994) at JT-60, the supershot regime at TFTR (Strachan

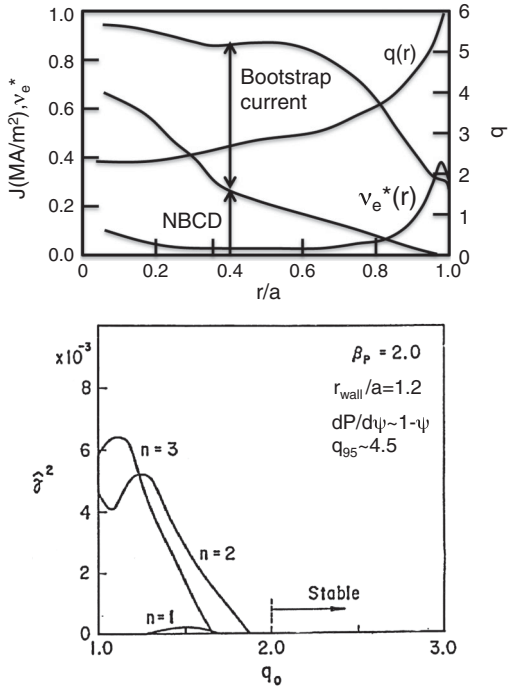

FIG. 6. WS profiles using central NBCD and $n = 1$, 2, and 3 ideal MHD stability as a function of the central safety factor q_0 for the SSTR. From Kikuchi, 1993.

et al., 1987), the improved H mode in the ASDEX Upgrade (Sips *et al.*, 2002), the optimized shear regime at JET (Gormezano *et al.*, 1999; Pietrzyk *et al.*, 2001), and the hybrid regime at DIII-D (Luce *et al.*, 2003). In these regimes, improved core confinement is observed with sawtooth suppression and an internal transport barrier (ITB).

2. Negative-shear operation

Ozeki *et al.* (1993a) showed, for the first time, that a hollow current profile with a reduced pressure gradient near $q_{\min}$ can be stable to ideal MHD modes; this is called NS operation. Since the bootstrap current profile is hollow, it is much easier to use a hollow current profile to minimize active current drive. Since shear plays an important role in stabilizing pressure-driven ideal MHD modes, a reduced pressure gradient near $q_{\min}$ is important for the NS scenario. A low-pressure gradient near $q_{\min}$ means that the bootstrap current is low. So it becomes essential to drive the plasma current noninductively near the pitch minimum location. These authors proposed to use off-axis NBCD to realize a negative-shear profile, as shown in Fig. 8.

Manickam *et al.* (1994) showed that the beta limit in NS is fairly low, $\beta_N = 2$, without wall stabilization and quite high, $\beta_N = 5$, with wall stabilization, as shown in Fig. 9. The reason for this is quite simple: wall stabilization is easier if the current is closer to the wall, but such a surface current is unstable if the wall is not effective. This result implies that wall stabilization should be securely maintained in the reactor by a combination of rotational stabilization and feedback stabilization.

This NS regime has been investigated in many tokamaks such as the enhanced reversed shear (ERS) regime in TFTR (Levinton *et al.*, 1995) and the negative central shear regime in DIII-D (Strait *et al.*, 1995), the reversed shear regime in JT-60 (Fujita *et al.*, 1997a, 1997b), and the stationary magnetic shear reversal regime in Tore-Supra (Litaudon *et al.*, 1996). In these regimes, very high confinement is observed with strong ITB. The key issue is control of the transport to match the optimum stable pressure profile to the

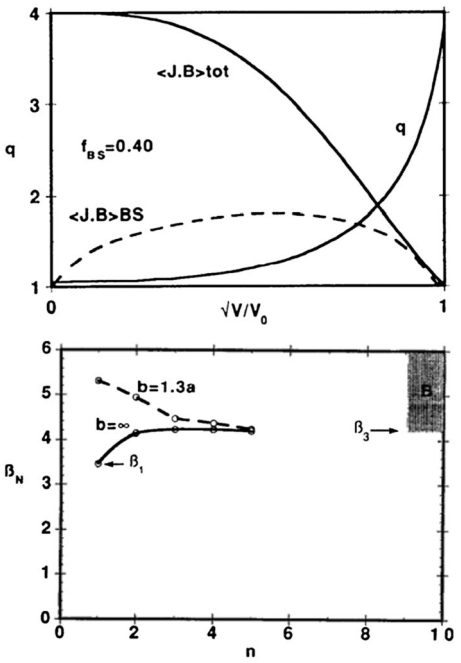

FIG. 7. WS profile and ideal β_N limits with and without wall stabilization. From Manickam *et al.*, 1994.

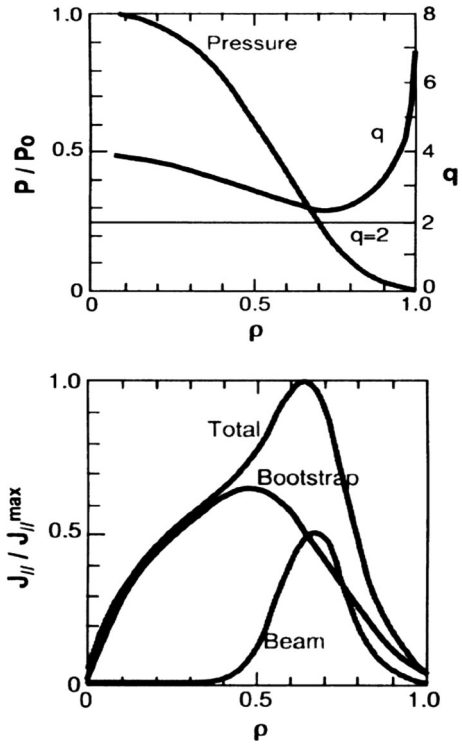

FIG. 8. Negative-shear scenario for the SSTR, where off-axis NBCD is used. From Ozeki *et al.*, 1993a.

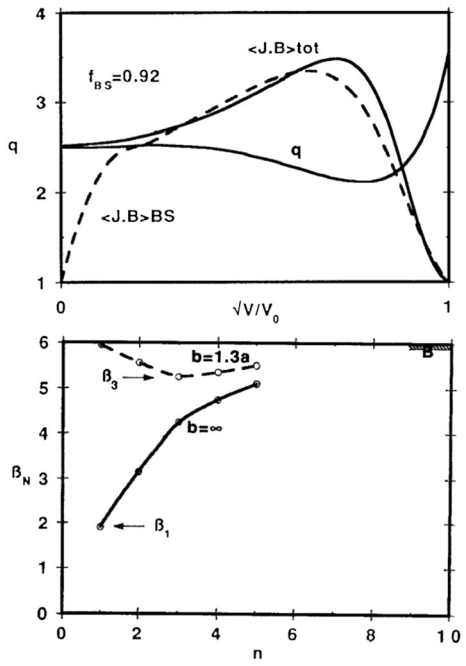

FIG. 9. Negative-shear plasma profile and ideal MHD stability limit with and without wall stabilization. From Manickam *et al.*, 1994.

high-β_N operation. A large-radius ITB is sustained by LHCD in the JET optimized shear (Mailloux *et al.*, 2002). Access to stable high β_N in the current ramp-up phase is also an important issue, especially when $q_{\min}$ changes above to below a low m/n rational value in avoiding kink ballooning and double tearing modes (TMs) (see Sec. V.B.3). At low β, stationary long-pulse operation (van Houtte *et al.*, 2004) is achieved and a stationary oscillating mode, called the *O* mode (Giruzzi *et al.*, 2003), is observed at the Tore-Supra tokamak.

3. Current-hole operation

An extreme situation in NS configuration, equilibrium with zero plasma current in the central regime called the current hole (CH) (see Fig. 10), was formed at JT-60U (Fujita *et al.*, 2001) and JET (Hawkes *et al.*, 2001). Although the core confinement inside the CH is poor (almost no confinement),

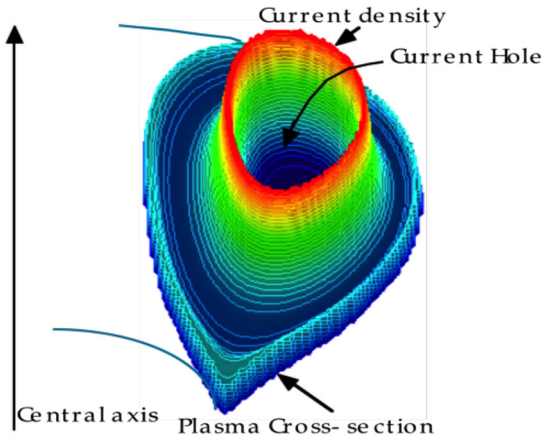

FIG. 10 (color online). Current hole equilibrium.

an ITB is formed just outside the CH, showing good confinement close to ion neoclassical transport (Hayashi *et al.*, 2005; Takizuka *et al.*, 2002). The whole global energy confinement is quite good, $HH_{y2} = 1.16$–1.45 at JT-60U (Fujita *et al.*, 2001). Here HH_{y2} is defined as the enhancement factor of the plasma energy confinement time over that of the ITER *H*-mode scaling law, called IPB98(y, 2) (ITER Physics Expert Group, 1999) and $HH_{y2} = 1$ corresponds to the ITER standard operation based on the *H* mode (Wagner *et al.*, 1982). This CH regime can be stably sustained for several seconds. This regime is interesting from the control viewpoint because it has low l_i and makes it easier to obtain a positionally stable elongated plasma and also to obtain a high bootstrap current fraction. On the other hand, the CH regime will be subject to higher ripple loss of α particles in future reactors and sets severe constraints on maximum toroidal field ripple as well as a low no-wall beta limit similar to that in the reversed shear regime. The CH operation was extensively reviewed by Fujita *et al.* (2010).

IV. PARALLEL TRANSPORT IN TOKAMAKS

Collisional parallel-transport physics plays an essential role in current and rotation drives for the steady-state tokamak reactor. Reviews of neoclassical transport have been given by Hinton *et al.* (1976) and Hirshman *et al.* (1981). Noninductive current drive theory and ideas are reviewed by Fisch *et al.* (1987). Since then, experimental demonstration of neoclassical parallel-transport theories has been made, notably on bootstrap current, as reviewed by Kikuchi *et al.* (1995b). Many experiments followed to validate neoclassical parallel transport. With the recent increased interest in intrinsic toroidal rotation (Rice *et al.*, 2007), an explanation of the hidden torque source has been developed by identifying symmetry breaking in turbulent momentum transport as well as neoclassical effects on toroidal rotation.

A. Collisional moment equation

1. Moment equation

The high-temperature plasma in present-day and future tokamak reactors consists of a Maxwellian electron, ion, and impurity, and a fast ion from NB heating and fusion α. Hirshman *et al.* (1981) developed moment equations for the thermal species, while Azumi *et al.* (1990) and Wang *et al.* (1994) investigated the fast-ion effect in the moment equations. The flux surface-averaged parallel-momentum and heat-flux balance equations for the thermal electron (e), ion (i), impurity (I), and fast ion (f) are given as follows:

$$\langle \boldsymbol{B}\cdot\nabla\cdot\boldsymbol{\Pi}_a\rangle = \langle \boldsymbol{B}\cdot\boldsymbol{F}_{a1}\rangle + e_a n_a\langle \boldsymbol{B}\cdot\boldsymbol{E}\rangle + \langle \boldsymbol{B}\cdot\boldsymbol{M}_a\rangle, \tag{2}$$

$$\langle \boldsymbol{B}\cdot\nabla\cdot\boldsymbol{\Theta}_a\rangle = \langle \boldsymbol{B}\cdot\boldsymbol{F}_{a2}\rangle + \langle \boldsymbol{B}\cdot\boldsymbol{Q}_a\rangle. \tag{3}$$

Here $\boldsymbol{\Pi}_a$, $\boldsymbol{F}_{a1}$, e_a, n_a, $\boldsymbol{E}$, $\boldsymbol{M}_a$, $\boldsymbol{\Theta}_a$, $\boldsymbol{F}_{a2}$, and $\boldsymbol{Q}_a$ are the viscosity tensor, friction force, electric charge, density, electric field, momentum source, heat viscosity tensor, heat friction force, and heat source, respectively, and a stands for species $a = e, i, I$, and f. The heat-flow balance equation (3) is not considered for the fast ion (Kikuchi *et al.*, 1995b). The viscosity and heat

viscosity tensors are related to the pressure anisotropy in a Chew-Goldberger-Low form (Chew *et al.*, 1956) as $\boldsymbol{\Pi}_a = (P_{\|a} - P_{\perp a})(\boldsymbol{bb} - \frac{1}{3}\boldsymbol{I})$ and $\boldsymbol{\Theta}_a = (\Theta_{\|a} - \Theta_{\perp a})(\boldsymbol{bb} - \frac{1}{3}\boldsymbol{I})$. Here $P_{\|a}$, $P_{\perp a}$, $\Theta_{\|a}$, and $\Theta_{\perp a}$ are the parallel pressure, perpendicular pressure, parallel and perpendicular components of heat viscosity, respectively. Also, $\boldsymbol{b}$ and $\boldsymbol{I}$ are a unit vector along the magnetic field and a unit tensor, respectively.

The first-order flows of species a are given by

$$\boldsymbol{u}_a^{(1)} = u_{\|a}\boldsymbol{b} + \boldsymbol{u}_{\perp a}^{(1)}, \qquad \boldsymbol{q}_a^{(1)} = q_{\|a}\boldsymbol{b} + \boldsymbol{q}_{\perp a}^{(1)}, \tag{4}$$

where $u_{\|a}\boldsymbol{b}$ and $q_{\|a}\boldsymbol{b}$ are the parallel flows and $\boldsymbol{u}_{\perp a}^{(1)}$ and $\boldsymbol{q}_{\perp a}^{(1)}$ are the perpendicular flows as given by

$$\boldsymbol{u}_{\perp a}^{(1)} = \frac{BV_{1a}}{F}\frac{\nabla\psi \times \boldsymbol{b}}{B}, \tag{5}$$

$$\boldsymbol{q}_{\perp a}^{(1)} = \frac{5P_a}{2}\frac{BV_{2a}}{F}\frac{\nabla\psi \times \boldsymbol{b}}{B}. \tag{6}$$

Here $BV_{1a} = -F[d\Phi/d\psi + (1/e_a n_a)dP_a/d\psi]$ and $BV_{2a} = -(F/e_a)dT_a/d\psi$ are thermodynamic forces and $F(\psi) = RB_\zeta$. Considering the poloidal flow in the unit flux tube, we find that the poloidal components of flows over the poloidal magnetic field are the flux functions,

$$\hat{u}_{a\theta}(\psi) = \frac{\boldsymbol{u}_a^{(1)} \cdot \nabla\theta}{\boldsymbol{B} \cdot \nabla\theta}, \qquad \hat{q}_{a\theta}(\psi) = \frac{\boldsymbol{q}_a^{(1)} \cdot \nabla\theta}{\boldsymbol{B} \cdot \nabla\theta}. \tag{7}$$

From the scalar product of Eq. (4) with $\nabla\theta$, we obtain relations among poloidal, parallel, and diamagnetic flows as

$$B^2\hat{u}_{a\theta}(\psi) = Bu_{\|a} - BV_{1a}, \tag{8}$$

$$B^2\frac{2\hat{q}_{a\theta}(\psi)}{5P_a} = B\frac{2q_{\|a}}{5P_a} - BV_{2a}. \tag{9}$$

Substituting the axisymmetric relation $\boldsymbol{b} \times \nabla\psi = F\boldsymbol{b} - R^2B\nabla\zeta$ into Eq. (6), the first-order flow relation (4) is transformed into the following form by using Eqs. (8) and (9):

$$\boldsymbol{u}_a^{(1)} = \hat{u}_{a\theta}(\psi)\boldsymbol{B} + \frac{BV_{1a}}{F}R^2\nabla\zeta, \tag{10}$$

$$\boldsymbol{q}_a^{(1)} = \hat{q}_{a\theta}(\psi)\boldsymbol{B} + \frac{5P_a}{2}\frac{BV_{2a}}{F}R^2\nabla\zeta. \tag{11}$$

Taking the toroidal (ζ) component of Eqs. (10) and (11) and using the flux surface average of Eqs. (8) and (9), we obtain the following equations for the toroidal flows:

$$u_{a\zeta}^{(1)} = \frac{B_\zeta}{\langle B^2\rangle}\langle Bu_{\|a}\rangle + \left[1 - \frac{B_\zeta^2}{\langle B^2\rangle}\right]\frac{BV_{1a}}{B_\zeta}, \tag{12}$$

$$q_{a\zeta}^{(1)} = \frac{B_\zeta}{\langle B^2\rangle}\langle Bq_{\|a}\rangle + \frac{5P_a}{2}\left[1 - \frac{B_\zeta^2}{\langle B^2\rangle}\right]\frac{BV_{2a}}{B_\zeta}. \tag{13}$$

Here the second terms on the right-hand side are called the Pfirsch-Schlüter terms.

2. Friction and viscous forces

The flux surface-averaged parallel viscous forces $\langle \boldsymbol{B} \cdot \nabla \cdot \boldsymbol{\Pi}_a \rangle$ and $\langle \boldsymbol{B} \cdot \nabla \cdot \boldsymbol{\Theta}_a \rangle$ and the friction forces $\langle \boldsymbol{B} \cdot \boldsymbol{F}_{a1} \rangle$ and $\langle \boldsymbol{B} \cdot \boldsymbol{F}_{a2} \rangle$ are related to the first-order flows. The friction forces are given as follows:

$$\begin{bmatrix} \langle \boldsymbol{B} \cdot \boldsymbol{F}_{a1} \rangle \\ \langle \boldsymbol{B} \cdot \boldsymbol{F}_{a2} \rangle \end{bmatrix} = \frac{m_a n_a}{\tau_{aa}} \sum_b \begin{bmatrix} \hat{l}_{11}^{ab} & -\hat{l}_{12}^{ab} \\ -\hat{l}_{21}^{ab} & \hat{l}_{22}^{ab} \end{bmatrix} \begin{bmatrix} \langle Bu_{\|a} \rangle \\ \frac{2\langle Bq_{\|a}\rangle}{5P_a} \end{bmatrix}. \tag{14}$$

Here $\hat{l}_{ij}^{ab} = (\tau_{aa}/m_a n_a) l_{ij}^{ab}$ is the normalized friction coefficient. The l_{ij}^{ab} for thermal species and those between the fast-ion and thermal species are given in the Appendix.

The parallel viscous force is related to the poloidal flow since viscous force operates when the particle moves poloidally in response to the variation of the toroidal magnetic field,

$$\begin{bmatrix} \langle \boldsymbol{B} \cdot \nabla \cdot \boldsymbol{\Pi}_a \rangle \\ \langle \boldsymbol{B} \cdot \nabla \cdot \boldsymbol{\Theta}_a \rangle \end{bmatrix} = \frac{m_a n_a \langle B^2 \rangle}{\tau_{aa}} \begin{bmatrix} \hat{\mu}_{a1} & \hat{\mu}_{a2} \\ \hat{\mu}_{a2} & \hat{\mu}_{a3} \end{bmatrix} \begin{bmatrix} \hat{u}_{a\theta} \\ \frac{2\hat{q}_{a\theta}}{5P_a} \end{bmatrix}. \tag{15}$$

Here $\hat{\mu}_{ai} = (\tau_{aa}/m_a n_a)\mu_{ai}$ is the normalized viscosity coefficient. While early neoclassical transport theory is based on the variational method to obtain transport coefficients numerically (Hinton *et al.*, 1976), a novel method to obtain an analytical transport coefficient (such as that for the parallel viscosity) is developed by Tsang *et al.* (1976) using a model Coulomb collision operator. The basic idea is to divide velocity space into Pfirsh-Schlüter, plateau, banana, and boundary layers to obtain the transport coefficients so that the transport coefficients are given by a velocity space integral. This method was further improved by Hirshman *et al.* (1977) utilizing an analytically tractable approximate Coulomb collision operator, which conserves energy and momentum (Hirshman *et al.*, 1976). Later Shaing *et al.* (1996) gave an improved viscosity coefficient, which is implemented in the NCLASS package (Houlberg *et al.*, 1997).

Substituting these formulas for the viscosity and friction coefficients into Eqs. (2) and (3) and using Eqs. (8) and (9) the following balance equations for the friction and viscous forces are obtained:

$$\begin{aligned} &\begin{bmatrix} \hat{\mu}_{a1} & \hat{\mu}_{a2} \\ \hat{\mu}_{a2} & \hat{\mu}_{a3} \end{bmatrix} \begin{bmatrix} \langle Bu_{\|b} \rangle - BV_{1a} \\ \left\langle B\frac{2q_{\|b}}{5P_b} \right\rangle - BV_{2a} \end{bmatrix} \\ &\quad = \frac{\tau_{aa}}{m_a n_a} \begin{bmatrix} \langle BM_{\|a} \rangle \\ \langle BQ_{\|a} \rangle \end{bmatrix} + \sum_b \begin{bmatrix} \hat{l}_{11}^{ab} & -\hat{l}_{12}^{ab} \\ -\hat{l}_{21}^{ab} & \hat{l}_{22}^{ab} \end{bmatrix} \begin{bmatrix} \langle Bu_{\|b} \rangle \\ \left\langle B\frac{2q_{\|b}}{5P_b} \right\rangle \end{bmatrix} \\ &\qquad + \frac{e_a \tau_{aa}}{m_a} \begin{bmatrix} \langle BE_\| \rangle \\ 0 \end{bmatrix}. \end{aligned} \tag{16}$$

Here $M_{\|a}$ and $Q_{\|a}$ are the parallel momentum source and parallel heat source, respectively. If we write Eq. (16) for the electron, ion, impurity, and fast ion (only momentum balance is considered for the fast ion since heat flow by the fast ion is comparatively small), we obtain the following system of linear equations:

$$\hat{\boldsymbol{M}}(\boldsymbol{U}_\| - \boldsymbol{V}_\perp) = \hat{\boldsymbol{L}}\boldsymbol{U}_\| + \hat{\boldsymbol{E}} + \hat{\boldsymbol{S}}_\|, \tag{17}$$

where $\hat{\boldsymbol{M}}$ is the normalized viscosity matrix, $\hat{\boldsymbol{L}}$ is the normalized friction matrix, $\boldsymbol{U}_\|$ is the parallel flow vector, $\boldsymbol{V}_\perp$ is the thermodynamic force vector, $\hat{\boldsymbol{E}}$ is the electric field acceleration vector, and $\hat{\boldsymbol{S}}_\|$ is the parallel source vector.

The normalized friction and viscosity matrices are given in the Appendix. Using Eq. (17), we obtain the following expressions for parallel flow:

$$\langle \boldsymbol{B}\cdot\boldsymbol{u}_a\rangle = \sum_{b=1}^{4}\frac{e_b\tau_{bb}\hat{c}_{ab}}{m_b}\langle \boldsymbol{B}\cdot\boldsymbol{E}\rangle + \sum_{b=1}^{7}\left[\hat{\alpha}_{ab}V_{\perp b}+\frac{\tau_{bb}\hat{c}_{ab}}{m_b n_b}\hat{S}_{\|b}\right], \tag{18}$$

$$\hat{\boldsymbol{\alpha}} = (\hat{\boldsymbol{M}}-\hat{\boldsymbol{L}})^{-1}\hat{\boldsymbol{M}}, \tag{19}$$

$$\hat{\boldsymbol{c}} = (\hat{\boldsymbol{M}}-\hat{\boldsymbol{L}})^{-1}. \tag{20}$$

Equation (18) is important to obtain the generalized Ohm's law in the next section and also the relation between poloidal and toroidal rotations.

Here we explain the physical picture of the parallel viscous force. Distortion of the velocity distribution function occurs in collisionless plasma. The origin of this velocity space anisotropy is explained in the case of the electron in Fig. 11 (Kikuchi *et al.*, 1995b). The magnetic moment μ is conserved in high-temperature plasma when the electron moves along the magnetic field. So the orbit of the electrons satisfying $B_{\max}\geq E/\mu$ is trapped in the weak-magnetic-field regime reflected by the magnetic mirror (the trapped-particle orbit, also called the banana orbit because of its shape). When density is decreasing toward the outside ($dn/dr<0$) consider the velocity distribution function on a magnetic surface. There are fewer $v_\|>0$ trapped electrons since this trapped electron comes from radially outside, while there are more $v_\|<0$ trapped electrons since this trapped electron comes from radially inside. Meanwhile, the orbit of untrapped electrons stays much closer to the magnetic surface and the number of electrons for $v_\|>0$ is roughly equal to that for $v_\|<0$. Then there appears a discontinuity in the trapped-untrapped boundary of the velocity distribution function. Small Coulomb collisions smooth this gap and cause the particle diffusion in the velocity space. This collisional diffusion in velocity space acts as a viscous force in the magnetic field direction. In Fig. 11, the electron distribution function is drifting in the direction of $v_\|<0$, while the ion velocity distribution function is drifting in the direction of $v_\|>0$. This change in drift direction can be understood from the conservation of canonical angular momentum $P_{\zeta a}=eZ_aRA_\zeta+m_aRv_{a\zeta}$ since the field momentum changes sign for electrons and ions. This produces a noninductive plasma current, which is called the bootstrap current.

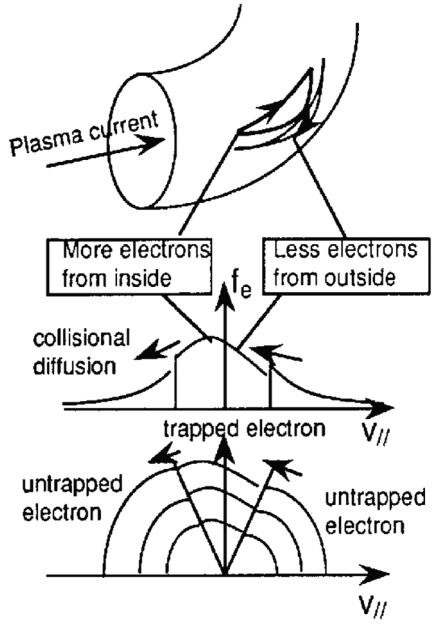

FIG. 11. Distortion of velocity distribution function in collisionless tokamak. From Kikuchi *et al.*, 1995b.

B. Current drive physics

1. Generalized Ohm's law

Using Eq. (18), we can calculate the flux surface-averaged parallel current density as follows:

$$\langle \boldsymbol{B}\cdot\boldsymbol{J}\rangle = \sum_a e_a n_a\langle \boldsymbol{B}\cdot\boldsymbol{u}_a\rangle = \langle \boldsymbol{B}\cdot\boldsymbol{J}\rangle_{\rm Oh}+\langle \boldsymbol{B}\cdot\boldsymbol{J}\rangle_{\rm bs}+\langle \boldsymbol{B}\cdot\boldsymbol{J}\rangle_{\rm ni}, \tag{21}$$

where "Oh," "bs," and "ni" are abbreviations for the Ohmic current, the bootstrap current, and the noninductive current, respectively,

$$\langle \boldsymbol{B}\cdot\boldsymbol{J}\rangle_{\rm Oh} = \sum_{a,b=1}^{4}\frac{n_a e_a e_b\tau_{bb}}{m_b}\hat{c}_{ab}\langle \boldsymbol{B}\cdot\boldsymbol{E}\rangle, \tag{22}$$

$$\langle \boldsymbol{B}\cdot\boldsymbol{J}\rangle_{\rm bs} = \sum_{a=1}^{4}e_a n_a\sum_{b=1}^{7}\hat{\alpha}_{ab}V_{\perp b}, \tag{23}$$

$$\langle \boldsymbol{B}\cdot\boldsymbol{J}\rangle_{\rm ni} = \sum_{a=1}^{4}\sum_{b=1}^{7}\frac{n_a e_a\tau_{bb}}{m_b n_b}\hat{c}_{ab}\hat{S}_{\|b}. \tag{24}$$

Equation (21) is called the generalized Ohm's law. Using Eq. (12), the local toroidal current density is given by

$$J_\zeta = \frac{B_\zeta}{\langle B^2\rangle}\langle BJ_\|\rangle+\left[1-\frac{B_\zeta^2}{\langle B^2\rangle}\right]R\frac{dP}{d\psi}. \tag{25}$$

Then the flux surface-averaged toroidal current density $J_\zeta(\rho)=\langle J_\zeta/R\rangle/\langle 1/R\rangle$ is given by

$$J_\zeta(\rho) = J_{\zeta\rm Oh}+J_{\zeta\rm bs}+J_{\zeta\rm ni}+J_{\zeta\nabla P}, \tag{26}$$

$$J_{\zeta s} = \frac{\langle B_\zeta/R\rangle}{\langle B^2\rangle\langle 1/R\rangle}\langle \boldsymbol{B}\cdot\boldsymbol{J}\rangle_s \qquad (s=\text{Oh, bs, ni}), \tag{27}$$

$$J_{\zeta\nabla P} = -\frac{\langle B_\theta^2\rangle dP/d\psi}{\langle B^2\rangle\langle 1/R\rangle}. \tag{28}$$

Here we used $B^2=B_\zeta^2+B_\theta^2$. The new term $J_{\zeta\nabla P}$ comes from the Pfirsch-Schlüter term [the last term on the right-hand side of Eq. (25)] and is important for low-aspect-ratio tokamaks where the poloidal field becomes comparable to the toroidal field.

2. Electrical conductivity

The generalized Ohm's law (21) includes current induced by the parallel electric field (22). A theoretical expression for the electrical conductivity in fully ionized plasma has been obtained by Spitzer (1962) and is called the "Spitzer conductivity." A key observation is the importance of electron-electron collisions as well as electron-ion collisions, which almost double the electrical conductivity. In a high-temperature plasma such as a tokamak, there is an important modification to the electrical conductivity due to the parallel viscosity (trapped-particle effect), called neoclassical (NC) conductivity. From Eq. (22), we obtain the following form of the electrical conductivity in tokamak geometry:

$$\sigma_{\parallel}^{\mathrm{NC}} = \sum_{a,b=1}^{4} \frac{n_a e_a e_b \tau_{bb}}{m_b} (\hat{\boldsymbol{M}} - \hat{\boldsymbol{L}})^{-1}_{ab}. \tag{29}$$

Here $\hat{\boldsymbol{L}}$ represents the collisional friction forces among various species, and $\hat{\boldsymbol{M}}$ represents the effect of trapped particles. This summation is dominated by the electron term due to the $1/\sqrt{m_b}$ mass dependence of τ_{bb}/m_b. If there are no trapped particles, the viscosity matrix $\hat{\boldsymbol{M}} = 0$ and conductivity σ are given in this case as follows:

$$\sigma_{\parallel}^{\mathrm{Spitzer}} = -\sum_{a,b=1}^{4} \frac{n_a e_a e_b \tau_{bb}}{m_b} \hat{\boldsymbol{L}}^{-1}_{ab}. \tag{30}$$

Equation (30) corresponds to the Spitzer conductivity. The electrical conductivity (29) is reduced due to the viscosity $\hat{\boldsymbol{M}}$, which becomes significant in the collisionless regime. In large tokamaks such as JT-60 (Kishimoto *et al.*, 2005), JET (Keilhacker *et al.*, 2001), and TFTR (Hawryluk *et al.*, 1998), it is possible to produce collisionless plasma even in Ohmically heated plasma.

The experimental resistive loop voltage and surface voltage are consistent with electrical conductivity including the trapped-particle correction as shown by Kikuchi (1990b) and Zarnstorff *et al.* (1990). A typical experimental result from TFTR is shown in Fig. 12.

Further verification of the electrical conductivity in tokamaks was obtained at the TFTR (Batha *et al.*, 1997) and at the JET (Kelliher *et al.*, 2005) showing that the time variation of the local poloidal field measured by motional Stark effect

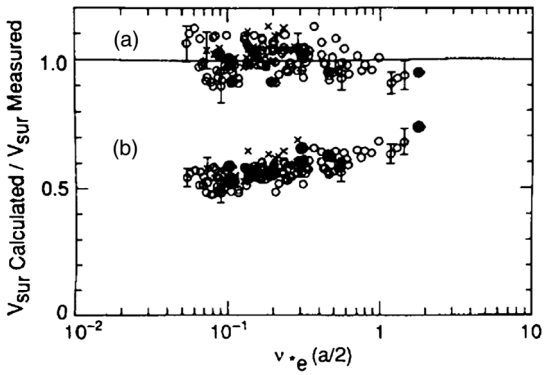

FIG. 12. Comparison of experimental and simulated surface voltages with and without trapped-particle correction. ×, ○, and ● correspond to different analysis methods and plasma species. From Zarnstorff *et al.*, 1990.

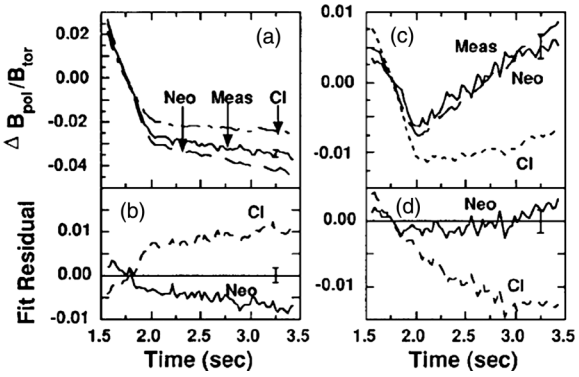

FIG. 13. Comparison of experimental and simulated local poloidal fields with and without trapped-particle correction in TFTR. Better agreement with experiment is obtained using the neoclassical resistivity. From Batha *et al.*, 1997.

(MSE) spectroscopy is better described by a time-dependent simulation using the neoclassical conductivity as shown in Fig. 13. The trapped particle does not contribute to the current. It creates a frictional force because of its velocity relative to the circulating particles. If the plasma is not sufficiently collisionless, the difference in loop voltages calculated with the NC and the Spitzer conductivity is small. So small and medium-sized tokamak experiments are controversial in identifying the viscosity effect (trapped-particle correction) to the electrical conductivity.

3. Bootstrap current

The bootstrap current was predicted theoretically by Galeev *et al.* (1971) and its importance for the steady-state operation of tokamaks was first noted by Bickerton *et al.* (1971). The generalized Ohm's law in Eq. (21) includes current driven by the thermodynamic forces V_{1a} and V_{2a} as $\langle \boldsymbol{B} \cdot \boldsymbol{J} \rangle_{\mathrm{bs}} = \sum_{a=1}^{4} \sum_{b=1}^{7} e_a n_a \hat{\alpha}_{ab} V_{\perp b}$. Here $\hat{\alpha}_{ab}$ is the matrix element of $\hat{\boldsymbol{\alpha}} = (\hat{\boldsymbol{M}} - \hat{\boldsymbol{L}})^{-1} \hat{\boldsymbol{M}}$. Substituting expressions for the thermodynamic forces V_{1a} and V_{2a} into Eq. (23), we obtain the following form for the bootstrap current:

$$\langle \boldsymbol{B} \cdot \boldsymbol{J} \rangle_{\mathrm{bs}} = -\sum_{a=1}^{4} \frac{F n_e}{|Z_a|} \left[L_{31}^{a} \frac{1}{n_a} \frac{dP_a}{d\psi} + L_{32}^{a} \frac{dT_a}{d\psi} \right], \tag{31}$$

$$\begin{aligned} L_{31}^{a} &= \sum_{b=1}^{4} \frac{|Z_a|}{Z_a} \frac{Z_b n_b}{n_e} \hat{\alpha}_{ab}, \\ L_{32}^{a} &= \sum_{b=1}^{3} \frac{|Z_a|}{Z_a} \frac{Z_b n_b}{n_e} \hat{\alpha}_{a,b+4}. \end{aligned} \tag{32}$$

Although V_{1a} includes an electrostatic potential term, this term vanishes for an axisymmetric plasma due to charge neutrality. Sauter *et al.* (1999) gave a more accurate fitted formula for the electrical conductivity and bootstrap current coefficients using a full Fokker-Planck operator since both Hirshman *et al.* (1981) and Shaing *et al.* (1996) used an approximate Coulomb collision operator.

The first observation of the bootstrap current was made in a multipole (Zarnstorff *et al.*, 1984) and subsequently in a tokamak (Zarnstorff *et al.*, 1988) by driving ~1/3 of the plasma current with the bootstrap current. Later, up to 80% of

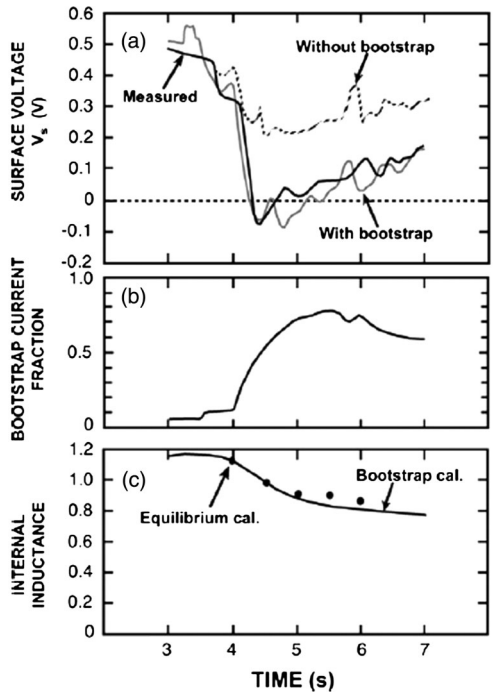

FIG. 14. (a) Time evolution of surface voltage, (b) bootstrap fraction, and (c) internal inductance from measurement and calculation. High-power NB is injected perpendicularly so that the NB does not drive significant current. The measured surface loop voltage is consistent with the 80% bootstrap current fraction. From Kikuchi *et al.*, 1995b.

the plasma current was driven by the bootstrap current at JT-60 (Kikuchi, 1990b) as shown in Fig. 14. Figure 15 shows the experimental and numerical bootstrap current fractions as functions of poloidal beta (Kikuchi *et al.*, 1995b). This shows that the bootstrap current fraction is proportional to the poloidal beta, $f_{\mathrm{boot}} \sim \beta_p$. This result opened good prospects toward efficient steady-state operation of the tokamak reactor.

In the *H* mode, a steep pressure gradient is formed near the plasma edge, called the edge transport barrier (ETB). This ETB induces an edge bootstrap current if the edge is deeply collisionless. The excitation of the edge bootstrap current

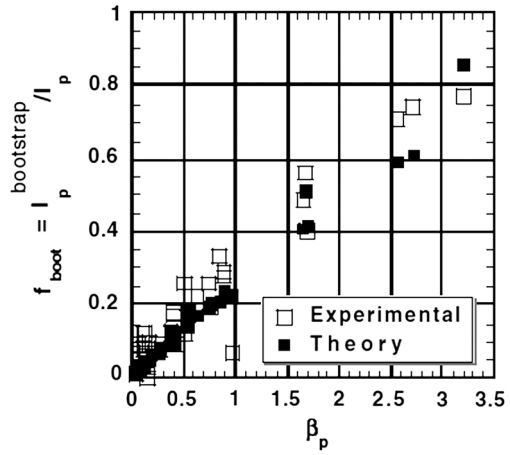

FIG. 15. Comparison of experimental and numerical bootstrap current fractions as a function of poloidal beta. From Kikuchi *et al.*, 1995b.

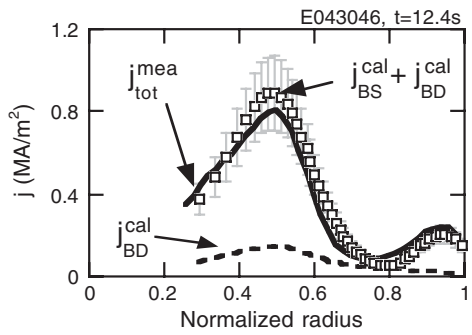

FIG. 16. Comparison of measured and calculated current-profiles in bootstrap-current-dominated JT-60U discharge. From Sakamoto *et al.*, 2005.

sensitively affects the time evolution of the parallel electric field at the ETB, $E_{\parallel} = \langle B_{\phi}^2 \rangle (\partial\psi/\partial\rho)/F$. In the *H* mode, a comparison of the measured surface voltage with simulation results including the bootstrap current was made by the JET team (1989); and a more detailed comparison of the time evolution of the edge parallel electric field with the theoretical prediction was made by Wade *et al.* (2004) and was consistent with the existence of the edge bootstrap current.

A direct comparison of measured and numerical local bootstrap current densities was made by using the bootstrap-current-dominated discharges at JT-60U (Sakamoto *et al.*, 2005) as shown in Fig. 16. The measured current profile is consistent with the prediction of collisional transport theory including the edge region ($0.8 < \rho/a < 1$).

Conventional neoclassical theory predicts zero bootstrap current density at the plasma center and requires a seed current to sustain the bootstrap current there (Hirshman *et al.*, 1981). Shaing *et al.* (1997) showed that the bootstrap current can be sustained without the seed current since the so-called potato particle can drive a viscous force to a passing particle at the plasma center providing a finite source current to form a poloidal magnetic field. Actually, a plasma discharge fully driven by the bootstrap current was produced at JT-60U (Takase *et al.*, 2006) as shown by Fig. 17 and more recently for a longer time scale of several current diffusion times at the TCV tokamak (Coda *et al.*, 2008).

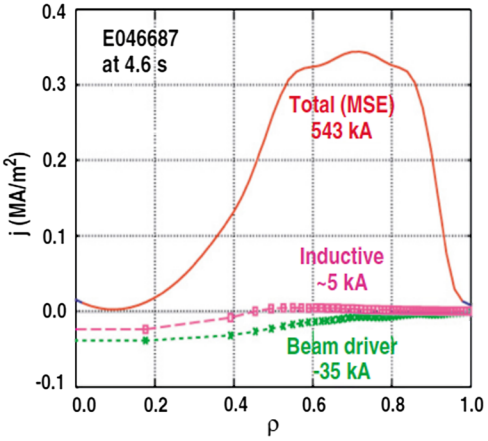

FIG. 17 (color online). Composition of current profile in full bootstrap discharge in JT-60U. From Takase *et al.*, 2006.

4. Neutral beam current drive

Fisch *et al.* (1987) reviewed early NBCD results of the DITE tokamak (Clark *et al.*, 1980) [$T_e(0) \sim 0.6$ keV, $E_b = 24$ keV], noting that trapped electrons play a negligible role. The key parameters of NBCD are the beam energy E_b and the electron temperature T_e. Since then, both the central electron temperature and the beam energy have been extended to a reactor-relevant regime, especially at JT-60 [$T_e(0) \sim 15$ keV, $E_b = 350$ keV] by use of N-NBI (Oikawa *et al.*, 2000, 2001).

When a fast neutral beam is injected tangentially to the torus, a circulating fast ion produces a fast-ion current ($J_{\rm fast}$) by multiple circulations around the torus. Collision with bulk electrons produces a shielding current ($J_{\rm shield}$) by the induced drift in the same direction as the fast ion. This shielding is not perfect due to the existence of trapped electrons and impurities. The sum of fast-ion and shielding currents is called a beam-driven current $J_{\rm bd}$ ($= J_{\rm fast} + J_{\rm shield}$).

The flux surface-averaged fast-ion current $\langle \boldsymbol{B}\cdot\boldsymbol{J}\rangle_{\rm fast}$ is obtained from the velocity distribution function of fast ions f as a solution of the Fokker-Planck equation valid for $v_{Ti} \ll v \ll v_{Te}$ (Cordey *et al.*, 1976),

$$\tau_{\rm se}\frac{\partial f}{\partial t} = \frac{1}{v^2}\frac{\partial}{\partial v}[(v_c^3+v^3)f] + \frac{\beta v_c^3}{v^3\eta\langle v/v_\parallel\rangle}\frac{\partial}{\partial\eta} \times\left[\frac{1-\eta^2}{\eta}\left\langle\frac{v_\parallel}{v}\right\rangle\frac{\partial f}{\partial\eta}\right] + \tau_{\rm se}S(v,\eta), \tag{33}$$

$$\tau_{\rm se} = \frac{3(2\pi)^{2/3}\epsilon_0^2 M_f T_e^{2/3}}{e^4 Z_f^2 n_e m_e^{1/2}\ln\Lambda} = \frac{0.20 A_f T_e[\mathrm{keV}]^{2/3}}{Z_f^2 n_e[10^{20}/m^3]\ln\Lambda}(s), \tag{34}$$

$$\beta = \frac{Z_{\rm eff}}{2A_f\bar{Z}}, \quad Z_{\rm eff} = \sum_{j=i,I}\frac{n_j Z_j^2}{n_e}, \quad \bar{Z} = \sum_{j=i,I}\frac{n_j Z_j^2}{n_e A_j}, \tag{35}$$

$$v_c = \left(\frac{2E_c}{m_f}\right)^{1/2}, \qquad E_c = \left(\frac{9\pi m_p}{16 m_e}\right)^{1/3}\bar{Z}^{2/3}A_f T_e, \tag{36}$$

$$\left\langle\frac{v}{v_\parallel}\right\rangle = \frac{2}{\pi}K\left[\left(\frac{\eta_t}{\eta}\right)^2\right], \qquad \left\langle\frac{v_\parallel}{v}\right\rangle = \frac{2}{\pi}E\left[\left(\frac{\eta_t}{\eta}\right)^2\right], \tag{37}$$

where $S(v,\eta)$ is the bounce-averaged fast-ion source rate per unit volume, $\tau_{\rm se}$ is the electron beam slowing down time, v_c is the critical velocity, $Z_{\rm eff}$ is the effective charge, and K and E are complete elliptic integrals of the first and second kind, respectively.

In the framework of the moment equation, we use only the momentum source term from the fast ion $\hat{S}_{\parallel f}$ for the neutral beam current drive. The flux surface-averaged beam-driven current may be decomposed as (Kikuchi *et al.*, 1995b)

$$\langle \boldsymbol{B}\cdot\boldsymbol{J}\rangle_{\rm bd} = \langle \boldsymbol{B}\cdot\boldsymbol{J}\rangle_{\rm fast} + \langle \boldsymbol{B}\cdot\boldsymbol{J}\rangle_{\rm shield}, \tag{38}$$

$$\langle \boldsymbol{B}\cdot\boldsymbol{J}\rangle_{\rm fast} = e_f n_f(\hat{\boldsymbol{M}}-\hat{\boldsymbol{L}})^{-1}_{ff}S_{\parallel f}, \tag{39}$$

$$\langle \boldsymbol{B}\cdot\boldsymbol{J}\rangle_{\rm shield} = \sum_{a=e,i,I} e_a n_a(\hat{\boldsymbol{M}}-\hat{\boldsymbol{L}})^{-1}_{af}S_{\parallel f}. \tag{40}$$

Here $S_{\parallel f} = \tau_{ee}\hat{S}_{\parallel f}/m_e n_e$. While the expression for the fast-ion current (39) is not accurate enough, the ratio of the beam-driven current $J_{\rm bd}$ to the fast-ion current $J_{\rm fast}$, the shielding factor $F = J_{\rm bd}/J_{\rm fast}$, can be calculated as follows:

$$F = \frac{\langle \boldsymbol{B}\cdot\boldsymbol{J}\rangle_{\rm bd}}{\langle \boldsymbol{B}\cdot\boldsymbol{J}\rangle_{\rm fast}} = 1 + \sum_{a=e,i,I}\frac{Z_a n_a}{Z_f n_f}\frac{(\hat{\boldsymbol{M}}-\hat{\boldsymbol{L}})^{-1}_{af}}{(\hat{\boldsymbol{M}}-\hat{\boldsymbol{L}})^{-1}_{ff}}. \tag{41}$$

Equation (41) is valid for all aspect ratios, multiple species, and all collisionalities. Start *et al.* (1980) calculated this shielding factor F assuming zero collisionalities to find the parametric dependences on $Z_{\rm eff}$ and ϵ at arbitrary aspect ratio ($0 \le \epsilon \le 1$). Lin-Liu *et al.* (1997) found that this shielding factor is related to the bootstrap coefficient L_{31}^e and gave an analytic expression in the collisionless limit. Results of a calculation by Eq. (41) with $\nu_a^* = 0$ agree well with the results of the Start *et al.* (1980) calculation [see Fig. 18(a)]. Honda *et al.* (2012) showed recently that finite collisionality has an important effect on the shielding factor by use of Eq. (41) as well as Sauter's L_{31}^e formula, valid for all collisionality regimes [see Fig. 18(b)]. Deviation from the collisionless limit starts at $\nu_{*e} \sim 10^{-2}$ depending on the model, indicating the need for reassessment of some comparisons between measured and calculated NBCD efficiencies (Suzuki *et al.*, 2011).

Beam ionization by various atomic processes is one important factor in determining the neutral-beam-driven current profile. Since the historical review of atomic data by Riviere *et al.* (1971), significant effort has been put forth to compile ionization cross section and rate coefficients especially under the auspices of the International Atomic Energy Agency (IAEA) (Janev *et al.*, 1993). Those from the ground state are refined for charge exchange with a bulk ion (Janev *et al.*, 1993, p. 78), ionization by ion impact (Janev *et al.*, 1993,

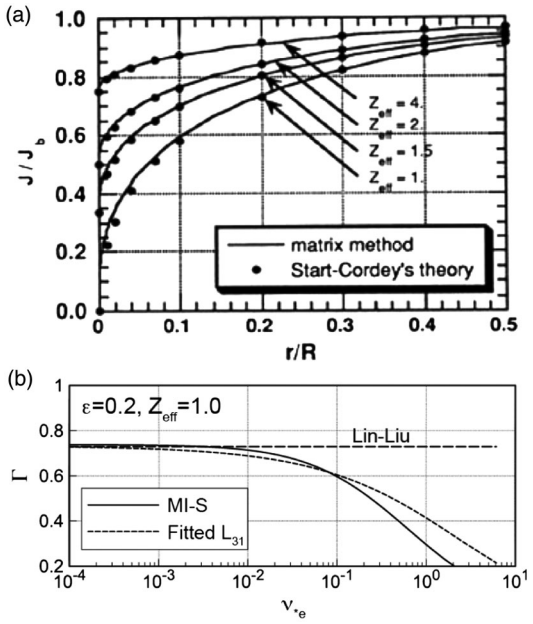

FIG. 18. (a) Comparison of shielding factors between the Start-Cordey theory and magnetic island (MI) methods with $\nu_a^* = 0$. From Kikuchi *et al.*, 1995b. (b) Collisionality dependence of the shielding factor from Eq. (41) and Sauter's L_{31} compared with the Lin-Liu model. From Honda *et al.*, 2012.

p. 68), ionization by impurity [Janev *et al.*, 1989, Eq. (15)], and ionization by electron impact (Janev, 1987, reaction 2.1.5 of p. 258). But there are a number of processes from excited states. Thus the process has multiple steps including ionization from excited states, and is called multistep ionization (MSI) as noted by Janev *et al.* (1989). Details of the MSI processes were refined by Suzuki *et al.* (1998); enhancement of the stopping cross section due to MSI was found to be as much as 20%–40% for the beam energy $E_b = 0.1$–1 MeV and a good agreement between experiments and calculation was obtained for the shine-through rate at JT-60. This MSI process is important for the evaluation of local driven current density since the deposition profile of fast ions is changed significantly. Various numerical codes such as ACCOME (Tani *et al.*, 1992), ASTRA (Pereverzev *et al.*, 1991), NFREYA (Fowler, 1979), and NUBEAM (Pankin *et al.*, 2004) have been developed to calculate the beam-driven current.

For a quantitative comparison of driven current density with calculations, an important improvement in "measuring" noninductive local current density was developed by Forest *et al.* (1994). From the generalized Ohm's law (21), the inductive electric field is given by

$$\langle \boldsymbol{E}\cdot\boldsymbol{B}\rangle = \frac{\langle B_\zeta^2\rangle}{F}\frac{\partial\psi}{\partial t}\bigg|_\phi. \tag{42}$$

Here a partial time derivative is taken with fixed toroidal flux ϕ. The time evolution of the poloidal flux $\psi(\rho, t)$ and the total local current density $\langle \boldsymbol{B}\cdot\boldsymbol{J}\rangle$ can be measured by the MSE diagnostics. With a profile measurement of density, temperature, and effective charge, we can calculate the electrical conductivity $\sigma_\parallel^{\rm NC}$ and the noninductive current profile $\langle \boldsymbol{B}\cdot\boldsymbol{J}\rangle_{\rm ni}$ can be measured from $\langle \boldsymbol{B}\cdot\boldsymbol{J}\rangle_{\rm ni} = \langle \boldsymbol{B}\cdot\boldsymbol{J}\rangle - \sigma_\parallel^{\rm NC}\langle \boldsymbol{E}\cdot\boldsymbol{B}\rangle$.

Figure 19 shows an experimentally measured NBCD current profile compared to calculations with and without the MSI process (Gormezano *et al.*, 2007). It shows that the calculation with MSI agrees with the measurement. In addition to such local measurements, a systematic comparison between theory and experiments was carried out in JT-60 (see Fig. 20) and shows good agreement if there

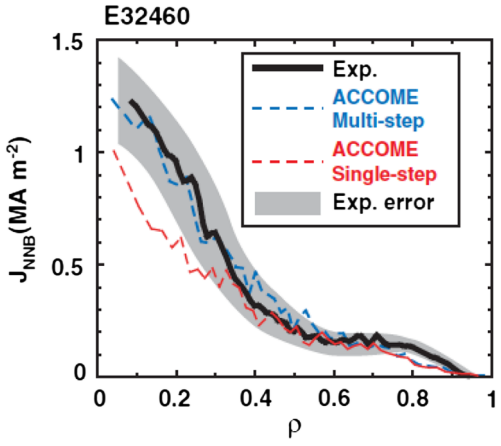

FIG. 19 (color online). Comparison of experimentally measured NBCD current profile with calculations with and without MSI. From Gormezano *et al.*, 2007.

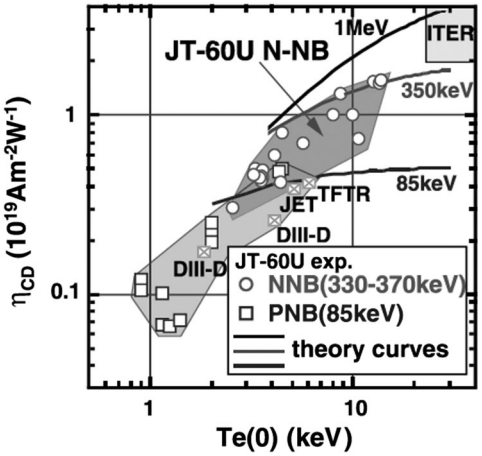

FIG. 20. Neutral-beam-current drive efficiency $\eta_{\rm CD} = \bar{n}_e R I_p^{\rm CD}/P_{\rm CD}$ at central electron temperature $T_e(0)$. From Oikawa *et al.*, 2001.

are no significant MHD activities. The dependence of the neutral beam current drive efficiency $\eta_{\rm CD} = \bar{n}_e R I_p^{\rm CD}/P_{\rm CD}$ on the central electron temperature $T_e(0)$ is also verified, showing that efficiency increases with $T_e(0)$ as shown in Fig. 20 (Oikawa *et al.*, 2001). These results, with their excellent predictability, are quite encouraging for future application . An efficient current drive via NBCD needs operation at high electron temperature, leading to a long slowing down time and accumulation of fast ion and α pressures. This leads to possible excitation of Alfvén eigenmodes (AEs), which will be discussed later.

5. Electron cyclotron current drive

After the comprehensive review by Fisch *et al.* (1987), significant progress was made in various rf fields. In this review, recent progress in ECCD is described due to its better accessibility to reactor plasma and its importance in stabilization of neoclassical TMs. A review by Prater *et al.* (2004) provides a good summary of recent progress.

There are some advantages of the electron cyclotron range of frequency (ECRF) application in the reactor environment. First is the absence of the accessibility problem and robust coupling irrespective of plasma conditions. Second is the high power density, enabling a smaller port penetration with low neutron backstreaming and tritium. Third is good controllability of local power deposition and parallel n index with a steerable launcher. Fourth is the recent availability of an efficient high-power gyrotron (Sakamoto *et al.*, 2007).

There are two mechanisms responsible for EC current drive. One is the Fisch-Boozer mechanism (Fisch *et al.*, 1980) creating asymmetry in parallel resistivity via wave-induced velocity space diffusion. The other is the Ohkawa mechanism (Ohkawa, 1976) creating an untrapped-trapped transition since the trapped electron cannot contribute to the toroidal current (see Fig. 21).

Momentum input to the electron is primarily perpendicular to the magnetic field because of electron cyclotron damping [a resonance condition given by $(\omega - l\Omega_e)/k_\parallel = v_\parallel$ of the first- or second-order harmonic electron cyclotron waves ($l = 1, 2$)]. There are two types of ECRF waves for CD, O modes and X modes, where $\tilde{\boldsymbol{E}}$ is parallel and perpendicular to the

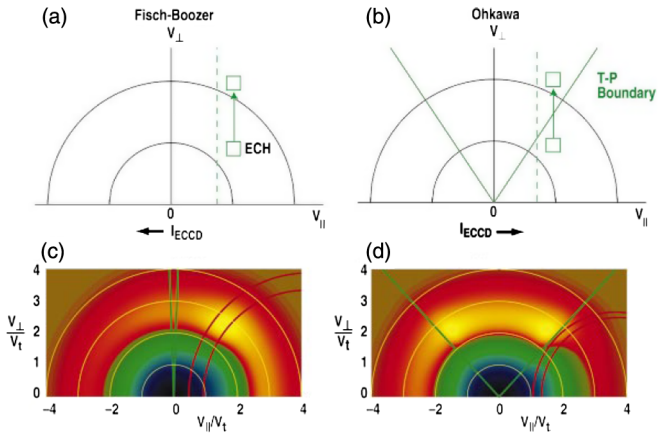

FIG. 21 (color online). Schematic explanation of Fisch-Boozer and Ohkawa mechanisms. From Prater *et al.*, 2004.

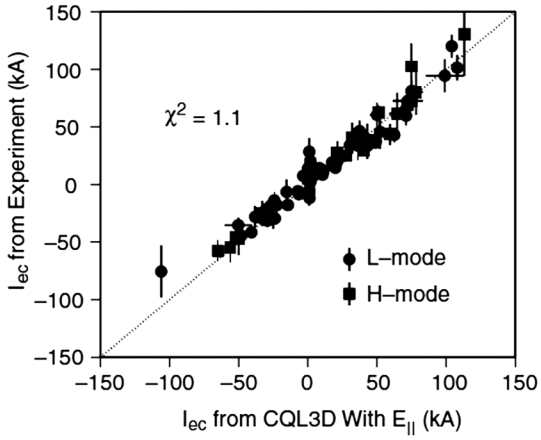

FIG. 22. Comparison of measured and calculated EC-driven current. From Petty *et al.*, 2002.

magnetic field $\boldsymbol{B}$, respectively (Stix, 1962). The wave propagation is governed by the Hamilton (or ray-tracing) equation

$$\frac{d\boldsymbol{x}}{dt} = \frac{\partial \Omega}{\partial \boldsymbol{k}}\bigg|_{x}, \qquad \frac{d\boldsymbol{k}}{dt} = -\frac{\partial \Omega}{\partial \boldsymbol{x}}\bigg|_{k}. \tag{43}$$

Here $\omega = \Omega(\boldsymbol{k}, \boldsymbol{x}, t)$ is the local dispersion relation. We expand the electron velocity distribution function as $f_e = f_{eM} + f_{e1}$ (f_{eM} is Maxwellian) and its drift kinetic equation in the toroidal geometry for a given wave amplitude is given by

$$\frac{u_\parallel}{\gamma}\boldsymbol{b}\cdot\frac{\partial f_{e1}}{\partial \boldsymbol{x}} - C(f_{e1}) = -\frac{\partial}{\partial \boldsymbol{u}}\cdot\boldsymbol{S}_w. \tag{44}$$

Here $\boldsymbol{b}$ is the unit vector along the magnetic field, $\boldsymbol{u} = \boldsymbol{p}/m_e = \gamma\boldsymbol{v}$ is momentum per unit mass, $\gamma = (1 + u^2/c^2)^{1/2}$, $C(f_{e1})$ is the linearized electron collision term, and $\boldsymbol{S}_w = \boldsymbol{D}_{\mathrm{QL}}\cdot\partial f_{e1}/\partial\boldsymbol{u}$ is the wave-induced flux in velocity space due to quasilinear diffusion via wave-particle interaction. The wave-induced flux ($\boldsymbol{S}_w$) is given by Kennel *et al.* (1966) for Landau damping ($l = 0$) and electron cyclotron damping ($l \neq 0$) as follows:

$$\boldsymbol{D}_{\mathrm{QL}} = \sum_{n=-\infty}^{\infty}\frac{\pi}{2}\left(\frac{e}{m_e}\right)^2\delta(\gamma\omega - k_\parallel v_\parallel - l\Omega_e)\boldsymbol{a}_n^*\boldsymbol{a}_n, \tag{45}$$

$$\boldsymbol{a}_n = \Theta_n\left[\left(1 - \frac{k_\parallel u_\parallel}{\gamma\omega}\right)\hat{\boldsymbol{u}}_\perp + \frac{k_\parallel u_\perp}{\gamma\omega}\hat{\boldsymbol{u}}_\parallel\right], \tag{46}$$

$$\Theta_n = \frac{E_{w+}J_{n-1} + E_{w-}J_{n+1}}{\sqrt{2}} + \frac{u_\parallel}{u_\perp}J_nE_{w\parallel}. \tag{47}$$

Here $\Omega_e = -eB/m_e$, $*$ means complex conjugate, $\hat{\boldsymbol{u}}_\parallel$ and $\hat{\boldsymbol{u}}_\perp$ are unit vectors in perpendicular and parallel directions, and J_n is the nth-order Bessel function with its argument $k_\perp v_\perp/\Omega_e$. E_{w+} and E_{w-} are the left- and right-handed components of E_w. Instead of solving Eq. (44), Antonsen *et al.* (1982) and Taguchi (1983) realized that the rf-induced current can be obtained by using a solution of the following adjoint equation originally used by Spitzer-Härm to obtain electrical conductivity:

$$\frac{u_\parallel}{\gamma}\boldsymbol{b}\cdot\frac{\partial\chi}{\partial\boldsymbol{x}} + \frac{1}{f_{eM}}C(\chi f_{eM}) = -\frac{eu_\parallel B}{\gamma\langle B^2\rangle}. \tag{48}$$

It is easy to prove the following formulas for the generated current and the dissipated power by using Eqs. (44) and (48), and partial integration:

$$\langle\boldsymbol{J}\cdot\boldsymbol{B}\rangle = \langle B^2\rangle\left\langle\int d^3u\boldsymbol{S}_w\cdot\frac{\partial\chi}{\partial\boldsymbol{u}}\right\rangle, \tag{49}$$

$$P_d = \left\langle\int d^3u\boldsymbol{S}_w\cdot\frac{\partial\boldsymbol{\epsilon}}{\partial\boldsymbol{u}}\right\rangle. \tag{50}$$

Here $\boldsymbol{\epsilon} = \gamma m_e c^2$ is the electron energy, and $\partial\boldsymbol{\epsilon}/\partial\boldsymbol{u} = m_e\boldsymbol{u}/\gamma$. The solution of the adjoint equation (48) is $\chi = 0$ for $\lambda > \lambda_c$ and that for $\lambda < \lambda_c$ is given by Taguchi *et al.* (1989) as

$$\chi(u,\lambda) = \frac{\langle B^2\rangle}{2f_c}\sigma K(u)\int_\lambda^{\lambda_c}\frac{d\lambda}{\langle\sqrt{1-\lambda B}\rangle}. \tag{51}$$

Here $\lambda = (u_\perp/u_\parallel)^2/B$, $\lambda_c = 1/B_{\max}$, $\sigma = u_\parallel/|u_\parallel|$, and K is a solution of the one-dimensional integro-differential equation, which can be obtained using the Sonine expansion (Taguchi *et al.*, 1989) or numerically using an exact relativistic collision term (Hamamatsu *et al.*, 2001).

A comparison of experimental and theoretical expectations of the ECCD was done at DIII-D (Petty *et al.*, 2002) (see Fig. 22) and also at JT-60U (Suzuki *et al.*, 2004a). An ECCD of 0.74 MA is demonstrated in high-electron-temperature [$T_e(0) = 23$ keV] plasma at JT-60U by taking the $E_\parallel$ effect (Dnestrovski *et al.*, 1988) into account (Suzuki *et al.*, 2004b). The existence of a trapped electron reduces the net driven current and its effect is more significant for outboard EC injection (Cohen *et al.*, 1987) as confirmed experimentally at DIII-D by Petty *et al.* (2003) and at JT-60U by Suzuki *et al.* (2004a). Figure 23 shows the calculated and experimental results. Here $\zeta = e^3\eta_{\mathrm{CD}}/\epsilon_0^2 kT_e$ is the normalized EC current drive efficiency (Lin-Liu *et al.*, 2003). A transformer recharging by ECCD was also demonstrated at TCV by Sauter *et al.* (2000).

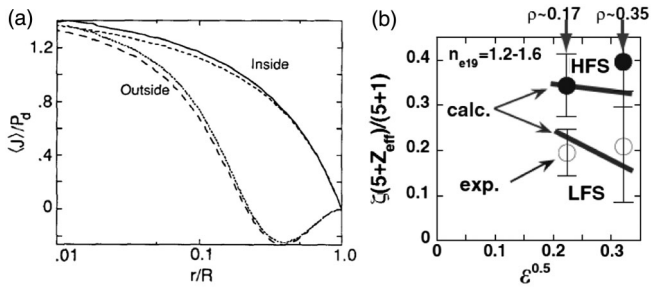

FIG. 23. (a) Effect of inboard and outboard injection on ECCD efficiency. From Cohen *et al.*, 1987. (b) Experimental result. From Suzuki *et al.*, 2004a.

C. Rotation physics

Toroidal rotation physics is now important in the effect of rotation shear on confinement improvement, rotational stabilization of MHD modes, and also observation of intrinsic toroidal rotation. All these elements are important and sometimes essential to realize the steady-state tokamak reactor.

1. Neoclassical rotations

Equation (18) governs the parallel flows in the tokamak. Kim *et al.* (1991) derived an analytic expression for the poloidal and toroidal rotations assuming that the impurity is in the Pfirsh-Schlüter regime and has large mass ratio ($m_i/m_I \ll 1$), while Kikuchi (1991) solved the moment equation numerically to analyze toroidal and poloidal rotations at JT-60U. The general flow balance equation (16) allows us to derive an expression for the toroidal flows of electrons, ions, and impurities. Here we concentrate on the effect of the thermodynamic force on toroidal rotation, assuming $E_\parallel = \hat{S}_\parallel = 0$, and neglect the fast-ion component, for simplicity. From Eq. (12), the local toroidal flow for species a is the summation of the flux surface-averaged parallel flow and the Pfirsch-Schlüter flow as follows:

$$u_{a\zeta}^{(1)} = \frac{B_\zeta \langle B u_{\parallel a}\rangle}{\langle B^2\rangle} - \left[1 - \frac{B_\zeta^2}{\langle B^2\rangle}\right] R\left(\Phi' + \frac{P_a'}{e_a n_a}\right). \tag{52}$$

Here the prime denotes the derivative with respect to ψ. From Eq. (16), we obtain the following expression for the flux surface-averaged parallel flows:

$$\langle B u_{\parallel a}\rangle = -F \sum_{b=1}^{3}\left[\alpha_{ab}\left(\Phi' + \frac{P_b'}{e_b n_b}\right) + \frac{\alpha_{a,b+3}}{e_b} T_b'\right]. \tag{53}$$

The impurity (e.g., carbon) toroidal rotation can be measured by charge-exchange recombination spectroscopy, which can be used to determine the radial electric field using Eq. (52), if density and temperature profiles are known, as follows:

$$\frac{d\Phi}{d\psi} = -\frac{\langle B^2\rangle u_{\zeta I}/RB_\zeta^2 + \sum_{b=1}^{3}(\alpha_{Ib}^* P_b'/e_b n_b + \alpha_{I,b+3} T_b'/e_b)}{\sum_b \alpha_{Ib}^*}. \tag{54}$$

Here $\alpha_{Ib}^* = \alpha_{Ib} + (\langle B^2\rangle/B_\zeta^2 - 1)\delta_{ab}$. This radial electric field profile can be used to discuss the effect of radial electric field shear on transport reduction as in Sec. VI. Once the radial electric field is known, we can calculate parallel flows of electron, ion, and impurity from Eq. (52). If we calculate these flows for a typical high-temperature plasma, we find significant differences between ion and impurity toroidal rotations of several 10 km/s in high-β_p plasma (Kikuchi, 1991).

According to Kim *et al.* (1991), the electron contribution to the momentum balance can be neglected since electron inertia is small, and the flow relations of ions and impurities are given as follows:

$$\hat{\boldsymbol{\mu}}^I \cdot \boldsymbol{u}_\theta^I = \hat{\boldsymbol{L}}_{II} \cdot \boldsymbol{u}_\parallel^I + \hat{\boldsymbol{L}}_{Ii} \cdot \boldsymbol{u}_\parallel^i, \tag{55}$$

$$\hat{\boldsymbol{\mu}}^i \cdot \boldsymbol{u}_\theta^i = \hat{\boldsymbol{L}}_{iI} \cdot \boldsymbol{u}_\parallel^I + \hat{\boldsymbol{L}}_{ii} \cdot \boldsymbol{u}_\parallel^i, \tag{56}$$

$$\hat{\boldsymbol{u}}_\theta^a = \boldsymbol{u}_\parallel^a - \boldsymbol{V}^a, \tag{57}$$

where the last equation for $\hat{\boldsymbol{u}}_\theta^a$ is obtained from Eq. (8) and $\hat{\boldsymbol{u}}_\theta^a$, $\boldsymbol{u}_\parallel^a$, $\boldsymbol{V}^a$, $\hat{\boldsymbol{\mu}}^a$, and $\hat{\boldsymbol{L}}_{ab}$ are defined as

$$\hat{\boldsymbol{u}}_\theta^a = \begin{bmatrix} \langle B^2\rangle \hat{u}_{a\theta} \\ \frac{2\langle B^2\rangle \hat{q}_{a\theta}}{5P_a} \end{bmatrix}, \quad \boldsymbol{u}_\parallel^a = \begin{bmatrix} \langle B u_{\parallel a}\rangle \\ \frac{2\langle B q_{\parallel a}\rangle}{5P_a} \end{bmatrix}, \quad \boldsymbol{V}^a = \begin{bmatrix} BV_{1a} \\ BV_{2a} \end{bmatrix}, \tag{58}$$

$$\hat{\boldsymbol{\mu}}^a = \begin{bmatrix} \hat{\mu}_{a1} & \hat{\mu}_{a2} \\ \hat{\mu}_{a2} & \hat{\mu}_{a3} \end{bmatrix}, \quad \hat{\boldsymbol{L}}_{ab} = \begin{bmatrix} \hat{l}_{11}^{ab} & -\hat{l}_{12}^{ab} \\ -\hat{l}_{21}^{ab} & \hat{l}_{22}^{ab} \end{bmatrix}. \tag{59}$$

Since the impurity collisionality is given by $\nu_I^* = (n_I Z_I^4/n_i Z_i^4)\nu_i^*$ considering fast equipartition between ion and impurity ($T_i \approx T_I$), the impurity may be in the Pfirsh-Schlüter regime (negligible impurity viscous force $\hat{\boldsymbol{\mu}}^I \cdot \boldsymbol{u}_\theta^I \approx 0$) while the bulk ion is in a deeply collisionless regime $\nu_I^* \gg \nu_i^*$. Therefore, the impurity parallel flow can be given as $\boldsymbol{u}_\parallel^I = -\hat{\boldsymbol{L}}_{II}^{-1}\hat{\boldsymbol{L}}_{Ii} \cdot \boldsymbol{u}_\parallel^i$. Using the large-impurity-mass approximation $m_I \gg m_i$, substitution into Eq. (56) gives the following ion momentum balance equation:

$$\hat{\boldsymbol{\mu}}^i \cdot \hat{\boldsymbol{u}}_\theta^i = -\begin{bmatrix} 0 & 0 \\ 0 & \gamma \end{bmatrix} \cdot \boldsymbol{u}_\parallel^i. \tag{60}$$

Here $\gamma = \sqrt{2} + \alpha$, and $\alpha = n_I Z_I^2/n_i Z_i^2$. [The $\beta = O((m_i/m_I)^2)$ term of Kim *et al.* (1991) is neglected.] Using $\boldsymbol{u}_\parallel^i = \hat{\boldsymbol{u}}_\theta^i + \boldsymbol{V}^i$, we obtain the following expression:

$$\begin{bmatrix} \hat{\mu}_{i1} & \hat{\mu}_{i2} \\ \hat{\mu}_{i2} & \hat{\mu}_{i3} + \gamma \end{bmatrix} \hat{\boldsymbol{u}}_\theta^i = -\begin{bmatrix} 0 & 0 \\ 0 & \gamma \end{bmatrix} \boldsymbol{V}^i. \tag{61}$$

This equation indicates that the $\hat{u}_\theta$-driven ion viscous force is balanced against the $\hat{q}_\theta$-driven ion viscous force so that the total parallel ion viscous force becomes zero. Equation (61) leads to the following analytic expressions for $\hat{\boldsymbol{u}}_\theta^i$, $\boldsymbol{u}_\parallel^i$, $\boldsymbol{u}_\parallel^I$, and $\hat{\boldsymbol{u}}_\theta^I$:

$$\hat{\boldsymbol{u}}_\theta^i = \begin{bmatrix} 0 & K_1 \\ 0 & -\frac{\hat{\mu}_{i1}}{\hat{\mu}_{i2}} K_1 \end{bmatrix} \boldsymbol{V}^i, \qquad \boldsymbol{u}_\parallel^i = \begin{bmatrix} 1 & K_1 \\ 0 & K_2 \end{bmatrix} \boldsymbol{V}^i, \tag{62}$$

$$\boldsymbol{u}_\parallel^I = \begin{bmatrix} 1 & K_1 + 1.5K_2 \\ 0 & 0 \end{bmatrix} \boldsymbol{V}^i, \qquad \hat{\boldsymbol{u}}_\theta^I = \boldsymbol{u}_\parallel^I - \boldsymbol{V}^I, \tag{63}$$

$$K_1 = \frac{\gamma \hat{\mu}_{i2}}{D}, \qquad K_2 = \frac{\hat{\mu}_{i1}\hat{\mu}_{i3} - \hat{\mu}_{i2}^2}{D}, \tag{64}$$

$$D = \hat{\mu}_{i1}(\hat{\mu}_{i3} + \gamma) - \hat{\mu}_{i2}^2. \tag{65}$$

If we use tokamak ordering $B \approx B_\zeta$ and $\hat{u}_{a\theta} \approx u_\theta/B_\theta$ by neglecting poloidal variation, we obtain the following form of $u_{\|i}$, $u_{\|I}$, $u_{\theta i}$, and $u_{\theta I}$:

$$u_{\|i} \approx \frac{-1}{B_\theta}\left[\frac{d\Phi}{dr} + \frac{1}{eZ_i n_i}\frac{dP_i}{dr} + \frac{K_1}{eZ_i}\frac{dT_i}{dr}\right], \tag{66}$$

$$u_{\|I} \approx \frac{-1}{B_\theta}\left[\frac{d\Phi}{dr} + \frac{1}{eZ_i n_i}\frac{dP_i}{dr} + \frac{K_1 + 1.5K_2}{eZ_i}\frac{dT_i}{dr}\right], \tag{67}$$

$$u_{\theta i} \approx -\frac{K_1}{eZ_i B_\zeta}\frac{dT_i}{dr}, \tag{68}$$

$$u_{\theta I} \approx -\frac{K_1 + 1.5K_2}{eZ_i B_\zeta}\frac{dT_i}{dr} - \frac{1}{eZ_I n_I B_\zeta}\frac{dP_I}{dr} + \frac{1}{eZ_i n_i B_\zeta}\frac{dP_i}{dr}. \tag{69}$$

All terms proportional to dT_i/dr in the above four equations originate from the heat-flow balance equation.

If we neglect these terms, we see that $u_{\theta i} \approx 0$ due to strong viscous damping of poloidal rotation. The term $u_{\|i}$ is determined to satisfy $u_{\theta i} \approx 0$ (the poloidal component of parallel flow must compensate the poloidal component of $E_r \times B$ and ion diamagnetic flows). Also $u_{\|i} \approx u_{\|I}$ because there is negligible impurity parallel viscous force. Then the impurity parallel flow cancels the poloidal component of $E_r \times B$ and ion (not impurity) diamagnetic flows. Therefore, the impurity poloidal flow becomes the difference between impurity and ion diamagnetic flows [$u_{\theta I} \approx [(dP_i/dr)/Z_i n_i - (dP_I/dr)/Z_I n_I]/eB_\zeta$].

Retaining the dT_i/dr terms, we see ion and impurity toroidal rotation proportional to dT_i/dr and $1/B_\theta$ (large at high β_p),

$$\Delta u_\| = u_{\|I} - u_{\|i} = -\frac{1.5K_2}{eZ_i B_\theta}\frac{dT_i}{dr}. \tag{70}$$

If the total toroidal momentum is zero ($n_i m_i u_{\|i} + n_I m_I u_{\|I} = 0$), this equation together with Eq. (70) implies positive toroidal rotation for ions and negative toroidal rotation for impurities as follows:

$$u_{\|I} = -\frac{n_i m_i}{n_I m_I}u_{\|i} = \frac{-n_i m_i}{n_i m_i + n_I m_I}\frac{1.5K_2}{eZ_i B_\theta}\frac{dT_i}{dr}. \tag{71}$$

Since $n_i m_i/n_I m_I \gg 1$ holds in most cases, the impurity rotates strongly in the counter direction and the bulk ion rotates weakly in the cocurrent direction ($|u_{\|I}| \gg |u_{\|i}|$) if the total toroidal momentum is zero. Since there is expected to be very little momentum, an Ohmically heated plasma is ideal to test strong counter impurity rotation. At the Sherwood conference, Kim (1991) discussed the impurity toroidal rotation (nearly parallel flow) in Ohmically heated plasma at JFT-2M, implying that its value of -12.5 km/s is consistent with this temperature gradient-driven counter impurity toroidal rotation from Eq. (71). This suggests that there is no significant hidden torque drive in Ohmically heated plasma. But later many experiments showed strong intrinsic rotation driven by hidden torque.

2. Neoclassical toroidal viscosity

One important property of the axisymmetric system is the conservation of total toroidal momentum. The total toroidal angular momentum balance equation is as follows:

$$\sum_a m_a\left\langle n_a R\frac{du_{a\zeta}}{dt}\right\rangle = \sum_a \langle R^2\nabla\zeta\cdot(\nabla\cdot\mathbf{\Pi}_a + \boldsymbol{M}_a)\rangle. \tag{72}$$

Noting that the viscosity tensor $\mathbf{\Pi}_a$ is symmetric for axisymmetric plasma and $\nabla(R^2\nabla\zeta)$ is an antisymmetric tensor (Hirshman, 1978), the flux surface average of the toroidal viscous force can be shown to be zero, $\langle R^2\nabla\zeta\cdot\nabla\cdot\mathbf{\Pi}_a\rangle = 0$. This means that the toroidal drag force caused by magnetic field variation is zero for the axisymmetric system. When symmetry is broken by the application of a nonaxisymmetric field, $\langle R^2\nabla\zeta\cdot\nabla\cdot\mathbf{\Pi}_a\rangle \neq 0$. This drag is called the neoclassical toroidal viscosity (NTV) and has been observed at NSTX (Zhu *et al.*, 2006); see Fig. 24.

The zeroth-order ion force balance is given by

$$0 = eZ_i n_i(\boldsymbol{E} + \boldsymbol{u}_i \times \boldsymbol{B}) - \nabla P_i. \tag{73}$$

In the flux coordinates (ψ, θ, ζ), the magnetic field is expressed as $\boldsymbol{B} = \nabla\psi \times \nabla(q\theta - \zeta)$. The radial component of the above equation can be obtained by taking the inner product with the tangent vector $\partial\boldsymbol{x}/\partial\psi$ and using the identity $\partial\boldsymbol{x}/\partial\psi\cdot\nabla\psi = 1$, where $\boldsymbol{x}$ is the position vector,

$$\boldsymbol{u}_i\cdot\nabla\zeta = -\left[\frac{d\Phi}{d\psi} + \frac{1}{eZ_i n_i}\frac{dP_i}{d\psi}\right] + q\boldsymbol{u}_i\cdot\nabla\theta. \tag{74}$$

In a tokamak plasma with symmetry breaking, the electrostatic potential Φ is determined so that nonambipolar flux $\langle\mathbf{\Gamma}_{na}\cdot\nabla V\rangle$ becomes zero. In Hamada coordinates, the nonambipolar flux $\langle\mathbf{\Gamma}_{na}\cdot\nabla V\rangle$ is related to the toroidal viscous force as $\langle\mathbf{\Gamma}_{na}\cdot\nabla V\rangle = [V'(\psi)^2/e_a q]\langle\boldsymbol{B}_t\cdot\nabla\cdot\mathbf{\Pi}_a\rangle$ (Shaing *et al.*, 1983). In the collisionless regime, the ion viscous force is larger than that for the electron by a factor of $(m_i/m_e)^{1/2}$. The zero-nonambipolar-flux condition is then given by $\langle\boldsymbol{B}_t\cdot\nabla\cdot\mathbf{\Pi}_i\rangle = 0$ for electron-ion plasma, from which Shaing *et al.* (2003) derived the following relation for the ion in the collisionless regime:

$$\frac{d\Phi}{d\psi} + \frac{1}{eZ_i n_i}\frac{dP_i}{d\psi} = -\frac{\lambda_2}{eZ_i\lambda_1}\frac{dT_i}{d\psi}. \tag{75}$$

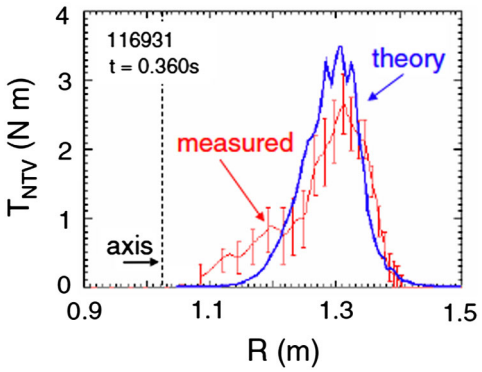

FIG. 24 (color online). Observation of neoclassical toroidal viscosity (NTV) at NSTX. From Zhu *et al.*, 2006.

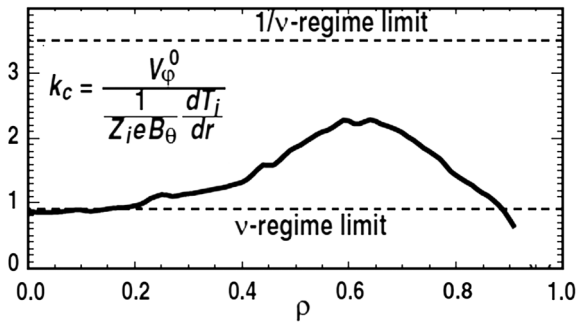

FIG. 25. Observation of offset toroidal rotation due to NTV at DIII-D. From Garofalo *et al.*, 2008.

Here λ_1 and λ_2 are numerical constants given by Shaing *et al.* (2003). Even if we include an impurity, we may be able to assume the impurity is in the Pfirsh-Schlüter regime (namely, the impurity toroidal viscosity is small) while the ion is deeply in the collisionless regime as in Sec. IV.C.1. Then Eq. (75) is still a zero-nonambipolar-flux condition. Substituting Eq. (75) into Eq. (74), we obtain the following expressions for offset rotations (Kikuchi, 2011a):

$$\boldsymbol{u}_{i0}\cdot\nabla\zeta = \frac{\lambda_2}{eZ_i\lambda_1}\frac{dT_i}{d\psi} + q\boldsymbol{u}_{i0}\cdot\nabla\theta, \tag{76}$$

$$\boldsymbol{u}_{i0}\cdot\nabla\theta = -\frac{K_1 F(\boldsymbol{B}\cdot\nabla\theta)}{eZ_i\langle B^2\rangle}\frac{dT_i}{d\psi}. \tag{77}$$

Since measurement of the toroidal rotation is made using the impurity toroidal rotation, the offset toroidal rotation of the impurity has to be obtained. In cylindrical coordinates, the offset toroidal rotations of ion and impurity are given as follows:

$$u_{i\zeta 0} = \frac{3.54 - K_1}{eZ_i B_\theta}\frac{dT_i}{dr}, \tag{78}$$

$$u_{I\zeta 0} = \frac{3.54 - 1.5K_2 - K_1}{eZ_i B_\theta}\frac{dT_i}{dr}. \tag{79}$$

The offset rotation has been confirmed experimentally at DIII-D (Garofalo *et al.*, 2008); see Fig. 25. Since K_1 and K_2 are of the order of 0.3–1.2 in the collisionless tokamak plasma as given by Kim *et al.* (1991), agreement with the collisionless ion $(1/\nu)$ regime becomes better when we include finite poloidal flow correction and the impurity effect. Physically,the NTV is caused by a nonambipolar particle flux. Evans *et al.* (2008) indicated that application of a resonant magnetic perturbation (RMP) induces cotoroidal rotation, which implies selective electron loss.

3. Intrinsic rotation

Momentum transport has long been a subject of interest. The existence of a nondiffusive toroidal momentum flux was observed for the first time by Nagashima *et al.* (1994) at JT-60U using the modulation technique. The off-diagonal contribution to the momentum flux was clarified at JFT-2M as shown in Fig. 26 (Ida *et al.*, 1995).

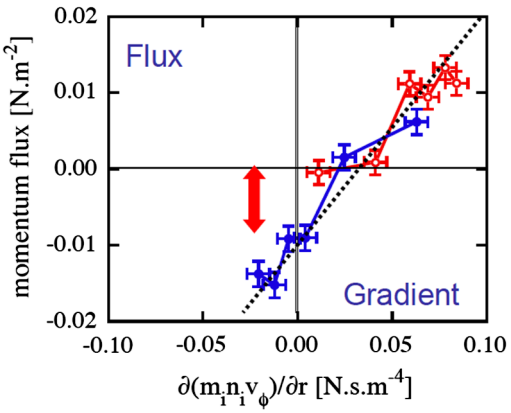

FIG. 26 (color online). Gradient-flux relation in toroidal momentum showing a clear offset in flux as evidence of nondiffusive (off-diagonal) transport of toroidal momentum. From Ida *et al.*, 1995.

The observation of intrinsic rotation by Rice *et al.* (1997) at Alcator C-Mod, and intermachine comparison by Rice *et al.* (2007), clarified the parametric dependence of intrinsic rotation $\Delta v_\phi \sim \Delta W/I_p$ and had a significant impact on the momentum transport studies searching for hidden torque input. Scarabosio *et al.* (2006) found slightly different scaling $\Delta v_\phi \sim T_i/I_p$. The existence of intrinsic torque has been shown at DIII-D (Solomon *et al.*, 2007). The parametric dependence of intrinsic rotation was investigated by Yoshida *et al.* (2008) ($v_\phi \propto dP/dr$), Rice *et al.* (2011) ($v_\phi \propto dT/dr$), and Angioni *et al.* (2011) ($dv_\phi/dr \propto dn/dr$).

On the theoretical front, Dominguez *et al.* (1993) first calculated the residual stress for intrinsic rotation. Garbet *et al.* (2001) gave the first numerical gyrofluid ion temperature gradient (ITG) simulation to show toroidal flow generation by the Reynolds stress $\Pi_{r\|} = \langle v_{Er} v_{E\|}\rangle$ (see Fig. 27). A gyrokinetic full-f Vlasov simulation of toroidal ITG turbulent momentum transport with consistent momentum conservation properties [see Scott *et al.* (2010)] by Idomura *et al.* (2009) showed the buildup of intrinsic co- and counterrotations on a time scale of τ_{ii}.

Wang *et al.* (2010) studied the parametric dependence of intrinsic rotation by a gyrokinetic simulation of ITG and

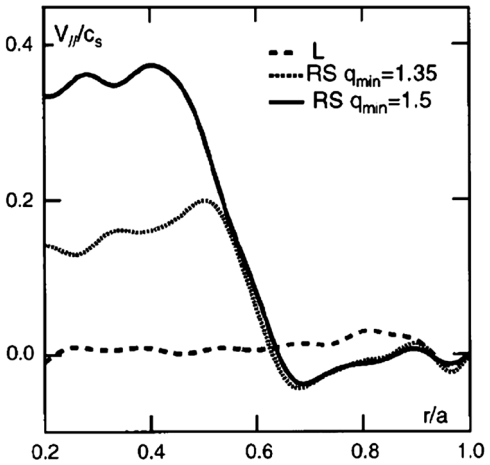

FIG. 27. Intrinsic rotation by Reynolds stress in ITG turbulence. From Garbet *et al.*, 2001.

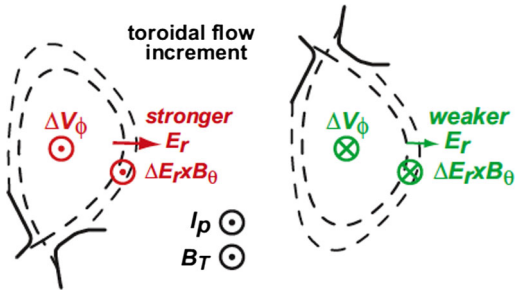

FIG. 28 (color online). Excitation of toroidal flow by different divertor geometries. From La Bombard *et al.*, 2004.

trapped electron mode (TEM) turbulences and reported that intrinsic rotation by ITG is proportional to dT_i/dr, while intrinsic rotation by a collisionless TEM increases with both dT_e/dr and dn_e/dr (Wang *et al.*, 2011). Angioni *et al.* (2011) reported that the reversal of intrinsic rotation from corotation to counterrotation correlates with the large density gradient in the TEM-dominant regime or at the ITG-TEM transition. Wang *et al.* also reported that enhanced $k_\parallel$ symmetry breaking due to larger q variation at a lower plasma current is consistent with the I_p part of the Rice scaling, $\Delta v_\phi \sim 1/I_p$.

The boundary condition at the separatrix is important since the so-called no-slip condition is usually used for turbulent simulation studies. Concerning these topics, La Bombard *et al.* (2004) showed at C-Mod that the strong ballooning character of transport leads to a net scrape-off layer (SOL) toroidal momentum whose sign is dependent on the X-point location. When $\boldsymbol{B} \times \nabla B$ is toward (away from) the X point, a positive (negative) increment in cocurrent rotation is observed (see Fig. 28). Bortolon *et al.* (2006) showed that the direction of the intrinsic toroidal rotation can be reversed at a critical density.

Diamond *et al.* (2009) clarified the basic mechanism of turbulent momentum transport. The mean-field momentum flux driven by electrostatic turbulence $\Pi_{r,\phi}$ is given by the Reynolds stress $\langle \tilde{v}_r \tilde{v}_\phi \rangle$ as $\Pi_{r,\phi} = \langle n \rangle \langle \tilde{v}_r \tilde{v}_\phi \rangle$ by neglecting convective flux $\langle \tilde{v}_r \tilde{n} \rangle \langle v_\phi \rangle$ and third-order flux $\langle \tilde{n} \tilde{v}_r \tilde{v}_\phi \rangle$, and $\langle \tilde{v}_r \tilde{v}_\phi \rangle$ can be further decomposed as follows:

$$\langle \tilde{v}_r \tilde{v}_\phi \rangle = -\chi_\phi \frac{\partial \langle v_\phi \rangle}{\partial r} + V \langle v_\phi \rangle + \Pi^R_{r,\phi}. \tag{80}$$

Here χ_ϕ is the turbulent viscosity, V is the convective velocity, and $\Pi^R_{r,\phi}$ is called the residual stress. The turbulent viscosity is closely related to the turbulent ion thermal diffusivity and the ratio is called the Prandtl number ($\mathrm{Pr} = \chi_\phi/\chi_i$). The residual stress $\Pi^R_{r,\phi}$ is defined as all momentum flux other than diffusive and convective fluxes (Gurcan *et al.*, 2008) and is proportional to $\partial \langle n \rangle / \partial r$ and/or $\partial \langle T \rangle / \partial r$. Residual stress originating from resonant and nonresonant wave-particle interaction is given by $\Pi^{\mathrm{wave}}_{r,\phi} = \int d\boldsymbol{k} v_{gr} k_\parallel \delta N$. Using the solution of the wave kinetic equation, the quasiparticle density is given by $\delta N = \tau_c [k_\theta V'_E \partial \langle N \rangle / \partial k_r - v_{gr} \partial \langle N \rangle / \partial r]$. Here V'_E and τ_c are the electric field shear and the correlation time of the δN response, respectively. The first and second terms of δN are related to $k_\parallel$ symmetry breaking and radial inhomogeneity of the turbulent amplitude, respectively (Gurcan *et al.*, 2007). Peeters *et al.* (2007) showed that Coriolis drift can drive a momentum pinch for long-wavelength ITG ($k_\perp \rho_i \ll 1$) and Hahm *et al.* (2007) gave a more general theory of the momentum pinch due to symmetry breaking caused by magnetic curvature. Camenen *et al.* (2009) showed the existence of momentum pinch due to up-down asymmetry theoretically and Camenen *et al.* (2010) also confirmed it experimentally. Important questions concern the effect of the intrinsic torque on the generalized Ohm's law as well as its relation to experimental observations.

V. MAGNETOHYDRODYNAMICS IN THE ADVANCED TOKAMAK REGIME

Magnetohydrodynamics has played an important role in magnetic confinement fusion research since its beginning. Many efforts have been made to overcome MHD instabilities. MHD instabilities are categorized into ideal MHD, neglecting resistive dissipation and wave-particle interaction, resistive MHD, with resistive dissipation, and kinetic MHD, with wave-particle interaction. MHD instabilities in tokamaks are also characterized by global MHD with lower toroidal mode number n and localized MHD with higher n.

Since the beginning of steady-state tokamak research in 1990, important progress in understanding MHD modes related to steady-state tokamaks has been made. In Sec. V.A, we introduce the progress made in ideal MHD stability theory: Spectral properties in Sec. V.A.1, the 1D and 2D Newcomb equations in Sec. V.A.2. In Sec. V.B, we introduce the progress in resistive MHD such as the classical TM in Sec. V.B.1, the neoclassical tearing mode (NTM) in Sec. V.B.2, the double tearing mode (DTM) in Sec. V.B.3, and the resistive wall mode (RWM) in Sec. V.B.4. In Sec. V.C, we describe the progress in the understanding of localized modes such as the infernal mode in Sec. V.C.1, the peeling-ballooning modes in Sec. V.C.2, and the barrier localized mode (BLM) in Sec. V.C.3. In Sec. V.D, we introduce the advances in understanding kinetic MHD focused on the so-called AE to explain the shear Alfvén gap in Sec. V.D.1, various types of AEs in Sec. V.D.2, and nonlinear AE characteristics in Sec. V.D.3. In Sec. V.E, we introduce the stability of CH by showing equilibrium bifurcation in Sec. V.E.1 and resistive stability and the β limit in Sec. V.E.2.

Global ideal MHD modes have a large growth time proportional to the poloidal Alfvén transit time, while resistive MHD modes have a growth time proportional to the resistive diffusion time. Kinetic MHD modes such as AEs may cause selective loss of fast ions such as α particles in the fusion reactor.

A. Progress in linear ideal magnetohydrodynamics

Ideal MHD stability theory has progressed since the establishment of the energy principle by Bernstein *et al.* (1958). An important breakthrough was the ballooning mode theory by Connor *et al.* (1978) which satisfies the double periodic boundary condition using quasimode expansion. Here we

focus on the progress in the spectral properties of MHD, the 2D Newcomb equation, and the flow effect on MHD.

1. Spectral properties in magnetohydrodynamics

The continuous spectrum of ideal MHD has significant importance not only in ideal MHD stability but also in stabilizing the RWM and as a damping mechanism of the AEs. The linearized ideal MHD equation is given by

$$[-\rho\omega^2 - \boldsymbol{F}]\boldsymbol{\xi} = 0, \tag{81}$$

where $\boldsymbol{F}$ is the self-adjoint linear force operator given by Bernstein *et al.* (1958), and ρ, ω, and $\boldsymbol{\xi}$ are the mass density, eigenfrequency, and plasma displacement vector, respectively. Because of this self-adjointness, the spectrum of $\boldsymbol{F}$ is either a point or a continuous spectrum and there is no resolvent spectrum in the linear MHD equation (81) (Kikuchi, 2011b). If some ω^2 gives nontrivial $\boldsymbol{\xi}$ to satisfy Eq. (81), the spectrum is called a point spectrum (in this case, $[-\rho\omega^2 - \boldsymbol{F}]^{-1}$ does not exist). The continuous spectrum is characterized by the existence of the inverse operator $[-\rho\omega^2 - \boldsymbol{F}]^{-1}$ and an unbounded nonsquare integrable eigenfunction.

A well-known linear operator having a continuous spectrum is $(x-\lambda)f = 0$, whose unbounded (nonsquare integrable) eigenfunction is the delta function $f = c\delta(x-\lambda)$, which appears in the linearized Vlasov equation and produces Landau damping. In the linear ideal MHD equation, the linear force operator has a logarithmic singular local eigenfunction $u = \ln(r - r_s)$ [$= \int dr/(r-r_s)$], which is also nonsquare integrable. This type of eigenfunction to produce a continuous spectrum was found for the first time in the electrostatic wave in a nonuniform plasma by Barston *et al.* (1964), analyzed by Sedlacek (1971), and applied to MHD modes by Uberoi *et al.* (1972).

The eigenmode equation in a cylindrical plasma is reduced to first-order ordinary differential equations for the radial displacement $u = r\xi_r$ and the perturbed total pressure $P_1 = p_1 + \boldsymbol{B}_1\cdot\boldsymbol{B}/\mu_0$ as $Ddu/dr = C_1 u - rC_2P_1$ and $DdP_1/dr = C_3u/r - C_1P_1$ (Appert *et al.*, 1974). Here

$$D = \left[\rho\omega^2 - \frac{F^2}{\mu_0}\right]\left[\rho\omega^2\left(\gamma p + \frac{B^2}{\mu_0}\right) - \frac{\gamma p F^2}{\mu_0}\right], \tag{82}$$

and $F = (m - nq)B_\theta/r$, while other quantities are defined by Appert *et al.* (1974). Radial positions satisfying $D = 0$ are called singular points. Because of this singularity, the solution of $u(r)$ includes the nonsquare integrable solution [$u \sim \ln(r - r_s)$] divergent at this singular point. The zeros of the first and second brackets of D are called the shear Alfvén continuum and the sound wave continuum, respectively.

Cheng *et al.* (1986) derived corresponding first-order differential equations in axisymmetric toroidal geometry as follows:

$$\nabla\psi\cdot\nabla\begin{bmatrix} P_1 \\ \xi_\psi \end{bmatrix} = C\begin{bmatrix} P_1 \\ \xi_\psi \end{bmatrix} + D\begin{bmatrix} \xi_s \\ \nabla\cdot\boldsymbol{\xi} \end{bmatrix}, \tag{83}$$

$$E\begin{bmatrix} \xi_s \\ \nabla\cdot\boldsymbol{\xi} \end{bmatrix} = F\begin{bmatrix} P_1 \\ \xi_\psi \end{bmatrix}, \tag{84}$$

where

$$E_{11} = \frac{\omega^2\rho|\nabla\psi|^2}{B^2} + \boldsymbol{B}\cdot\nabla\left(\frac{|\nabla\psi|^2\boldsymbol{B}\cdot\nabla}{B^2}\right), \tag{85}$$

$$E_{12} = 2\gamma p\kappa_s, \qquad E_{21} = 2\kappa_s, \tag{86}$$

$$E_{22} = \frac{\gamma p + B^2}{B^2} + \frac{\gamma p}{\omega^2\rho}\boldsymbol{B}\cdot\nabla\left(\frac{\boldsymbol{B}\cdot\nabla}{B^2}\right), \tag{87}$$

where $\xi_\psi = \boldsymbol{\xi}\cdot\nabla\psi$, $P_1 = p_1 + \boldsymbol{B}_1\cdot\boldsymbol{B}/\mu_0$, $\xi_s = \boldsymbol{\xi}\cdot\boldsymbol{B}\times\nabla\psi/|\nabla\psi|^2$, and other quantities are defined by Cheng *et al.* (1986).

We can solve ξ_s and $\nabla\cdot\boldsymbol{\xi}$ in terms of P_1 and ξ_ψ from Eq. (84). If the inverse operator E^{-1} does not exist, only a nonsquare integrable solution is possible as an eigenfunction of Eq. (83). Such a situation can be found from

$$E\begin{bmatrix} \xi_s \\ \nabla\cdot\boldsymbol{\xi} \end{bmatrix} = 0. \tag{88}$$

Then the corresponding set of eigenvalues ω^2 forms a continuous spectrum, which is the toroidal generalization of $D = 0$ in Eq. (82). The typical solution of Eq. (88) will be shown in Sec. V.D.1.

2. Two-dimensional Newcomb equation

It is important to identify the stability boundary (or marginal stability point) of the tokamak operation. The marginal stability is described by the Newcomb equation which minimizes Bernstein's energy integral. It is called the 1D Newcomb equation in cylindrical plasma (Newcomb *et al.*, 1960) and the 2D Newcomb equation for axisymmetric plasma (Tokuda *et al.*, 1999). In the Newcomb equation, a singular surface is always a rational surface for the concerned mode, while the singular surface changes with ω in the linear MHD equation and is different from the rational surface, in general.

The existence of a continuous spectrum makes it difficult to accurately calculate ω^2 from the linear MHD equation in 1D or 2D [see Eqs. (83) and (84)] near the marginal stability. The marginal stability calculation is improved in the PEST-2 code (Grimm *et al.*, 1983), and similarly in the KINX code (Degtyarev *et al.*, 1997) but is limited to the positive Mercier index case. So it is essential to separate out the nonsquare integrable eigenfunction from the eigenmode equation to evaluate the point spectrum. Pletzer *et al.* (1991) introduced the bell-shaped localization function $H(r)$ ($H = 1$ for $|r - r_0| < \epsilon$ and $H = 0$ for $|r - r_0| > \delta$) to eliminate the big solution part of the eigenfunction. For marginal stability, the 1D Newcomb equation with a single regular singular point in $r \in [0, a]$ is given by (Newcomb *et al.*, 1960)

$$L(\xi) = \frac{d}{dr}\left(f(r)\frac{d\xi}{dr}\right) - g(r)\xi = 0, \tag{89}$$

where $f(r) = f_0(r - r_0)^2 + \cdots$, $f_0 > 0$, $g(r) = g_0 + \cdots$, and $g_0 \neq 0$. $r = r_0$ is a regular singular point. The solution comprises "small" (square integrable with power of $r^{-0.5+\mu}$) and "big" (nonsquare integrable with power of $r^{-0.5-\mu}$) solutions, where $\mu = \sqrt{1/4 + g_0/f_0}$ and $1/4 + g_0/f_0 > 0$ is the Suydam stability criterion. Tokuda *et al.* (1997) converted this marginal stability problem to the eigenvalue

problem by keeping the behavior of the eigenfunction near the regular singular point as follows:

$$L(\xi) = -\lambda\rho\xi, \qquad \rho = \rho_0(r - r_0)^2. \tag{90}$$

This equation is similar to the Sturm-Liouville equation for string vibration [f(~elastic modulus) > 0] (Courant, 1953). But f can be zero or positive in our case. As such this equation is not the Sturm-Liouville equation in the exact sense. The choice of this functional form for ρ does not change the leading singularity of the eigenfunction near the regular singular point [μ does not change since $\rho(r_0) = 0$] and this equation coincides with the Newcomb equation at marginal stability ($\lambda = 0$).

As in the case of a cylindrical plasma, the energy integral inside the plasma is minimized under the incompressibility condition $\nabla \cdot \boldsymbol{\xi} = 0$ in the case of an axisymmetric torus. By using $X = \boldsymbol{\xi} \cdot \nabla r$ and $V = r\boldsymbol{\xi} \cdot \nabla(\theta - \zeta/q)$ in the flux coordinates (r, θ, ζ) with $r = [2R_0 \int_0^{\psi}(q/F)d\psi]^{1/2}$, the energy integral W_p can be expressed in the following form (Tokuda *et al.*, 1999):

$$W_p = \frac{\pi}{2\mu_0}\int_0^1 dx \int_0^{2\pi} d\theta L\left(X, \frac{\partial X}{\partial\theta}, \frac{\partial X}{\partial x}, V, \frac{\partial V}{\partial\theta}\right). \tag{91}$$

Here $x = r/a = 1$ is the plasma surface and L is the Lagrangian as given by Tokuda *et al.* (1999). The absence of the $\partial V/\partial x$ term in L leads to the following Euler-Lagrange equation for V:

$$\frac{\partial}{\partial\theta}\left[\frac{\partial L}{\partial(\partial V/\partial\theta)}\right] - \frac{\partial L}{\partial V} = 0. \tag{92}$$

Integration of the above equation in $\theta = [0, 2\pi]$ leads to the following solvable condition:

$$\int_0^{2\pi}\frac{\partial L}{\partial V}d\theta = 0. \tag{93}$$

Fourier expansions of X and V for θ are defined as $X(x, \theta) = \sum X_m(x)e^{im\theta}$, and $V(x, \theta) = -i\sum V_m(x)e^{im\theta}$ Substitution of these equations into Eqs. (92) and (93) gives linear equations for V_m. The solution is substituted into the energy integral. The energy integral is now given by $\boldsymbol{Y} = x\boldsymbol{X}$, $\boldsymbol{X} = (\ldots, X_{-2}, X_{-1}, X_0, X_1, X_2, \ldots)^t$ (t indicates transposed) in the following form:

$$W_p[\boldsymbol{Y}] = \int_0^1 \hat{L}\left(\boldsymbol{Y}, \frac{d\boldsymbol{Y}}{dx}\right)dx. \tag{94}$$

This leads to the following Euler-Lagrange equation to minimize the energy integral:

$$\frac{d}{dx}\frac{\partial\hat{L}}{\partial(d\boldsymbol{Y}/dx)} - \frac{\partial\hat{L}}{\partial\boldsymbol{Y}} = 0. \tag{95}$$

Since $\hat{L}$ is given by a quadratic form of $\boldsymbol{Y}$ and $d\boldsymbol{Y}/dx$, the Euler-Lagrange equation is reduced to the following form of second-order ordinary differential equation:

$$\boldsymbol{N}(\boldsymbol{Y}) \equiv \frac{d}{dx}\boldsymbol{f}\frac{d\boldsymbol{Y}}{dx} + \boldsymbol{g}\frac{d\boldsymbol{Y}}{dx} + \boldsymbol{h}\boldsymbol{Y} = 0, \tag{96}$$

where $\boldsymbol{f}$, $\boldsymbol{g}$, and $\boldsymbol{h}$ are constant $(2M + 1) \times (2M + 1)$ matrices. Here M is the number of Fourier harmonics. This is called the two-dimensional Newcomb equation. Diagonal elements of $\boldsymbol{f}$ have $(n/m - 1/q)^2$ dependence similar to that in the one-dimensional Newcomb equation, and the radius of $q = m/n$ is the regular singular point. Small and big solutions exist near the singular point and the Mercier condition is derived as the local stability condition. Once the Mercier condition is met, kink and peeling modes can be studied using this two-dimensional Newcomb equation. Tokuda *et al.* (1999) converted this 2D Newcomb equation into an eigenvalue equation by adding an artificial kinetic energy integral term as follows:

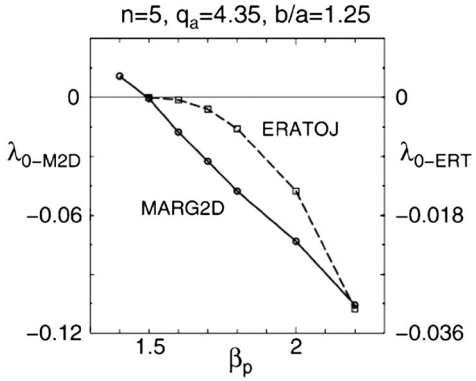

FIG. 29. Comparison of ERATO-J and MARG2D simulations for identifying the stability boundary. From Aiba *et al.*, 2006.

$$W[\boldsymbol{Y}] = W_p - \lambda W_k, \tag{97}$$

$$W_k = 2\pi^2\int\sum_m \rho_m(\hat{r})|Y_l(\hat{r})|^2 dx, \tag{98}$$

$$\rho_m(x) = \begin{cases} F^2(\frac{m}{q} - n), & m = nq(r_0), \\ F^2, & m \neq nq(r_0). \end{cases} \tag{99}$$

This choice of ρ_m conserves the leading singularity of the eigenfunction at the singular radius. The Euler-Lagrange equation to minimize the energy integral $W[\boldsymbol{Y}]$ is given as

$$\boldsymbol{N}_\lambda\boldsymbol{Y} = [\boldsymbol{N} + \lambda\,\mathrm{diag}(\rho_m(x))]\boldsymbol{Y} = 0. \tag{100}$$

The linear operator $\boldsymbol{N}_\lambda$ is related to the 2D Newcomb operator as $\boldsymbol{N}_\lambda = \boldsymbol{N} + \lambda\,\mathrm{diag}(\rho_m(x))$. Here $\mathrm{diag}(\rho_m(x))$ is the diagonal matrix having $\rho_m(x)$ as its (m, m) component. This equation is a quasi-Sturm-Liouville equation as in the 1D case.

MARG2D (Tokuda *et al.*, 1999) solves Eq. (100) to identify the stability boundary. The code is extended to the free-boundary mode by inclusion of a vacuum solution by Aiba *et al.* (2006). Figure 29 shows a comparison of MARG2D and ERATO-J (Azumi *et al.*, 1981) in identifying the critical β_p value for stability. While the stability boundary is not quite sharp in ERATO-J, MARG2D can determine a sharp stability boundary.

3. Flow effect on ideal magnetohydrodynamics

Active use of plasma flow to stabilize global MHD modes (especially the RWM in Sec. V.B.4) is important for all advanced tokamak regimes (WS, NS, and CH). But the

inclusion of flow brings quite rich physics to ideal MHD stability theory.

The effect of flow on toroidal equilibrium was investigated by Zehrfeld *et al.* (1972). Since poloidal rotation is small due to viscous damping, only toroidal rotation can be of the order of the sound velocity. Plasma pressure is no longer a flux function [$P = P(\psi, R)$] and the Grad-Shafravov equation (1) is modified (Hameiri *et al.*, 1983) as

$$\frac{\partial^2\psi}{\partial R^2} - \frac{1}{R}\frac{\partial\psi}{\partial R} + \frac{\partial^2\psi}{\partial Z^2} = -\mu_0 R^2 \frac{\partial P}{\partial\psi}\bigg|_R - F\frac{dF}{d\psi}. \quad (101)$$

The linearized equation of motion with mass flow was given by Frieman *et al.* (1960) and is called the Frieman-Rotenberg (FR) equation:

$$\rho\frac{\partial^2\boldsymbol{\xi}}{\partial t^2} + 2\rho(\boldsymbol{u}\cdot\nabla)\frac{\partial\boldsymbol{\xi}}{\partial t} = \boldsymbol{F}(\boldsymbol{\xi}), \quad (102)$$

$$\boldsymbol{F} = \boldsymbol{F}_s(\boldsymbol{\xi}) + \boldsymbol{F}_d(\boldsymbol{\xi}), \quad (103)$$

$$\boldsymbol{F}_s(\boldsymbol{\xi}) = \nabla[\boldsymbol{\xi}\cdot\nabla P + \gamma P\nabla\cdot\boldsymbol{\xi}] + (\nabla\times\boldsymbol{B}_1)\times\boldsymbol{B} + \boldsymbol{J}\times\boldsymbol{B}_1, \quad (104)$$

$$\boldsymbol{F}_d(\boldsymbol{\xi}) = \nabla\cdot[\rho\boldsymbol{\xi}(\boldsymbol{u}\cdot\nabla)\boldsymbol{u} - \rho\boldsymbol{u}(\boldsymbol{u}\cdot\nabla)\boldsymbol{\xi}], \quad (105)$$

$$\boldsymbol{B}_1 = \nabla\times(\boldsymbol{\xi}\times\boldsymbol{B}). \quad (106)$$

Both $\boldsymbol{F}_s$ and $\boldsymbol{F}_d$ are Hermite operators but the convective term $2\rho(\boldsymbol{u}\cdot\nabla)\partial\boldsymbol{\xi}/\partial t$ is an anti-Hermitian operator, and the system as a whole is not self-adjoint. While the ω spectrum of the Hermite MHD operator lies on a real or imaginary axis, the spectrum of the FR equation spreads in the complex plane, causing some difficulty in searching for the eigenvalue. Moreover, the eigenvalue analysis may fail to identify the most unstable solution when the time evolution of this solution is no longer $\exp(\lambda t)$. MHD stability codes treating toroidal flow have been developed during the 1990s including MARS by Chu *et al.* (1999) and more recently MINERVA by Aiba *et al.* (2011) and CASTOR-FLOW by Chapman *et al.* (2011). If we can assume $\boldsymbol{\xi} = \hat{\boldsymbol{\xi}}\exp(\lambda t)$, the eigenvalue $\lambda = \gamma + in\omega$ (γ is the growth rate, ω is the real frequency, and n is the toroidal mode number) including toroidal and poloidal flows can be expressed as (Chu *et al.*, 1999; Aiba *et al.*, 2011)

$$\gamma^2 = \frac{\delta W_{g1}}{\delta K} - n^2\omega^2, \qquad in\omega = -\frac{\delta W_c}{\delta K}, \quad (107)$$

$$\delta K = \langle\hat{\boldsymbol{\xi}}|\rho|\hat{\boldsymbol{\xi}}\rangle, \quad (108)$$

$$\delta W_{g1} = -\langle\hat{\boldsymbol{\xi}}|\boldsymbol{F}(\hat{\boldsymbol{\xi}})\rangle + \langle\hat{\boldsymbol{\xi}}|\rho(\boldsymbol{u}\cdot\nabla)(\boldsymbol{u}\cdot\nabla)|\hat{\boldsymbol{\xi}}\rangle, \quad (109)$$

$$\delta W_c = \langle\hat{\boldsymbol{\xi}}|\rho(\boldsymbol{u}\cdot\nabla)|\hat{\boldsymbol{\xi}}\rangle. \quad (110)$$

The spectral and singular structures of this equation have been investigated in depth by Hirota *et al.* (2008). They extended the definition of wave energy in a bounded plasma including a continuous spectrum using the action-angle formulation, where the wave energy is given by $\omega_n\mu_n$ for the discrete mode and by $\int\omega\mu(\omega)d\omega$ for the continuous mode. The energy integral in the ideal MHD theory is represented by the sum of these wave energies. In a flowing plasma, the wave energy can be negative and its interaction with positive dissipation at the wall may destabilize the mode. Also, resonance causes continuum damping if the wave energies of continuous and discrete modes have the same sign, while resonant instability occurs if they have different signs.

B. Resistive magnetohydrodynamics

1. Classical tearing mode

The TM is an important resistive instability associated with the reconnection of the magnetic field at the resonant rational surface $r = r_s$. This mode is destabilized by changing the topology of the magnetic field, while it is stable within the ideal MHD context. The linear growth rate of this mode is given by Furth *et al.* (1963) as $\gamma \sim \eta^{3/5}$ (or $\gamma \sim S^{-3/5}$, where $S = \mu_0 a v_A/\eta = \tau_R/\tau_A$ is the Lundquist number, $\tau_R = \mu_0 a^2/\eta$ the resistive diffusion time, $\tau_A = a/v_A$ the Alfvén transit time, and $v_A = B/\sqrt{\mu_0 n_i m_i}$ the Alfvén velocity).

But it soon goes into the nonlinear region, called the Rutherford regime (Rutherford *et al.*, 1973), where the time evolution of the magnetic island width $w = 4\sqrt{\psi_1(r_s)/\psi_0''(r_s)}$ is governed by the Rutherford equation under the approximation of constant ψ [i.e., first-order perturbed flux function $\psi_1(r_s) \neq 0$] and improved by Biskamp (1993) as follows:

$$\frac{dw}{dt} = \frac{1.22\eta}{\mu_0}\Delta'(w) \quad (111)$$

with $\Delta'(w) = [\psi_1'(r_s + w/2) - \psi_1'(r_s - w/2)]/\psi_1(r_s)$.

The island structure of the TM was observed using tomography by Sauthoff *et al.* (1978) and radial phase inversion of the TM structure was measured by Robinson *et al.* (1979). This mode is important for all tokamak regimes including advanced tokamak operation.

Stabilization of the tearing mode by electron cyclotron heating.—Suppression of the $m/n = 2/1$ TM using direct island heating was shown for the first time in 1992 by Hoshino *et al.* (1992) and followed by its observation at many other tokamaks (TEXT, WT-3, T-10, FTU, TEXTOR, HL-2A, and TCV). Since magnetic island formation produces temperature flattening by its shortcircuit effect, heating near the magnetic island, especially at the O point, has a stabilizing effect as shown by Yoshioka *et al.* (1984) and shown in a reduced resistive MHD simulation by Kurita *et al.* (1994). The heating effect on the Rutherford equation is expressed by adding an additional term to Eq. (118) as follows:

$$\frac{dw}{dt} = \frac{1.22\eta}{\mu_0}\Delta'(w) + C_2\frac{J_0}{\tilde{\psi}_m}\int_{-w/2}^{w/2}\tilde{\eta}_m dr, \quad (112)$$

where C_2, J_0, $\tilde{\eta}_m$, and $\tilde{\psi}_m$ are a constant of the order of 1, the equilibrium current density, the perturbed resistivity, and the perturbed poloidal flux function, respectively. Since $\tilde{\eta}_m < 0$ with ECH, the second term on the right-hand side is stabilizing.

2. Neoclassical tearing mode

Efficient steady-state operation of the tokamak relies on the maximum utilization of the bootstrap current. But this leads to an important new instability, called the neoclassical tearing mode (Carrera *et al.*, 1986).

Since the bootstrap current is proportional to the pressure gradient ($J_{bs} \sim dP/dr$), local flattening of the pressure gradient near the magnetic island produces a negative perturbed helical current, which enhances the magnetic island and destabilizes the TM in the positive-shear regime, while this negative perturbed helical current reduces the magnetic island size and is stabilizing in the negative-shear regime (Kikuchi, 2011b). Therefore, this NTM is important for all advanced tokamak operating regimes (WS, NS, and CH) except in regions of negative shear.

This NTM was observed for the first time in TFTR by Chang *et al.* (1995) (see Fig. 30) and explained well by the Rutherford equation including the bootstrap destabilization term but it cannot be explained without including the bootstrap destabilization term.

The Rutherford equation including this bootstrap destabilization effect with polarization effect (or finite Larmor radius effect $w_{pol} \sim \rho_{pi}$) (Waelbloeck *et al.*, 2001) and finite perpendicular transport [$w_d \sim (\chi_\perp/\chi_\parallel)^{1/4}$] (Fitzpatrick *et al.*, 1995) is given by (La Haye *et al.*, 2006)

$$\frac{dw}{dt} = \frac{1.22\eta}{\mu_0}\left[\Delta'(w) + \epsilon^{1/2}\frac{L_q}{L_p}\frac{\beta_p}{w}\left(\frac{w^2}{w^2+w_d^2} - \frac{w_{pol}^2}{w^2}\right)\right], \tag{113}$$

where $\epsilon = r/R$, $L_q = q/(dq/dr)$, $L_p = p/(dp/dr)$, and β_p is the poloidal beta value. The characteristic transport effect island width is given by $w_d = 5.1(qL_q/\epsilon k_\theta)^{1/2}(\chi_\perp/\chi_\parallel)^{1/4}$ (Fitzpatrick *et al.*, 1995), where the poloidal wave number $k_\theta = m/r$, and $\chi_\perp$ and $\chi_\parallel$ are perpendicular and parallel heat diffusivities, respectively. The characteristic threshold island width $w_{pol} = (L_q/L_p)^{1/2}\epsilon^{1/2}\rho_{\theta_i}$.

A more sophisticated formula with nondivergent polarization term at $w = 0$ and other terms was given by Sauter *et al.* (2002). Even if the equilibrium is stable to the classical TM $\Delta'(0) \le 0$, the NTM can be destabilized at finite island width $w \ge w_{crit}$. As such we need a seed island to destabilize NTM.

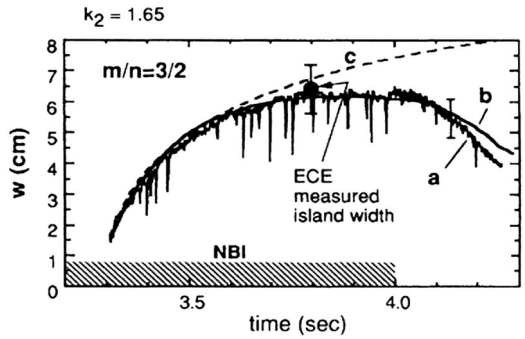

FIG. 30. Observation of $m/n = 3/2$ NTM at TFTR. (a) Measured evolution of island width, (b) calculated island width using modified Rutherford equation, and (c) calculated island width with fixed parameters (η, $w_c \equiv \epsilon^{1/2}L_q\beta_p/L_p$, Δ'). From Chang *et al.*, 1995.

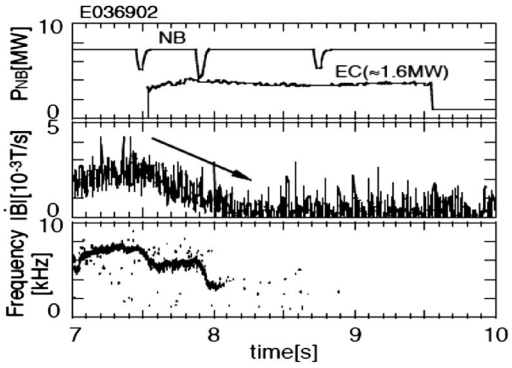

FIG. 31. Stabilization of NTM for fundamental O-mode ECCD. From Isayama *et al.*, 2000.

The loss of the bootstrap current inside the magnetic island is essential for the NTM. Direct measurement of this loss of bootstrap current inside the magnetic island was made using MSE diagnostics at JT-60U by Oikawa *et al.* (2005).

a. Stabilization of the neoclassical tearing mode by electron cyclotron current drive

Localized ECCD inside a magnetic island can compensate the lost bootstrap current to stabilize NTM. First complete NTM stabilization was demonstrated at ASDEX-U using the second-order harmonic X-mode ECCD by Gantenbein *et al.* (2000) and at JT-60U using the fundamental O-mode ECCD by Isayama *et al.* (2000) as shown in Fig. 31.

Benchmarking of the modified Rutherford equation for ECCD stabilization of NTM is important for its extrapolation to ITER control (Sauter *et al.*, 1997). Efforts have been successful in calibrating the coefficients (Hayashi *et al.*, 2004a) and the result was successfully applied to radial scanning experiments (Isayama *et al.*, 2007) (see Fig. 32)

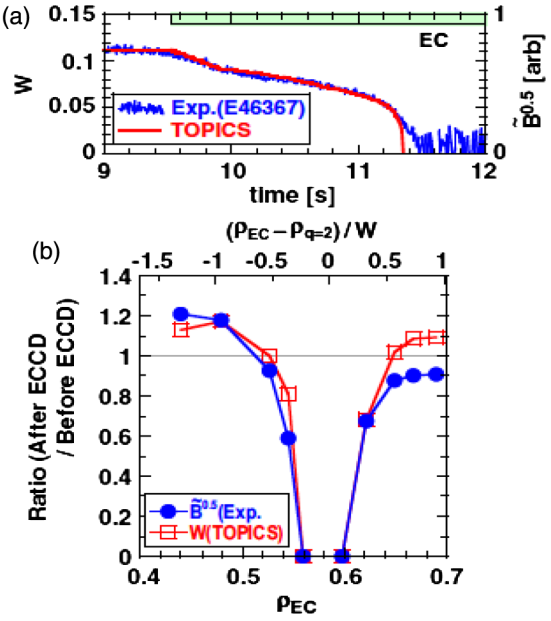

FIG. 32 (color online). Comparison of experimental measurement and numerical calculation based on the modified Rutherford equation. From Isayama *et al.*, 2007.

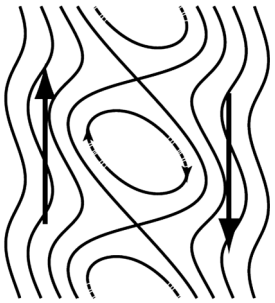

FIG. 33. Distortion of the tearing island due to viscous drag. From La Haye *et al.*, 2009.

and provided the power requirement (Hayashi *et al.*, 2004b) at ITER. The effect of EC power on achievable Q was discussed by Sauter *et al.* (2010).

b. Flow effect on the neoclassical tearing mode

The magnetic island can be distorted by the viscous drag of flow shear as shown in Fig. 33 and has a stabilizing effect on the classical TM and the NTM (Smolyakov *et al.*, 2001). Therefore not only flow shear but also perpendicular viscosity ν is important in stabilizing the TM and NTM in the high-temperature tokamak regime. A systematic simulation by Goelho *et al.* (2007) showed that the magnetic Prandtl number $\Gamma = \tau_R/\tau_V \gg 1$ is a necessary condition and the Lundquist number $S = \tau_R/\tau_A \gg 1$ is also important to enhance stabilization by flow shear, where the viscous time is given by $\tau_V = m_i n_i a^2/\nu$.

Except for JT-60U, most medium to large tokamaks use tangential neutral beam injection, which drives cotoroidal rotation. After the reorientation of tangential NBI, Buttery *et al.* (2008) and La Haye *et al.* (2009) showed that NTM is "destabilized" with reduced toroidal rotation using a combination of corotation or counterrotation NB injection capability at DIII-D. The NTM onset β_N is reduced with reduced corotation associated with weaker absolute negative rotation shear ($d\Omega_\zeta/dr < 0$), where $\Omega_\zeta = \boldsymbol{u}_{i0} \cdot \nabla\zeta$. The 2/1 NTM onset β_N data including NSTX results show better correlation with normalized flow shear $n_{\rm FS} = -L_s \tau_A d\Omega_\zeta/dr$, where $L_s = qL_q/\epsilon$ (La Haye *et al.*, 2010).

3. Double tearing mode

While the NS operation showed excellent plasma confinement exceeding $Q_{\rm DT}^{eq} = 1$ at JT-60U (Ishida *et al.*, 1997), the plasma is disrupted by ideal and resistive MHD modes. While NS can be stable to ideal MHD if the pressure profile is optimized, strong ITB near $q_{\rm min}$ may destabilize ideal MHD instabilities, as discussed in Sec. V.C.1. This mode of operation can also be unstable to the DTM where there are two rational surfaces in the plasma.

The stability of the DTM was analyzed for the cylindrical tokamak by Furth *et al.* (1973). The DTM is a possible cause of rapid current penetration and disruptive instability during the current ramp (Stix *et al.*, 1976). Formation of the hollow current profile and its rapid relaxation associated with the $m/n = 4/1$ mode was observed by Hutchinson *et al.* (1976).

The radial proximity of two rational surfaces $\Delta r_s/2a$ is an important parameter for the DTM, where eigenfunctions of

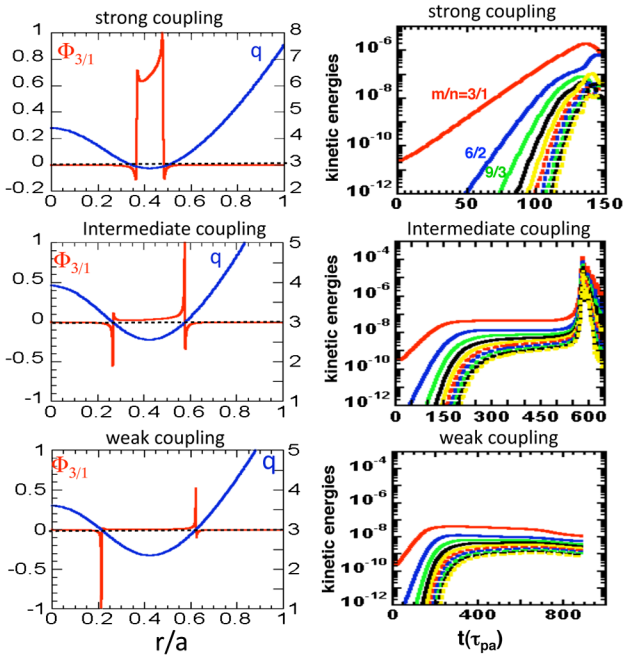

FIG. 34 (color online). Comparison of linear radial eigenmode structures among small (strong coupling), intermediate, and large (weak coupling) Δr (left panel) and nonlinear time evolution of kinetic energies of $m/n = 3/1, 6/2, 9/3, \ldots$ (right panel). From Ishii *et al.*, 2000.

the inner and outer TMs are coupled to form a DTM if $\Delta r_s/2a$ is sufficiently small. In this case, the linear growth rate follows $m = 1$ internal resistive TM scaling, $\gamma \sim \eta^{1/3}$. If the radial separation $\Delta r_s/2a$ is large, the modes at the two rational surfaces are decoupled and the linear growth rate of the mode follows TM scaling, $\gamma \sim \eta^{3/5}$.

Pritchett *et al.* (1980) derived the dispersion relation for the DTM in sheet pinch as

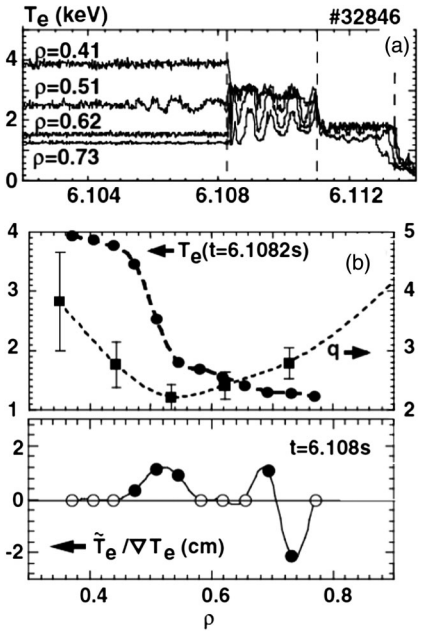

FIG. 35. (a) Time evolution of disruptive TM in NS discharge; (b) T_e, $\tilde{T}_e$, and q profiles just before collapse. From Takeji *et al.*, 2002a.

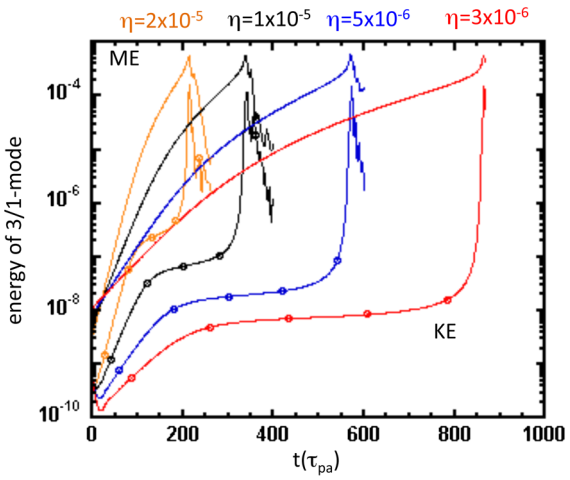

FIG. 36 (color online). Time evolution of nonlinear DTM for intermediate Δr for different resistivity η. ME and KE are the magnetic and kinetic energy, respectively. From Ishii *et al.*, 2000.

$$\frac{\hat{\lambda}^{5/4}\hat{\lambda}_h\Gamma[(\hat{\lambda}^{3/2}-1)/4]}{\Gamma[(\hat{\lambda}^{3/2}+5)/4]}=8, \tag{114}$$

where the scaled resistive growth rate $\hat{\lambda}$ and the ideal MHD driving energy $\hat{\lambda}_h$ are given as

$$\hat{\lambda}=\gamma\tau_h[S/\alpha^2(dB_0/dx)^2]^{1/3}, \tag{115}$$

$$\hat{\lambda}_h=\gamma_h\tau_h[S/\alpha^2(dB_0/dx)^2]^{1/3}. \tag{116}$$

Pritchett *et al.* (1980) also derived a coupling condition for the DTM and it may be given for a cylindrical plasma as $\Delta r_s/2a<(ma/r_s)^{-7/9}S^{-1/9}$, where S is the Lundquist number.

Ishii *et al.* (2000) analyzed linear and nonlinear behaviors of the DTM to understand characteristics of JT-60U NS plasmas. In the case $\Delta r<0.15$, a strong mode coupling occurs and the growth rate $\gamma\sim\eta^{1/3}$, while in the case $\Delta r>0.32$, a weak mode coupling occurs and the growth rate $\gamma\sim\eta^{3/5}$. The regime $0.15<\Delta r<0.32$ is called the intermediate regime.

Figure 34 (left panel) shows a radial linear eigenmode structure of the DTM for the small-Δr, intermediate-Δr, and large-Δr cases. It is clear that the radial eigenmode is not always coupled between two rational surfaces and can have weak coupling if the separation is large enough. Figure 34 (right panel) shows the nonlinear DTM time evolution of the kinetic energies of various m/n modes. In the case of small Δr, the mode grows exponentially until the collapse. In the case of large Δr, the mode goes into the Rutherford regime and saturates. On the other hand, nonlinear destabilization of the DTM is found in the intermediate regime, which is attributed to a new type of reconnection discussed later.

Takeji *et al.* (2002a) identified two types of resistive instabilities in JT-60U NS plasma. One is a nondisruptive resistive interchange mode and the other is a disruptive TM shown in Fig. 35. In the former case, temperature fluctuation was observed only near the inner rational surface (typically $q=3$) showing no phase inversion across the rational surface, and the stability criterion of the resistive interchange mode D_R (Glasser *et al.*, 1975) is violated ($D_R>0$). These observations are consistent with the resistive interchange mode. The observation of the resistive interchange mode was first reported in DIII-D by Chu *et al.* (1996) at $\beta_N=1.5$, resulting in disruption and showing the importance of a pressure peaking factor, while this resistive interchange mode in JT-60U at $\beta_N<1$ does not lead to disruption.

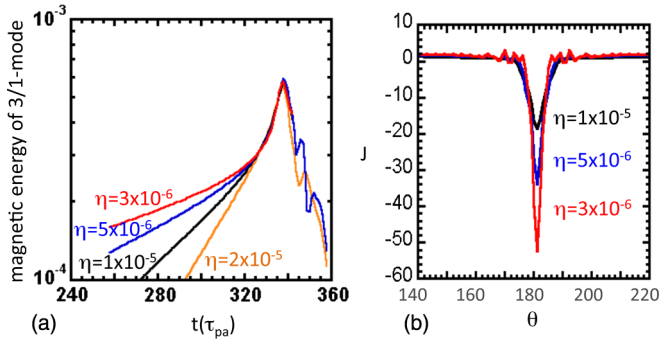

FIG. 37 (color online). (a) Time evolution of the $\frac{3}{1}$ magnetic energy in nonlinearly destabilized DTM for various plasma resistivities η; (b) current distributions for various plasma resistivities. From Ishii *et al.*, 2002.

For the latter case, precursor oscillation is observed before thermal collapse. The temperature perturbation $\tilde{T}_e$ just before the first thermal collapse shows clear phase inversion near the outer $q=3$ surface with a growth time of $\gamma^{-1}\sim 0.5$ ms, indicating a TM, and no fluctuation near the inner $q=3$ surface (Takeji *et al.*, 2002a).

Ishii *et al.* (2003) investigated the resistive instability in a toroidal geometry under the condition of $D_R>0$ near the inner $q=3$ surface, showing that the mode structure is not interchangeable but is a DTM, and they concluded that the existence of the Rutherford regime may cause precursor oscillation and that nonlinearly destabilized DTMs later may go to a thermal quench by an the explosive instability. Ishii *et al.* (2009) further investigated the effect of toroidal flow and external magnetic perturbation, showing that an inner magnetic island may disappear. Another important effect is the loss of the bootstrap current inside the magnetic island (NTM effect on the DTM) since the loss of the bootstrap current has a stabilizing effect on the negative-shear

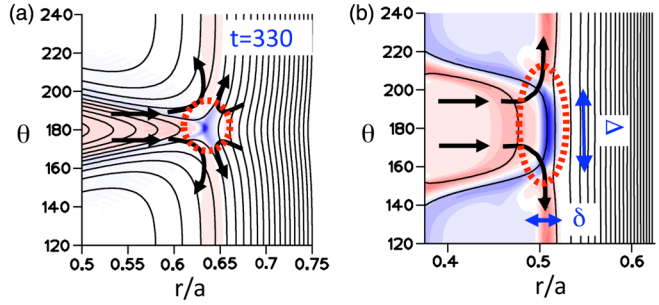

FIG. 38 (color online). Contour plot of current distribution for (a) nonlinearly destabilized DTM (point current) and (b) standard DTM (sheet current). From Ishii *et al.*, 2002.

($s < 0$) regime and a destabilizing effect on the positive-shear ($s > 0$) regime (Kikuchi, 2011b), which may lead to a single TM at rational surfaces in the positive-shear region. This is left for future study. Experimental analysis of the *O* mode at TCV (Turri *et al.*, 2008) showed that the *O* mode is a cyclic phenomenon due to magnetic-island-induced transport enhancement.

a. New fast-reconnection paradigm

Magnetic reconnection is one of the most important subjects in plasma physics. Fast reconnection observed in a solar flare has been a mystery since the usual Sweet-Parker sheet reconnection does not have a fast reconnection time (Biskamp, 2000).

As shown in Fig. 36, for sufficiently low resistivity η, a slowly growing Rutherford-regime-like phase is seen after the initial linear growth, and it changes to an explosive growth phase. The period of the Rutherford regime increases with lower resistivity η. The magnetic reconnection process in this nonlinearly destabilized DTM has marked differences from the usual Sweet-Parker sheet reconnection. The growth rate of the above nonlinearly destabilized DTM does not have any dependence on plasma resistivity η in the final stage [see Fig. 37(a)]. The peak current associated with the magnetic island increases with reduced plasma resistivity so that $\eta j =$ const [see Fig. 37(b)]. Ishii *et al.* (2002) showed that the magnetic island becomes more triangular shaped and the current distribution associated with the magnetic island is concentrated both poloidally and radially (point current) [see Fig. 38(a)] in the case of the nonlinearly destabilized DTM. On the other hand, the standard strongly coupled DTM [see Fig. 38(b)] has a sheet current distribution during explosive growth similar to the Sweet-Parker reconnection. Wang *et al.* (2007) showed this fast reconnection can occur in slab geometry with $\eta^{1/5}$ dependence. Janvier *et al.* (2011) explained this as a secondary instability.

4. Resistive wall modes

All advanced tokamak operating regimes (WS, NS, and CH) for steady-state tokamak operation require wall stabilization or are benefitted by an increase in the operating plasma beta value by wall stabilization.

When the steady-state tokamak reactor was proposed in 1990, most people believed that wall stabilization would not work for realistic tokamak circumstances since the wall necessarily had finite resistance and penetration of the magnetic field would nullify wall stabilization. Even if the plasma were rotating in the toroidal direction, it was pointed out that the mode (called the RWM) is attached to the wall and the mode will slip with respect to the plasma rotation; hence wall stabilization will not work for a long time as shown by Gimblett *et al.* (1986) and Hender *et al.* (1989). But, the existence of the continuous spectrum provided a collisionless damping mechanism for the RWM.

Recently, Chu *et al.* (2010) gave a comprehensive review of RWMs. Splitting of the rational and singular surfaces in flowing plasma brings some difficulty to RWM theory and Shiraishi *et al.* (2011) developed an accurate analytical dispersion relation.

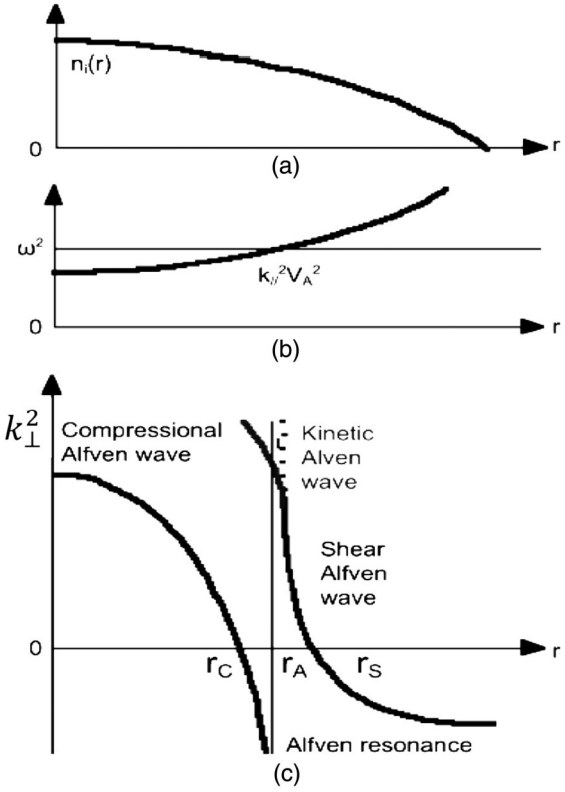

FIG. 39. (a) Density profile, (b) shear Alfvén wave, and (c) shear Alfvén wave modified to KAW.

a. Shear Alfvén wave continuous damping

The shear Alfvén wave has a continuous spectrum in the inhomogeneous plasma and provides strong collisionless damping as shown by Hasegawa *et al.* (1974) due to phase mixing or through mode conversion to the kinetic Alfvén wave (KAW) (Hasegawa *et al.*, 1976). A basic diagram of the shear Alfvén resonance (SAR) is shown in Fig. 39.

The ideal MHD equation has a singularity [see Eq. (82)] for the SAR $\omega = k_\parallel V_A$ at $r = r_A$, where $k_\parallel B = nB_\zeta/R - mB_\theta/r$. Since the density has a radial variation, SAR occurs for a range of ω, which constitutes a continuous spectrum and provides a collisionless wave absorption mechanism, where the eigenfunction of the displacement is given by $\xi = c\ \ln(r - r_A)$ $(r > r_A)$ and $\xi = c(\ln(r_A - r) + i\pi)$ $(r < r_A)$.

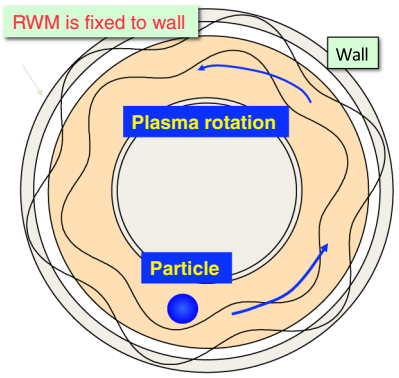

FIG. 40 (color online). Relation among rotating plasma, resistive wall mode, and wall.

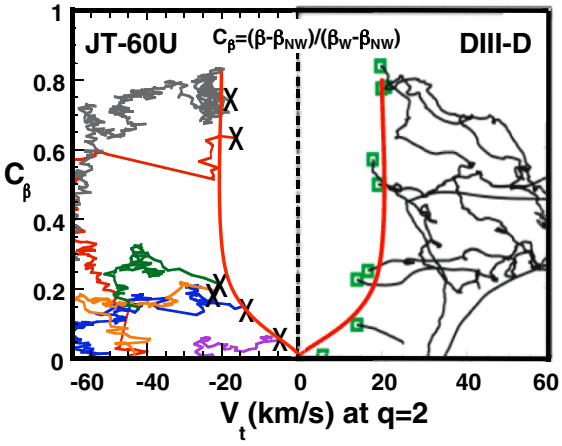

FIG. 41 (color online). Discharge trajectories of DIII-D and JT-60U in the $(V_t|_{q=2}, C_\beta)$ plane. The X's and boxes show onsets of RWM. From Garofalo *et al.*, 2007 and Takechi *et al.*, 2007.

This imaginary part of the eigenfunction appears from the analytical continuation of the solution in $r > r_A$.

Damping of the KAW occurs mainly through electron Landau damping for a low-beta plasma (Hasegawa *et al.*, 1976). Mode conversion of the shear Alfvén wave to the KAW and its damping was confirmed by Weisen *et al.* (1989) by excitation of the shear Alfvén wave using the external antenna structure in the TCA tokamak.

b. Stabilization of the resistive wall mode in tokamaks

In a rotating tokamak, the RWM is fixed to the wall and the rotating plasma will slip with respect to the mode (see Fig. 40). The plasma in the rotating frame experiences the RWM as a traveling wave and undergoes resonant wave-particle interaction to damp this traveling wave by phase mixing of the continuum modes (or by Landau damping of the KAW produced by the mode conversion of the shear Alfvén wave).

Reimerdes *et al.* (2007) at DIII-D and Takechi *et al.* (2007) at JT-60U showed that the RWM is stabilized with a small toroidal rotation. Both machines showed that the critical rotation speed is rather small at ~20 km/s, which is ~0.3% of the Alfvén velocity (see Fig. 41). This critical velocity to stabilize the RWM is close to the value expected from the continuous damping of the Alfvén wave (Reimerdes *et al.*, 2007). Such low toroidal rotation may be driven by so-called intrinsic rotation. While small toroidal rotation may stabilize RWM in ITER and the demonstration power reactor (DEMO), such rotation may be decelerated due to mode locking. In this case, rotational wall stabilization may be ineffective. To ensure wall stabilization, active feedback control of the RWM using sector coils is important. Stabilization of the RWM in a high-β, low-toroidal-rotation plasma was successfully demonstrated by Sabbagh *et al.* (2006).

c. Energetic particle driven wall mode

While the RWM can be stabilized with toroidal rotation of >0.3% of Alfvén velocity, a different bursting MHD instability was observed by Matsunaga *et al.* (2009) in the beta regime between the no-wall and wall beta limits. This mode was excited by the interaction of trapped energetic particles with a marginally stable mode in the wall-stabilized high-β_N regime. This observation is explained as a fishbonelike bursting mode with threshold energetic particle beta $\beta_c^* = 0.141$ ($\beta^* = \beta_h/\beta$) by Hao *et al.* (2011). For a review of energetic particle modes, see Chen *et al.* (2007).

d. Ferromagnetic wall effect on resistive wall modes

The use of ferritic material in fusion DEMO and beyond is closely related to the choice of blanket structural material. Since reduced activation ferritic (RAF) steel is a primary candidate for the blanket structural material, the effect of magnetization on the RWM is an important subject. Ferromagnetism attracts the perturbed magnetic field to the wall and may destabilize the RWM. Kurita *et al.* (2006) found that on the order of 8% reduction in the beta limit is expected for effective relative permeability $\mu_r = \mu/\mu_0 = 2$.

C. Localized magnetohydrodynamics

A plasma pressure profile does not always follow the optimum profile to achieve high beta. Improved confinement in tokamaks is frequently associated with local steep improved confinement layers such as an ETB in the *H* mode and ITB in WS (Koide *et al.*, 1994) and NS (Fujita *et al.*, 1997b). These local transport barriers are useful to achieve reactor relevant confinement but are not favorable to achieve a plasma pressure sufficient for the large bootstrap current fraction and high fusion power density as required from the reactor design (Kikuchi, 1993).

In the case of WS, the so-called ballooning formulation breaks down and intermediate-*n* modes [called infernal modes (Manickam *et al.*, 1987)] may play an important role in the central MHD activity and sometimes lead to β_p collapse.

With the development of ETB, the so-called edge localized mode (ELM) becomes unstable, which is effective in reducing impurity accumulation in the core but becomes serious for the power handling of divertor plates in ITER and beyond due to its excessive heat flux. The edge plasma becomes more collisionless in ITER and beyond and the localized bootstrap current is driven in the edge region. This edge bootstrap current as well as the steep pressure gradient destabilizes ideal MHD modes localized at the edge region, called peeling modes (Manickam *et al.*, 1992). In the case of ITB, the BLM is destabilized when the pressure gradient of ITB exceeds the stability limit (Takeji *et al.*, 1997; Manickam *et al.*, 1999).

1. Infernal mode in advanced tokamak operation

Advanced tokamak operations in WS and NS plasmas are associated with core improved confinement. Large pressure gradients in the core weak-shear regime in WS and the pitch minimum regime in NS lead to the loss of magnetic shear stabilization of pressure-driven ideal MHD modes. In these regimes, both $n = 1$ and intermediate-*n* modes become very unstable in some cases.

a. Infernal mode in tokamaks

The ballooning mode theory including finite-*n* correction was developed using the WKB formalism by Dewar *et al.*

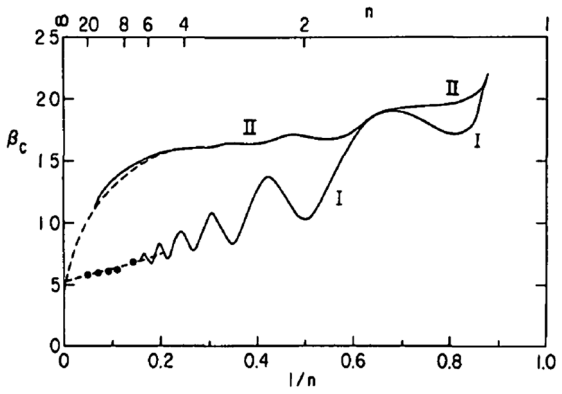

FIG. 42. n dependence of the beta limit showing agreement between WKB theory (dashed line) and PEST (solid line) in high-n regime and unique oscillatory behavior at low to intermediate n obtained by treating n as a continuous variable. From Dewar *et al.*, 1981.

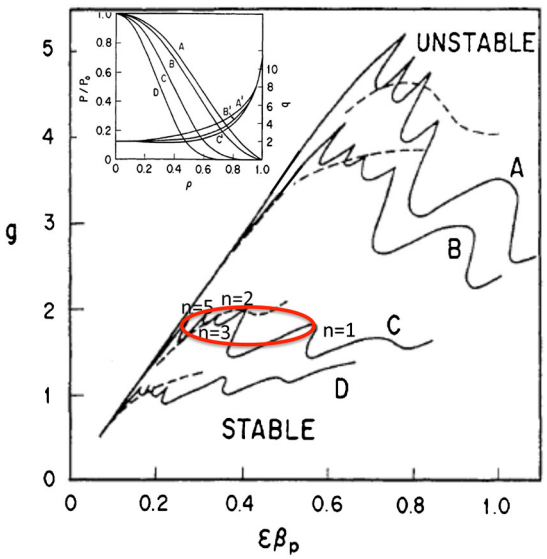

FIG. 43 (color online). Stability boundaries in $(\epsilon\beta_p, g)$ for various pressure profiles [A: $dp/d\psi \sim 0.3(1-\psi)^{0.5} + 0.7$, to C: $dp/d\psi \sim (1-\psi)^2$, D: $dp/d\psi \sim (1-\psi)^5$], where g is the normalized beta β_N. The circle shows the region of observed β_p collapses in high-β_p experiments in JT-60U. From Ozeki *et al.*, 1995.

(1979) and it agreed with the PEST calculation down to $n = 5$ as shown by Dewar *et al.* (1981). This theory predicts that the largest-n modes are most unstable within the ballooning formalism. But the PEST calculation also showed interesting oscillatory behavior of the beta limit in the intermediate-n regime as a function of $1/n$ if it is treated as a continuous variable (see Fig. 42).

Hastie *et al.* (1981) showed that this oscillatory behavior can be expected from the breakdown of the radial densely coupled ballooning mode structure. If the magnetic shear is finite, radial coupling of various resonant MHD modes (m, $m \pm 1$, $m \pm 2$, $m \pm 3$, etc.) becomes strong for high-n modes since the radial separation between modes is small. However, if the magnetic shear is very low, $s \sim 0$, the radial mode separation becomes larger and the standard ballooning mode theory by Connor *et al.* (1978) based on dense radial mode coupling breaks down.

Manickam *et al.* (1987) showed that when the magnetic shear is sufficiently weak, this oscillation can result in bands of unstable n values, where the ballooning mode theory predicts complete stability. This mode is called the "infernal" mode.

b. Infernal mode as cause of β_p collapse

Improved core confinement regimes at TFTR (Hawryluk *et al.*, 1998) and JT-60U (Kishimoto *et al.*, 2005) are associated with fast internal disruption or major disruption, where the beta limit deviates from Troyon scaling and is limited by $\epsilon\beta_p$ (McGuire *et al.*, 1988). This is called β_p collapse (Ishida *et al.*, 1992).

Figure 43 shows the stability diagram in $(\epsilon\beta_p, \beta_N)$ for various pressure profiles (A–D) in a WS plasma (magnetic shear ~0 in the central region) without wall stabilization and slightly high internal inductance $l_i = 1.2$ with $q_s/q_0 = 4$ (Ozeki *et al.*, 1995). Intensive central heating produces a peaked pressure profile and the observed β_p collapse is consistent with the region of $\epsilon\beta_p = 0.2$–0.6 for pressure profile C. The region of $\epsilon\beta_p = 0.2$–0.4 is characterized by low q_0 and intermediate $n = 2$–5 infernal modes become most unstable. While a broader pressure profile gives rise to much higher stable $\beta_N \sim 5$ ($l_i \sim 1.2$) without wall stabilization (Ozeki *et al.*, 1995), or $\beta_N \sim 5.8$ ($l_i \sim 1$) with a moderately distant wall $r_{\text{wall}}/a = 1.5$ (Howl *et al.*, 1992), the resultant broader bootstrap current seems not to be consistent with moderately high internal inductance for the steady-state tokamak operation.

Ozeki *et al.* (1993b) analyzed the ideal MHD stability of a circular weakly negative-shear (WNS) plasma $R/a = 3$, showing that significant improvement in the $\epsilon\beta_p$ limit can be obtained by modification of the pressure profile (see Fig. 44). Pressure profile B has a much higher $\epsilon\beta_p$ limit than that for pressure profile A. While the experimentally achievable $\epsilon\beta_p$ is ~0.6, tailoring of the pressure profile in the negative-shear regime and reduction of the pressure gradient near $q_{\min}$ improve stability against low $n = 1$–5 internal modes. Again, the importance of the relative location of the ITB and $q_{\min}$ radius is stressed. Bonderson *et al.* (1997) clarified characteristics of the NS stability regime with the high bootstrap current fraction without wall stabilization.

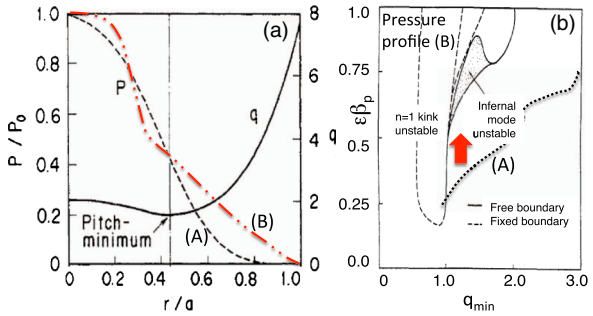

FIG. 44 (color online). (a) Pressure profiles (A) and (B) in weak-negative-shear plasma and (b) $\epsilon\beta_p$ stability improvement from (A) to (B) in $(q_{\min}, \epsilon\beta_p)$. From Ozeki *et al.*, 1993b.

Turnbull *et al.* (1998) addressed synergism between the cross section and profile shaping and sensitivity to wall location in beta optimization for NS.

Improved confinement regimes at NS plasma have been explored since their discovery by Strait *et al.* (1995) at DIII-D, by Levinton *et al.* (1995) at TFTR, and by Fujita *et al.* (1997b) at JT-60U as well as early experiments at JET (Hugon *et al.*, 1992). The NS plasma terminated mostly with the ideal $n = 1$ kink-ballooning mode and sometimes with the infernal mode near the ideal beta limit as discussed by Taylor *et al.* (1997) and Ishii *et al.* (1998). But it sometimes terminated with precursor oscillation possibly due to the Rutherford regime in the DTM as discussed in Sec. V.B.3. Turri *et al.* (2008) discussed the role of ideal (infernal) and resistive modes in electron-ITB discharges at TCV in detail.

2. Peeling, ballooning, and edge localized modes

The steady-state tokamak reactor will operate in the high-q (safety factor) and high-β_p (poloidal beta) regimes. Exploration of small or minute ELMs in this regime is crucial for the feasibility of divertor power handling. The high pressure gradient at ETB produces ELMs. The physics of ELMs has been well investigated since the *H* mode with ELM is a standard operation scenario for ITER.

The ballooning mode is a pressure-driven local ideal MHD mode with long wavelength along $\boldsymbol{B}$ and short wavelength perpendicular to $\boldsymbol{B}$ (Connor *et al.*, 1978). The peeling mode is an external mode localized near the plasma edge driven by the finite edge current (Manickam *et al.*, 1992). This mode can be coupled to the ballooning mode and is thought to be a cause of ELMs in tokamaks.

Since the growth rate of the medium-n peeling mode is rather low compared with the violent low-n kink instability, care must be taken to identify the stability boundary as discussed in Sec. V.A.2 and special codes have been developed such as MARG2D (Tokuda *et al.*, 1999; Aiba *et al.*, 2006) and ELITE (Wilson *et al.*, 2002). While the ELITE code was specifically developed for $n \geq 5$ using the $1/n$ expansion, the MARG2D code can analyze the stability boundary for any

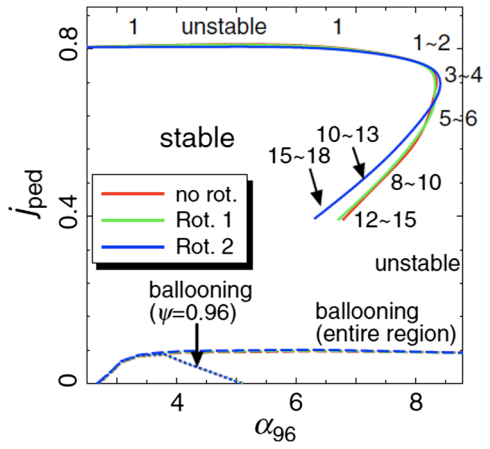

FIG. 45 (color online). Stability diagram of the high-q ($q_{95} = 7.3$) equilibria in the (j_{ped}, α_{96}) plane. Toroidal rotation weakly destabilizes the peeling-ballooning modes. From Aiba *et al.*, 2009.

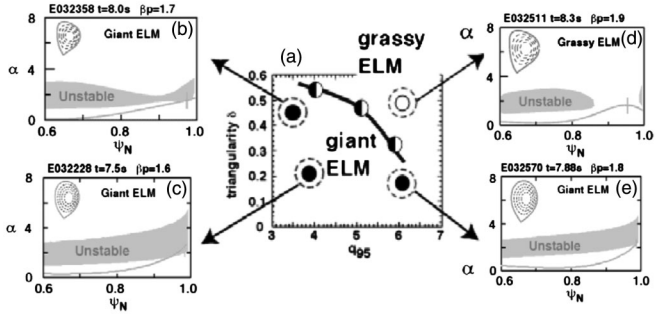

FIG. 46. The effect of triangularity and high-q operation for ELM stability. From Takeji *et al.*, 2002b.

toroidal mode number n efficiently, due to its special eigenvalue treatment. These codes have been applied to tokamak experiments by Snyder *et al.* (2002) and Hayashi *et al.* (2009), among others. The effect of a separatrix on edge MHD is an important subject and linear and nonlinear behaviors are addressed by the KINX code (Medvedev *et al.*, 2006) and the JOREK code (Huysmans *et al.*, 2007), respectively.

The stability of the peeling mode is well characterized by the pedestal current density j_{ped} and the normalized pressure gradient $\alpha = -2\mu_0 q^2 R(dP/dr)/B^2$. Figure 45 shows the stability of the ideal MHD modes ($n = 1, 2, 3, \ldots, 18$) for high-q ($q_{95} = 7.3$) operation in the (α, j_{ped}) diagram including the weak destabilizing effect of toroidal plasma rotation (Aiba *et al.*, 2009). Because of the low growth rate of the peeling-ballooning mode, the diamagnetic drift and finite-Larmor-radius effect become important as discussed by Azumi *et al.* (1981) and later by Tang *et al.* (1982). A key point is the replacement of $-\gamma^2$ with $\omega(\omega + \omega^*)$, which implies that $\gamma < \omega^*/2$ may be stabilized (Snyder *et al.*, 2002).

The stable region against ideal MHD modes in the high-q regime is much wider than in the low-q ($q_{95} \sim 3$) regime. The edge ballooning mode becomes stabilized with small $j_{ped} > 0.1$ in high-q operation, but not in low-q operation. Finite-n ($n = 3$–18) peeling-ballooning modes become most unstable when α reaches a critical value ($\alpha_c \sim 6$–8) for $j_{ped} \sim 0.4$–0.7. When the pedestal current density $j_{ped} > 0.8$, the plasma becomes unstable to the $n = 1$ mode. Excitation of a large edge bootstrap current in a collisionless edge plasma with $j_{ped} > 0.8$ will lead to $n = 1$ or a low-n global mode

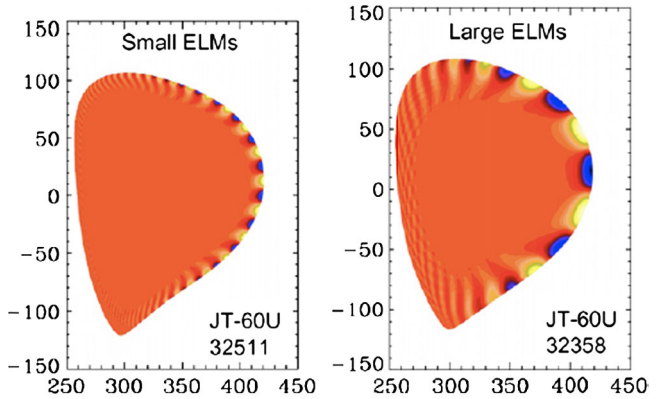

FIG. 47 (color online). Comparison of peeling-balooning eigenmodes for small and large ELMs. From Doyle *et al.*, 2007.

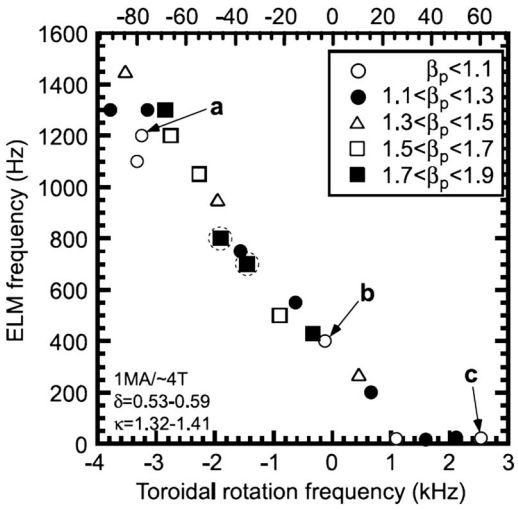

FIG. 48. ELM frequency variation with toroidal rotation at the pedestal top. From Oyama *et al.*, 2007.

(depending on the proximity of the stabilizing wall) and control of the edge bootstrap current to the stable region is important.

Kamada *et al.* (2000) and Lao *et al.* (2001) identified ELM regimes of type I and grassy ELM (or type-II ELM) by varying the plasma triangularity and safety factors and the results are shown in Fig. 46. The grassy ELM has been found at high $q_{95} = 6$ and high triangularity $\delta = 0.5$, which is relevant for steady-state tokamak reactors. Stability analysis by Lao *et al.* (2001) and Takeji *et al.* (2002b) showed the disappearance of type-I ELM at $q_{95} = 6$, high triangularity $\delta = 0.5$, and high $\beta_p = 1.9$, corresponding to entering into the second stability regime as shown in Fig. 46. It is also found that small and large ELMs correspond to small and larger radial extensions of eigenfunctions of peeling-ballooning modes, respectively, as shown in Fig. 47.

Significant modification of ELM characteristics by cotoroidal and countertoroidal rotation was reported by Oyama *et al.* (2007) as shown in Fig. 48. With more countertoroidal rotation, the discharges exhibit high-frequency grassy ELMs with comparable pedestal pressure to that in type-I ELMs. This observation is qualitatively consistent with the peeling mode stability including the effect of toroidal and poloidal rotations as shown by Aiba *et al.* (2011).

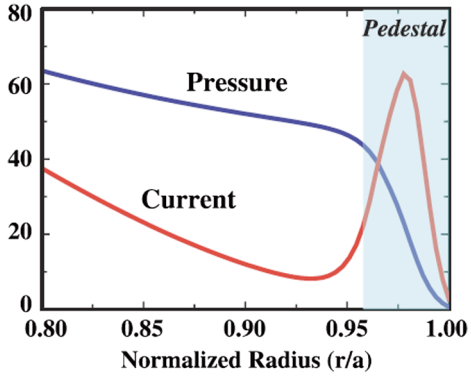

FIG. 49 (color online). Edge pedestal and edge bootstrap current in collisionless plasma. From Snyder *et al.*, 2009.

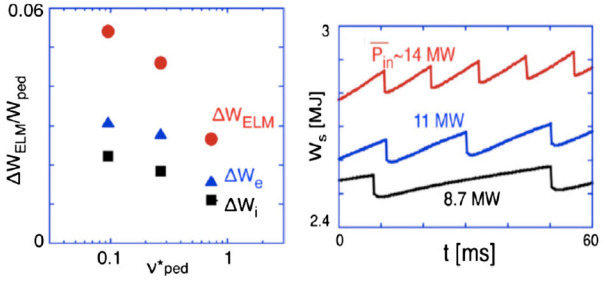

FIG. 50 (color online). ELM energy loss as a function of pedestal collisionality and time evolution of ELM for different powers. From Hayashi *et al.*, 2009.

The steep pressure gradient near the plasma edge drives the edge bootstrap current (pedestal current) if the edge plasma is collisionless enough as shown in Fig. 49 (Snyder *et al.*, 2009). This pedestal current destabilizes the peeling-ballooning mode. Experimentally, ELM energy loss increases with decreasing edge collisionality as shown by Loarte *et al.* (2003).

These characteristics are analyzed using a combination of MARG2D and a time-dependent 1.5D transport code (TOPICS-IB) by Hayashi *et al.* (2009). Reduction in edge collisionality lowers the edge magnetic shear by excitation of the bootstrap current. This reduction of magnetic shear enlarges the radial extent of the peeling eigenfunction leading to a larger energy loss by the ELM (see Fig. 50).

Since this ELM heat flux may become a serious problem and shorten the divertor lifetime of ITER (Hawryluk *et al.*, 2009), mitigation of ELMs becomes an important issue for the reliable operation of ITER. Evans *et al.* (2005) reported successful mitigation of type-I ELM in an ITER-like discharge with reduced pressure gradient by the RMP technique as shown in

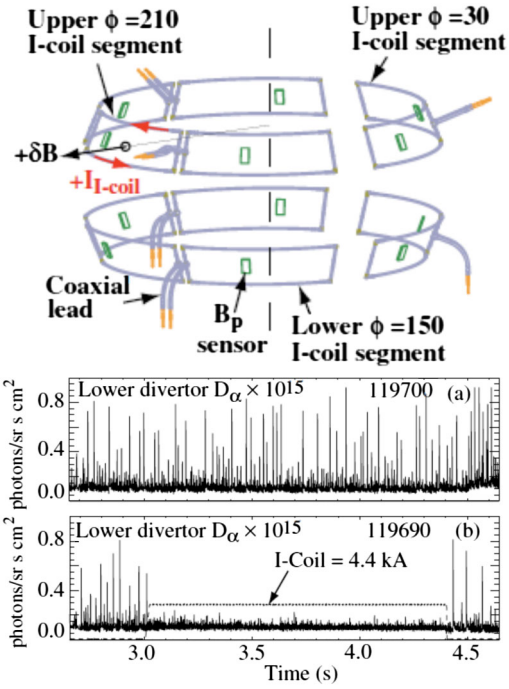

FIG. 51 (color online). Suppression of type-I ELM by $n = 3$ RMP. From Evans *et al.*, 2005.

Fig. 51. Snyder *et al.* (2007) explained this suppression of type-I ELM as due to lowering of the pressure gradient below the peeling-ballooning limit through field line stochastization. While Evans *et al.* (2005) used $n = 3$ magnetic perturbation, Liang *et al.* (2007) and Suttrop *et al.* (2011) stabilize ELMs by using $n = 1$ and $n = 2$, respectively.

3. Barrier localized mode

The BLM is an ideal MHD instability driven by the large local pressure gradient at the ITB, in both WS (Koide *et al.*, 1994; Takeji *et al.*, 1997) and NS (Manickam *et al.*, 1999) plasmas, and leads to relaxation of ITB without major disruption.

Figure 52 shows the time evolution of high-performance WS discharges at JT-60U (Koide *et al.*, 1994). After the formation of an ITB, the BLM became unstable and the ITB relaxation led to the formation of an H-mode edge. This BLM is estimated as $m/n = 3/1$ associated with a steep ITB near the $q = 3$ surface. If the ITB is recoverable after the BLM, a quasi-steady-state ITB is possible but the ITB may terminate as shown by Koide *et al.* (1996). Concerning the appearance of the $m/n = 3/1$ mode, Takeji *et al.* (1997) showed that the $n = 1$ mode is most unstable under the situation in which the bootstrap current driven by the steep pressure gradient reduces the local magnetic shear ($s \sim 0$), while the $n = 2$ mode is most unstable if the local shear is not weak. While intermediate-n peeling modes are responsible for the ELM, $n = 1$ or $n = 2$ semiglobal modes are responsible for the BLM.

The BLM in the NS plasma was analyzed by Manickam *et al.* (1999) for both JT-60U and TFTR. The JT-60U achieved a wider ITB radius; a steeper ITB was formed for balanced or perpendicular neutral beam injection and more frequently observed at JT-60U than other tokamaks such as TFTR. The softening of the BLM and the long-sustained quasi-steady-state improved confinement with ITB requires further investigation.

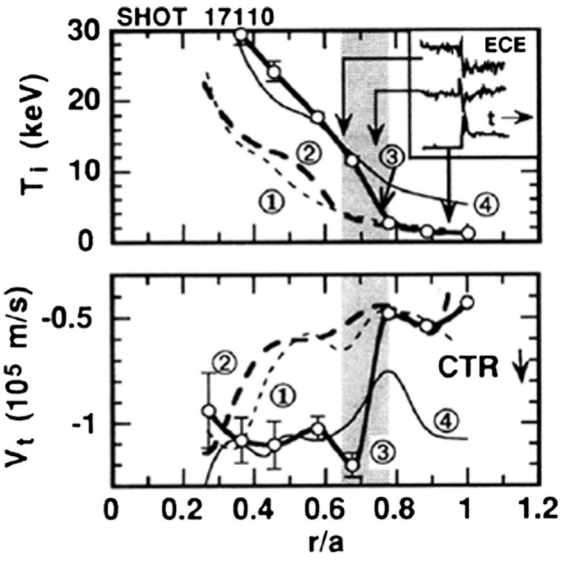

FIG. 52. Time evolution of high-β_p discharge showing the formation of ITB and subsequent BLM (observed by ECE) leading to H-mode edge pedestal formation. (1)–(4) correspond to different times between 5.6 and 6 s. From Koide *et al.*, 1994.

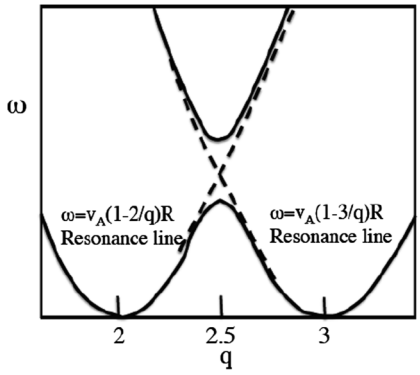

FIG. 53. SAR and gap structure due to toroidal coupling of $m = 1$ and $m = 2$ modes in the (q, ω) plane.

D. Alfvén eigenmodes

1. Shear Alfvén gap

In toroidal geometry where in-out inhomogeneity $B \sim B_0/(1 + \epsilon\cos\theta)$ exists, the SAR condition is given by a coupling of the $m[k_{\|m} = (n - m/q)/R]$ and $m + 1\{k_{\|m+1} = [n - (m + 1)/q]/R\}$ modes with mode coupling constant ϵ

$$\begin{vmatrix} k_{\|m}^2 - \frac{\omega^2}{v_A^2} & -\epsilon\frac{\omega^2}{v_A^2} \\ -\epsilon\frac{\omega^2}{v_A^2} & k_{\|m+1}^2 - \frac{\omega^2}{v_A^2} \end{vmatrix} = 0. \tag{117}$$

This gives a forbidden band of ω for the SAR (see Fig. 53), since $\sin(m\theta) + \sin[(m + 1)\theta] = \sin[(m + 0.5)\theta]\cos(0.5\theta)$, which implies periodicity after two circulations similar to the Mobius band. In this situation, it is difficult to have Alfvén resonance, which provides an explanation for the gap in the SAR.

Cheng *et al.* (1986) found this breakup of the continuous spectrum in the toroidal geometry by solving Eq. (88) through its conversion to a variational principle and application of the Galerkin method (see Fig. 54). The most important finding by Cheng *et al.* (1986) is the existence of a point (or discrete) spectrum in this gap with a frequency $\omega = k_{\|m}v_A = -k_{\|m+1}v_A = v_A/2qR$ at $r = r_m$, where $q(r_m) = (m + 1/2)/n$. Near $q(r_m)$, the eigenmode in $y = O(\epsilon^{0.5})$ can be expressed

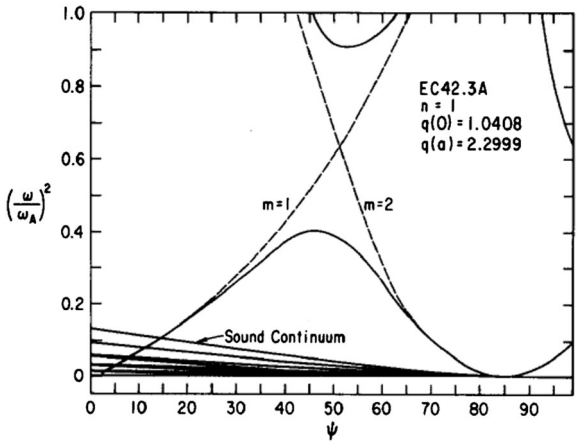

FIG. 54. Shear Alfvén resonance and gap spectrum due to toroidal coupling of $m = 1$ and $m = 2$ modes. From Cheng *et al.*, 1986.

as $u_m = a_1(\ln|y| + b_1)$, $u_{m+1} = a_2(\ln|y| + b_2)$, where $y = s(r - r_m)/r_m$ and $s = r_m(dq/dr)/q(r_m)$. While the AE with the SAR is singular at resonance, the AE in the gap is regular and radially extended. This AE due to toroidal mode coupling is called a toroidal Alfvén eigenmode (TAE). Since this mode does not experience continuum damping by the SAR, it can be destabilized through the wave-particle interaction.

An Alfvén resonance gap is also possible through other coupling mechanisms such as elongation of the plasma shape or more shaping; these modes are called elliptic Alfvén eigenmodes (EAEs) (Betti *et al.*, 1991) and noncircular Alfvén eigenmodes (NAEs) (Betti *et al.*, 1992), respectively. Elimination of the Alfvén resonance is also possible for a frequency ω slightly lower than $\min(k_\parallel v_A)$ (shown in Fig. 39) in the plasma but a shear Alfvén cutoff (r_s) still exists in the plasma, and a shear Alfvén wave exists without strong damping; this is called a global Alfvén eigenmode (GAE) (Appert *et al.*, 1982). This GAE has been observed by Evans *et al.* (1984). Sound (acoustic) wave resonance can also have a gap through a coupling with the low-frequency Alfvén continuum; this is called a beta-induced Alfvén acoustic eigenmode (Gorelenkov *et al.*, 2007).

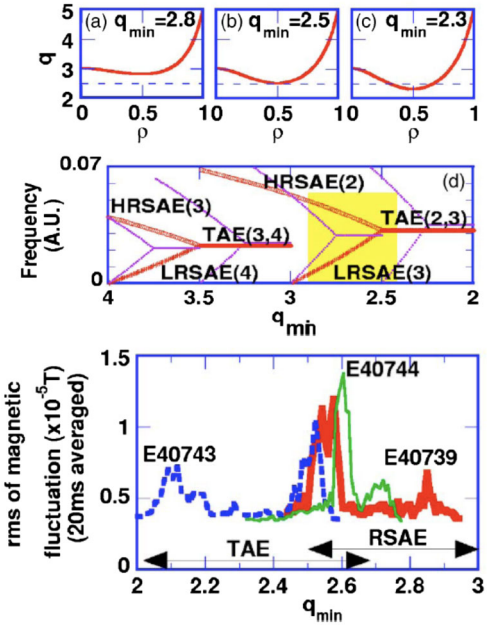

FIG. 55 (color online). Amplification of AE amplitude by RSAE-TAE interaction and the RSAE-TAE diagram. From Takechi *et al.*, 2005.

2. Stability of Alfvén eigenmodes

Cheng *et al.* (1985) showed that this TAE may be destabilized when the magnetic drift frequency of the energetic particles roughly equals the eigenfrequency of the TAE. Since energetic particles such as fusion-created α particles have comparable speed with the Alfvén velocities in ITER and DEMO, this has been an important subject since the 1990s. TAEs were first observed in a neutral-beam-heated plasma at TFTR by Wong *et al.* (1991).

The instability drive of these AEs is the pressure gradient of fast particles, $d\beta_{\rm fast}/dr$. There are several damping mechanisms, such as electron Landau damping (Fu *et al.*, 1989), ion Landau damping (Betti *et al.*, 1992), collisional damping of trapped electrons (Fu *et al.*, 1992), continuum damping (Berk *et al.*, 1992; Zonca *et al.*, 1992), and radiative damping (Mett *et al.*, 1992). The damping rate was directly measured by Fasoli *et al.* (1995). Both EAEs and NAEs were observed by Kramer *et al.* (1998) at JT-60U. The balance between the instability drive and damping gives the threshold $d\beta_{\rm fast}/dr$, discussed for burning plasma experiments by Gorelenkov *et al.* (2003). There are interim reviews of AEs by Wong *et al.* (1999), Chen *et al.* (2007), and Heidbrink *et al.* (2008).

Not only α particles but also MeV-class N-NBI fast ions can drive AEs, and the beam deposition profile should be carefully considered for steady-state operation. And as a result Ozeki's off-axis injection scenario is favorable for reduction of the central $d\beta_{\rm fast}/dr$. Actually tilting of N-NBI is thought to avoid TAEs at ITER (Polevoi *et al.*, 2010).

In the WNS operation, the TAE is more stable than in the case of positive-shear plasmas. In particular, the TAE becomes stable when a density ITB is formed inside $q_{\rm min}$ (Kimura *et al.*, 1998). This is because the TAE gap frequency $\omega \sim 1/n_e(r)^{0.5}q(r)^2$ becomes lower in the central region, prohibiting the formation of the TAE gap there. Thus the presence of a density ITB for tokamak steady-state operation seems good for AE stability.

On the other hand, the NS operation produces a new type of AE, observed as the chirping mode (Kusama *et al.*, 1998) when the density ITB is not strong enough for TAE formation. This is called the reversed shear Alfvén eigenmode (RSAE) and was explained as a special case of the GAE mode by Fukuyama *et al.* (1997). Berk *et al.* (2001) developed a theory of the RSAE. Nazikian *et al.* (2003) also demonstrated an α-particle-driven AE in a TFTR WNS plasma (Nazikian *et al.*, 1997) is RSAE.

Takechi *et al.* (2005) studied further the time evolution and structure of RSAEs. As $q_{\rm min}$ decreases in the range of $(m+1/2+\epsilon)/n < q_{\rm min} < (m+1)/n$, there are two RSAEs, the higher-frequency RSAEs (HRSAE) and the lower-frequency RSAEs (LRSAE) whose frequencies are given by $f_{\rm HRSAE} \sim (n - m/q_{\rm min})v_A/2\pi R$ and $f_{\rm LRSAE} \sim [(m+1)/q_{\rm min} - n]v_A/2\pi R$. When $q_{\rm min}$ decreases further in the range of $m/n < q_{\rm min} < (m+1/2+\epsilon)/n$, the TAE gap is formed and the TAE frequency is given by $f_{\rm TAE} \sim v_A/4\pi q_{\rm TAE}R$, where $q_{\rm TAE} = (m-1/2)/n$. Figure 55 shows a schematic diagram of AE evolution. It is important to note that the AE amplitude becomes bigger during the transition from the RSAE to the TAE mode. The RSAE mode is used to determine $q_{\rm min}$ (Sharapov *et al.*, 2001).

A unique $n = 0$ chirping mode was observed in the JET ion cyclotron resonance frequency experiment, where an energetically inverted ion distribution function was formed in the high-field side. Berk *et al.* (2006) explained it as a global geodesic acoustic mode.

3. Nonlinear Alfvén eigenmodes

Interaction of AEs with energetic particles produces radial transport or loss of fast ions (Duong *et al.*, 1993), damage to the first wall (White *et al.*, 1995), and reduction of the fusion

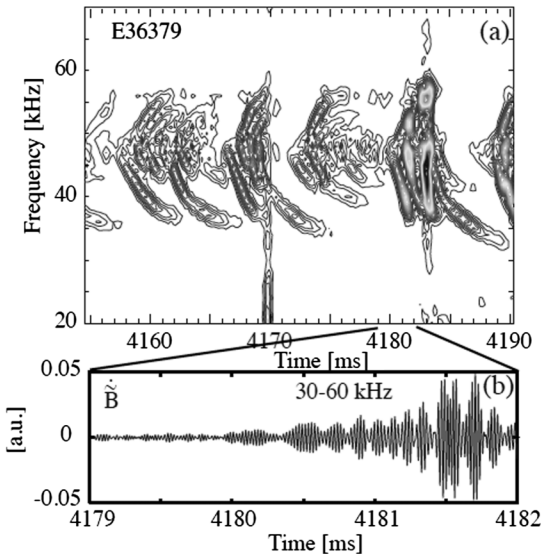

FIG. 56. Fast frequency sweeping (FS) mode observed at JT-60U. From Shinohara *et al.*, 2001.

reaction (Shinohara *et al.*, 2001; Ishikawa *et al.*, 2007). These processes may become strongly nonlinear. There are typically four nonlinear behaviors: (1) saturation, (2) limit cycle oscillation, (3) formation of a chaotic nonlinear state, and (4) explosive growth with mode frequency sweeping. Type 4 was observed by Shinohara *et al.* (2001); see Fig. 56.

The so-called Berk-Breizman (BB) model provides a clear view of the nonlinear behavior of AEs, which naturally explains type -4 instability (Berk *et al.*, 1999). Berk *et al.* (1995) gave a simplified Lagrangian formalism for wave-particle interaction. The Lagrangian for charged particles in an electromagnetic (EM) field is given by $L = L_w + L_{\mathrm{EP}}$, where L_w and L_{EP} are the Lagrangians for plasma particles and energetic particles, respectively. Each Lagrangian is a summation of free-particle, field-particle, and field Lagrangians. A simplified Lagrangian is obtained by assuming an adiabatic response for the background plasma. L_w is approximated by the quadratic form of the wave amplitude and its contribution can be regarded as a part of the electric field $\tilde{E}$.

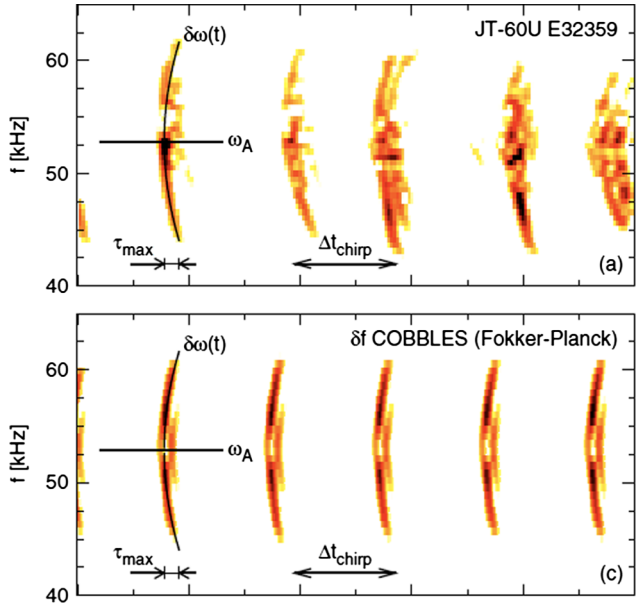

FIG. 57 (color online). Comparison of fast FS mode in JT-60U and simulation using the BB model. From Lesur *et al.*, 2010.

The nonlinear behavior of AEs is determined by a competition among drive by resonant particles, external damping, particle relaxation to recover positive df/dv, and particle trapping to smooth it. Chirping solutions occur in the rare collision regime when a hole and clump structure is formed in phase space (Berk *et al.*, 1999). Lesur *et al.* (2009) developed a code to solve the corresponding full-f and delta-f Vlasov equations numerically and explained the frequency sweeping (FS) as shown in Fig. 57. This shows the effectiveness of the BB model and also the importance of collisional drag and diffusion in velocity space (Lilley *et al.*, 2009; Lesur *et al.*, 2010).

E. Stability of the current hole

The CH is an interesting structure formation in the tokamak magnetic configuration, which is robust against perturbation. We briefly describe its equilibrium, ideal, and resistive MHD stabilities.

1. Equilibrium bifurcation

Takizuka (2002) described the dynamics of equilibrium bifurcation to a CH. CH operation is created by strong heating during the current ramp, leading to the buildup of a large bootstrap current (Fujita *et al.*, 2001) or noninductive CD (Hawkes *et al.*, 2001) associated with a negative Ohmic current with negative E_ζ. This negative E_ζ penetrates to the plasma center, and the central J_ζ becomes very low but cannot be negative due to the loss of equilibrium with the nested flux surface. However, an axisymmetric multimagnetic island (AMMI) equilibrium with the slightly negative J_ζ can exist in CH operation (see Fig. 58).

A number of investigations of AMMI equilibrium have been published since then, such as those by Martynov *et al.* (2003), Wang *et al.* (2004), and Rodrigues *et al.* (2005). Rodrigues *et al.* (2007), in particular, gave a theoretical calculation showing excellent agreement with the JT-60U result.

2. Resistive stability and the β limit

One of the important CH characteristics is a current clamp to $J_\zeta \sim 0$ (Fujita *et al.*, 2005). Huysmans *et al.* (2001)

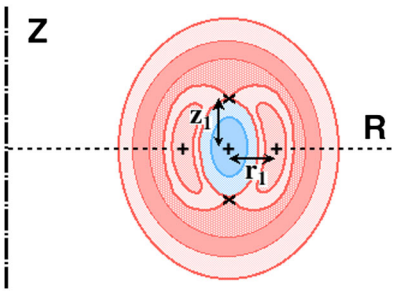

FIG. 58 (color online). Axisymmetric trimagnetic island equilibrium. From Takizuka, 2002.

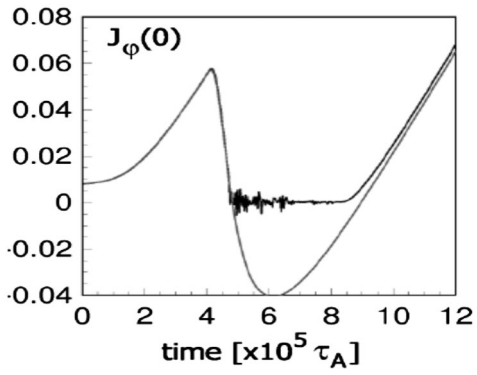

FIG. 59. Time evolution of central current density with and without resistive $m/n = 1/0$ modes. From Huysmans *et al.*, 2001.

calculated the time-dependent current diffusion using the reduced MHD equation. It was found that the central current density is clamped to nearly zero because of the $n = 0$ low-m resistive instabilities when negative current density is expected, without taking into account any of these modes, as shown in Fig. 59. The growth rate is largest for $m = 1$ and scales as $\gamma \sim \eta^{1/3}$ (as for the internal kink mode), while $\gamma \sim \eta^{3/5}$ for the $m = 2$ mode (as for the TM).

While there is no confinement inside the CH, it is possible to sustain high plasma pressure via dP/dr outside the CH. In fact, it was found that the stability limit is not very different between the strong-reversed-shear case with $q(0)/q_{\min} = 20$ [the model equilibrium for the CH since there is no equilibrium solution for $q(0) = \infty$] and the moderate-reversed-shear case with $q(0)/q_{\min} = 2$ (Ozeki *et al.*, 2003a). The standard ideal MHD stability calculation for the CH by Ozeki *et al.* (2003b) showed that the beta limit could be $\beta_N \sim 5$.

Chu *et al.* (2004) showed using the ideal MHD potential energy that the plasma behaves as if it were bordered by an extra internal vacuum region.

F. Magnetohydrodynamics summary

The control of ideal, resistive, and kinetic MHD is an essential element of fusion research. For three types of advanced tokamak operation (WS, NS, and CH) to realize efficient steady-state operation, ideal MHD modes such as peeling and ballooning modes for edge plasma, infernal modes for core plasma and BLMs for ITB, resistive MHD modes such as NTMs, DTMs, and RWMs, and kinetic MHD modes such as TAEs and RSAEs are well understood, including the control knob, while some kinetic MHD modes are not yet completely understood. The key issue is that the plasma profile does not match the optimum profile for high-beta advanced tokamak operation since the profile is determined by the turbulent transport. Hence, the understanding of turbulent transport is essential for optimization of the operation steady-state tokamaks.

VI. PERPENDICULAR TRANSPORT IN TOKAMAKS

The MHD stability physics of advanced tokamaks described above tells us that the plasma pressure profile must be controlled to avoid MHD modes and hence to realize a SSTR. Control of the temperature and density profiles requires a basic understanding of transport processes across the flux surface and identification of key parameters.

Energy and particle transport across a magnetic surface is governed by microinstabilities (Tang *et al.*, 1978). Drift waves (Horton *et al.*, 1999; Yoshizawa *et al.*, 2001) are the most likely candidates for turbulent transport in tokamaks and flow shear (Terry *et al.*, 2000) is the key to reduction of turbulent transport. The zonal flow (Diamond *et al.*, 2005; Fujisawa, 2009) plays an essential role in realizing fusion burn at ITER (Lin *et al.*, 1998). We now review recent progress.

A. Turbulent transport

1. Self-organized criticality

Heat and particle transport in tokamaks is governed by turbulent transport. Stiffness of the temperature profile is observed in the L mode, which is closely related to the existence of a critical temperature gradient in the toroidal ITG, TEM, and electron temperature gradient (ETG) modes, and turbulent heat transport is produced by avalanches, analogous to sand avalanches in a sand pile as discussed by Bak *et al.* (1987) as a typical example of self-organized criticality (SOC).

Diamond *et al.* (1995) clarified the dynamics of the turbulent plasma transport near marginal stability. If the initial dT_0/dr profile (shown by the dotted line in Fig. 60) is close to the critical temperature gradient $dT/dr|_c$, the superposition of a void ($\delta T < 0$) causes strong destabilization of the critical temperature gradient and the instabilities in the inner front lead to the inward propagation of the void. If a bump ($\delta T > 0$) is superposed, dT/dr in the outer front becomes larger, leading to an outward propagation of the bump. Diamond *et al.* noted that the heat flux q must be invariant under the dual transformations $x \rightarrow -x$ and $\delta T \rightarrow -\delta T$; this was called "joint reflection symmetry" by Hwa *et al.* (1992). This symmetry leads to a symmetric probability distribution of the void and bump.

Garbet *et al.* (1998) clarified the importance of heat-flux-driven simulation for SOC, showing the existence of an avalanche, while Candy *et al.* (2003) indicated the avalanche in a gyrokinetic fixed profile simulation. A gyrokinetic full-f Vlasov simulation of heat-flux-driven toroidal ITG turbulence by Idomura *et al.* (2009) clarified an important feature of self-organized criticality.

While sand collapses in a sand pile exhibiting equal probabilities of bump and void propagation, the relative

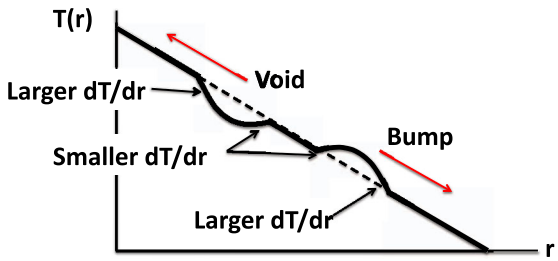

FIG. 60 (color online). Bump and void avalanches near marginal stability.

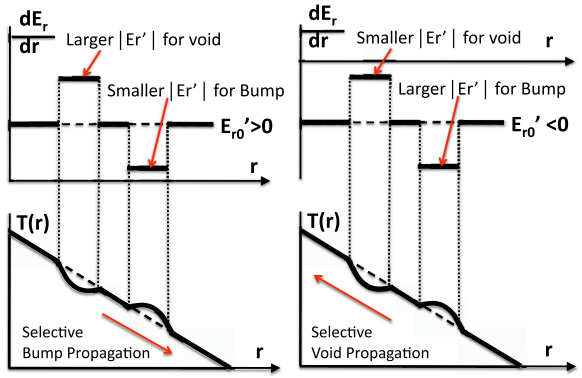

FIG. 61 (color online). Symmetry breaking of void and bump avalanches by dE_r shear.

occurrence of bump and void propagation varies in plasma turbulence through the change in dE_r/dr. The zeroth-order force balance equation (74) using the neoclassical expression for residual poloidal flow is shown to be still valid on average even under plasma turbulence (Idomura *et al.*, 2009), and is

$$u_{\zeta i} = \frac{1}{B_\theta}\left[E_r - \frac{1}{eZ_i n_i}\frac{dP_i}{dr} - \frac{K_1}{eZ_i}\frac{dT_i}{dr}\right] \tag{118}$$

in the cylindrical approximation, where K_1 is given by Eq. (64). This radial force balance means that E_r will balance the other two terms on the right-hand side as long as there is no toroidal rotation drive ($u_{\zeta i}$ is determined by the toroidal momentum balance equation). Therefore, an important additional constraint for plasma turbulence is that E_r shear should build up in proportion to temperature curvature during void or bump formation, namely, $dE_r/dr \sim cd^2T_i/dr^2$, where $c > 0$ is constant.

The void has positive temperature curvature ($d^2T_i/dr^2 > 0$) and the bump has negative temperature curvature ($d^2T_i/dr^2 < 0$), so that the E_r shear structures with voids and bumps for the cases of positive and negative background dE_{r0}/dr become as shown schematically in Fig. 61. Selective avalanche occurs in cases where $|dE_r/dr|$ is weakened by voids and bumps.

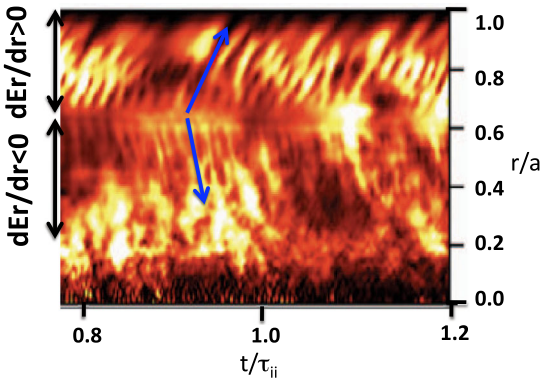

FIG. 62 (color online). Gyrokinetic full-f simulation of toroidal ITG turbulence, showing outward propagation of the bump where $dE_r/dr > 0$ and inward propagation of void where $dE_r/dr < 0$. From Idomura *et al.*, 2009.

In Fig. 62, two kinds of heat flux propagation are identified; one is an outward-propagating bump and the other is an inward-propagating void. When there is no E_r shear, outgoing bumps and incoming voids occur equally and cross each other during their radial propagation, which is a manifestation of joint reflection symmetry. But this symmetry breaks down when there is a gradient dE_r/dr in the plasma as described above, and selective avalanches occur. Even in a linear device, an avalanche or streamer (state of bunching of drift waves) is formed through nonlinear phase locking of the major triplet modes as shown by Yamada *et al.* (2008).

2. Ion temperature gradient turbulence

While earlier experimental work by Artsimovich (1972) and Murakami *et al.* (1979) indicated that ion thermal transport is close to neoclassical, anomalous ion thermal transport has been observed in DIII by Groebner *et al.* (1986) and was followed by large tokamak experiments like the TFTR supershot by Zarnstorff *et al.* (1989). Recent JET experiments by Mantica *et al.* (2009, 2011) showed clear evidence of a critical temperature gradient in ion transport (see Fig. 63).

a. Critical dT_i/dr and linear mode structure

The ITG is a drift wave rotating in the ion diamagnetic direction and is a primary candidate for anomalous ion thermal conduction and SOC, with its critical temperature gradient dT_{ic}/dr for destabilization. Romanelli *et al.* (1989) solved the ion-drift kinetic equation using a ballooning transformation and derived an approximate expression for dT_{ic}/dr in terms of $L_{T_i} = T_i/(dT_{ic}/dr)$ in the flat density regime: $R/L_n < 2(1 + T_i/T_e)$ $[L_n = n/(dn/dr)]$ in a circular plasma. They also showed that the dT_i/dr observed by Groebner *et al.* (1986) is close to the theoretical dT_{ic}/dr given by $R/L_{T_i} = \frac{4}{3}(1 + T_i/T_e)$. Guo *et al.* (1993) proposed a combined formula including the Hahm *et al.* (1989) slab ITG threshold, which does not quite reproduce the numerical slab ITG threshold. A more refined formula for the critical temperature gradient can be obtained by just adding two terms including the impurity effect implied by the ETG formula (128) as

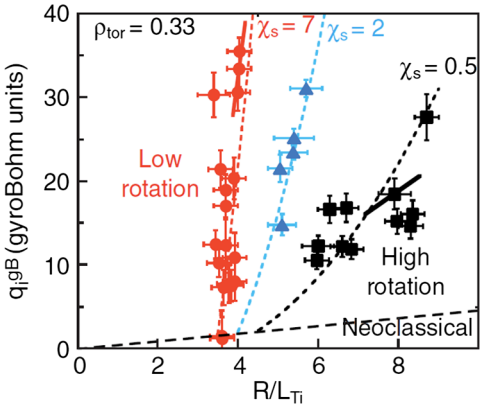

FIG. 63 (color online). Normalized ion heat flux as a function of R/L_{Ti} for different toroidal rotations at JET. From Mantica *et al.*, 2011.

$$R/L_{T_i} = (1 + \tau_i)(1.33 + 1.91s/q), \tag{119}$$

where $\tau_i = T_i/T_e Z_{\text{eff}}$, and s and q are the magnetic shear and safety factor, respectively.

Romanelli *et al.* (1993) further analyzed the radial structure of toroidal ITG showing that the ITG has a radially elongated structure with a characteristic radial correlation length $L_r \sim (\rho_i L)^{1/2}$ due to toroidal coupling. So toroidicity significantly influences the linear mode structure of the ITG. Such a radially elongated semiglobal structure tilted in the poloidal direction was also reported in the gyrokinetic simulation by Parker *et al.* (1993). Kishimoto *et al.* (1996) discussed this semiglobal structure of toroidal ITG related to SOC. In order to treat accurate eigenmodes efficiently in toroidal ITG modes, Idomura and co-workers developed a quasiballooning representation for ITG turbulence (Idomura *et al.*, 2003) originally developed for the linear MHD solver by Gruber *et al.* (1981). Figure 64 shows a typical example of a recent gyrokinetic simulation by Idomura *et al.* (2003).

In an axisymmetric system, the electrostatic potential $\tilde{\Phi}$ can be expressed as a summation of poloidal harmonics with harmonic amplitude $\tilde{\Phi}_l(q)$ constructed by the eigenfunction for $l = 0$, $\tilde{\Phi}_0(nq - m)$ peaked at $q = m/n$, and assuming a translational symmetry similar to the Bloch function in a crystal lattice (Kittel, 1971; Zakharov *et al.*, 1979),

$$\tilde{\Phi}(r, \theta, \zeta) = \sum_{l=-\infty}^{+\infty} \tilde{\Phi}_l(q) e^{i(m+l)\theta} e^{-in\zeta}, \tag{120}$$

$$\tilde{\Phi}_l(q) = a(\Delta q)\tilde{\Phi}_0(nq - m - l), \tag{121}$$

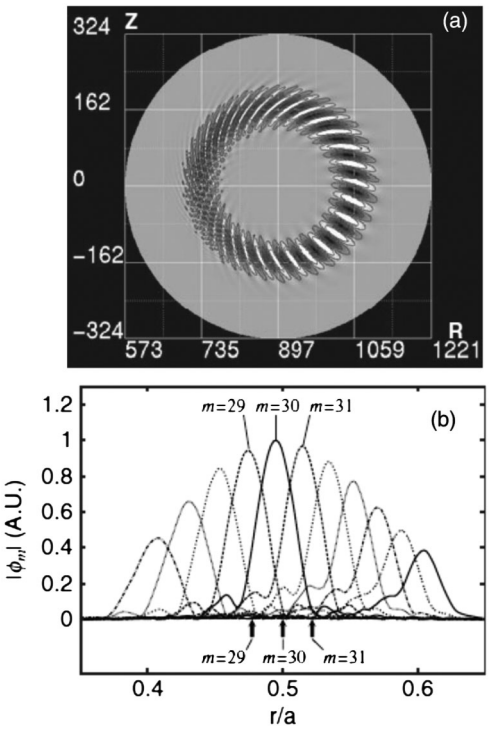

FIG. 64. (a) Eigenmode structure in poloidal cross section. (b) Radial harmonics of toroidal ITG with $n = 15$ and $a/\rho_i = 324$. From Idomura *et al.*, 2003.

where each harmonic is located in the region with $q = (m + l)/n$. Here q is the safety factor used as a radial coordinate, $\Delta q = l/n$, $a(\Delta q)$ is the slowly varying amplitude corresponding to the envelope of modes in Fig. 64. This is called the ballooning eigenfunction, originally developed for the ideal MHD ballooning mode. This translational symmetry holds except at the mode edge. This translational symmetry comes from the dense overlap of poloidal harmonics and breaks down when magnetic shear is very weak, as in the infernal mode discussed in Sec. V.C.1.

b. Zonal flow in toroidal ion temperature gradient turbulence

Zonal flow is $\boldsymbol{E} \times \boldsymbol{B}$ flow with toroidally ($n = 0$) and poloidally ($m = 0$) symmetric but radially varying electric potential fluctuation with nearly zero frequency and is important in regulating turbulence (Lin *et al.*, 1998). Extensive reviews of theories and experiments have been given by Diamond *et al.* (2005) and Fujisawa (2009), respectively. Zonal flow in drift wave turbulence was first predicted by Hasegawa *et al.* (1979) from the energy cascade of the Hasegawa-Mima equation (Hasegawa *et al.*, 1977) and its similarity to the geostrophic vortex equation (Charney eqation) of the Jobian atmosphere, and was confirmed by numerical simulation of the Hasegawa-Mima equation with dissipation (Hasegawa-Wakatani equation) in the cylindrical geometry (Hasegawa *et al.*, 1987). Zonal flow does not produce radial transport due to its symmetry and more importantly can stabilize plasma turbulence via the $\boldsymbol{E} \times \boldsymbol{B}$ flow shear.

Chen *et al.* (2000) clarified the dynamics of zonal flow generation by use of the modulational instability in toroidal ITG turbulence. Four waves (pump wave, zonal flow, and two sideband waves) affect this modulational instability. As described in Eq. (120), the toroidal ITG with a single n value consists of a set of poloidal harmonics oscillating together with a fixed phase relation. So the zonal flow, the pump wave, and the sidebands can be expressed as follows [$a(\Delta q) = 1$ is assumed by Chen *et al.* (2000)]:

$$\tilde{\Phi}^{\text{ZF}} = \tilde{\Phi}_0^{\text{ZF}}(x) e^{ik_r r - i\Omega t}, \tag{122}$$

$$\tilde{\Phi}^{p} = \sum_{m=-\infty}^{+\infty} \tilde{\Phi}_0^{p}(x) e^{i(m\theta - n\zeta - \omega_0 t)}, \tag{123}$$

$$\tilde{\Phi}^{\pm} = \sum_{m=-\infty}^{+\infty} \tilde{\Phi}_0^{\pm}(x) e^{i[m\theta \mp (n\zeta + \omega_0) + ik_r r - \Omega t]}. \tag{124}$$

Here $x = nq - m$. Sideband modes with (radial wave number, toroidal mode number, frequency) $= (+k_r, +n, \omega_0 + \Omega)$ and $(+k_r, -n, -\omega_0 + \Omega)$ interact to produce zonal flow $(+k_r, n = 0, \Omega)$.

In the toroidal geometry, Rosenbluth *et al.* (1998) showed that this zonal flow can have an undamped component due to the neoclassical effect, which is found to be an important mechanism in regulating the saturation level of turbulence and associated radial heat transport,

$$\frac{u_p}{u_p(0)} = \frac{1}{1 + 1.6q^2/\epsilon^{0.5}}. \tag{125}$$

The kinetic equilibrium of the tokamak may be characterized by a canonical Maxwellian distribution $f_{\rm CM}(P_\phi, \epsilon, \mu) = C_{\rm CM}(P_\phi)\exp[-\epsilon/T_a(P_\phi)]$, where P_ϕ, ϵ, and μ are the canonical angular momentum, kinetic energy, and magnetic moment, respectively. Use of this canonical Maxwellian is important in delta-f simulation to eliminate spurious growth of the zonal flow (Idomura *et al.*, 2003). The accurate kinetic equilibrium is the neoclassical equilibrium with self-consistent E_r (Idomura *et al.*, 2009).

The toroidal effect (especially at high q) sometimes inhibits this zero-frequency zonal flow (hereafter- called the zonal flow) and produces the so-called geodesic acoustic mode (GAM), which is an oscillating zonal flow through geodesic coupling to the $m = 1$, $n = 0$ pressure perturbation, first predicted by Winsor *et al.* (1968) and reconsidered by Hallatschek *et al.* (2001). Zonal GAM flow v_E is larger on the outside of the torus and smaller on the inside because $B \propto 1/R$. This leads to a density perturbation $\tilde{n}$ proportional to $-\nabla\cdot\boldsymbol{v}_\perp = (\boldsymbol{E}\times\boldsymbol{B})\cdot\nabla B^2/B^4$, which produces parallel pressure perturbation p. The coupled evolution equations for v_E (zonal GAM flow) and the perturbed pressure p in a toroidal plasma with circular cross section are (Miyato *et al.*, 2004)

$$\frac{\partial\langle v_E\rangle}{\partial t} = \frac{1}{r^2}\frac{\partial}{\partial r}r^2\langle\tilde{v}_{Er}\tilde{v}_{E\theta}\rangle + \frac{\mu_0\beta}{n_{\rm eq}}\frac{1}{r^2}\frac{\partial}{\partial r}r^2\langle\tilde{B}_r\tilde{B}_\theta\rangle - \frac{2}{n_{\rm eq}}\frac{a}{R}\langle p\sin\theta\rangle, \tag{126}$$

$$\frac{\partial}{\partial t}\langle p\sin\theta\rangle = -\langle[\tilde{\phi}, \tilde{p}]\sin\theta\rangle + (\Gamma+\tau)p_{\rm eq}\frac{a}{qR}\langle v\cos\theta\rangle + (\Gamma+\tau)\frac{a}{R}p_{\rm eq}\langle v_E\rangle. \tag{127}$$

Here $\langle\cdot\rangle$ is the flux surface average, $\langle v_E\rangle = \partial\phi_0/\partial r$ is the GAM flow, $\tilde{v}_{Er} = -(1/r)\partial\tilde{\phi}/\partial\theta$ and $\tilde{v}_{E\theta} = \partial\tilde{\phi}/\partial r$ are turbulent $E\times B$ drift velocities in the radial and poloidal directions, respectively, $\langle p\sin\theta\rangle$ is the $(m, n) = (1, 0)$ pressure perturbation, $n_{\rm eq}$ is the equilibrium density, β is the beta value, $[f, g]$ is the Poisson bracket, $\Gamma = 5/3$, $\tau = T_e/T_i$, and $p_{\rm eq}$ is the equilibrium pressure. The three terms on the right-hand side of Eq. (126) are the Reynolds stress, Maxwell stress, and the geodesic transfer term, respectively. The three terms on the right-hand side of Eq. (127) are the nonlinear coupling of pressure perturbation to turbulence, sound wave, and zonal flow terms, respectively. Scott (2003) showed that while turbulent Reynolds stress always transfers energy from small eddies to the larger-scale zonal flows, the geodesic curvature couples the zonal flows to finite-$k_\parallel$ pressure sidebands, by which the nonlinear $\boldsymbol{E}\times\boldsymbol{B}$ pressure advection $(\boldsymbol{v}_E\cdot\nabla\tilde{p}_e)$ quickly delivers the free energy in the zonal flow and sidebands back to the turbulence, and the growth of the zonal flow amplitude is limited. This is called the geodesic transfer effect.

A global electromagnetic Landau-fluid ITG simulation by Miyato *et al.* (2005) clarified the basic properties of the GAM. While strong zonal flow dominates in the low-q regime, zonal flow is weak and the GAM is dominant in the high-q regime [see Fig. 65(a)]. The zonal flow energy is supplied mainly by the Reynolds stress drive ($-\langle\tilde{v}_{Er}\nabla^2\tilde{\phi}\rangle\times\langle v_E\rangle$) at low β, and zonal flow energy is transferred to a (1,0) pressure perturbation through geodesic transfer for both zonal flow and GAM [see Fig. 65(b)]. The energy supply for $\langle p\sin\theta\rangle$ is from zonal and/or GAM flows and is transferred mainly to the sound wave term $\langle v\cos\theta\rangle$ in the case of zonal flow, while it is transferred mainly to turbulence through nonlinear coupling between electrostatic potential and pressure perturbation in the case of the GAM.

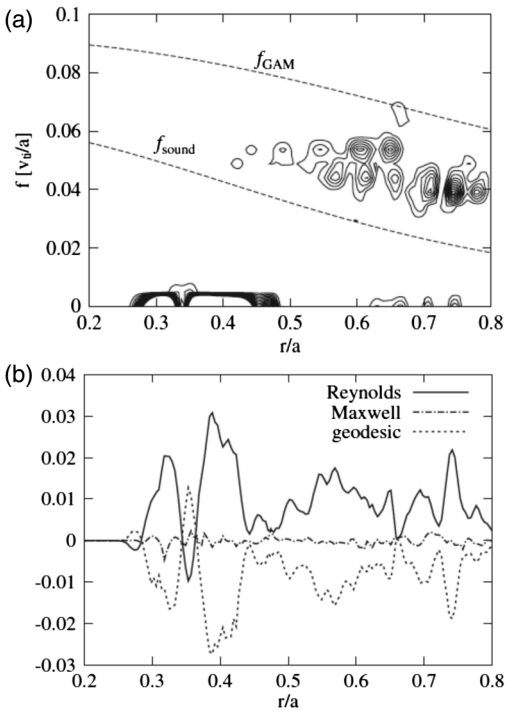

FIG. 65. (a) Radial variation of normalized zonal flow, GAM, and sound wave frequencies [$f[v_i/a]$, $f_{\rm GAM} = \sqrt{2(\Gamma+\tau)T_{\rm eq}}(a/2\pi R)$, and $f_{\rm sound} = \sqrt{(\Gamma+\tau)T_{\rm eq}}(a/2\pi qR)$]. (b) Radial variation of time-averaged zonal flow drives. From Miyato *et al.*, 2005.

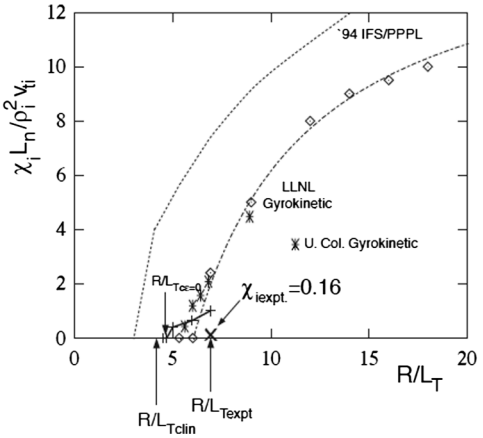

FIG. 66. Equivalent ion thermal diffusivity vs R/L_T from the Lawrence Livermore National Laboratory (LLNL) gyrokinetic simulation, showing the Dimits shift, as compared with the 1994 Institute of Fusion Study/Princeton Plasma Physics Laboratory (IFS/PPPL) gyrofluid simulation. From Dimits *et al.*, 2000.

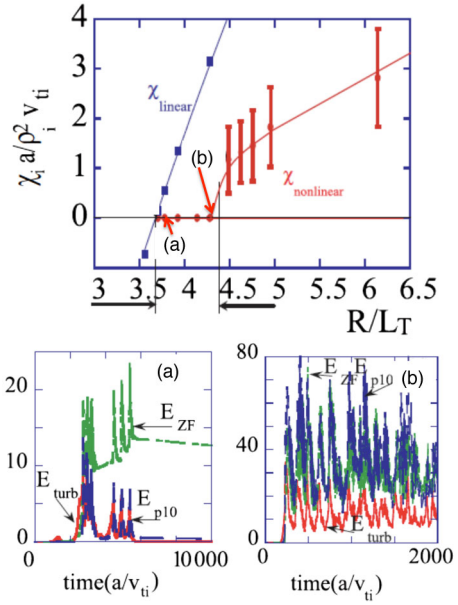

FIG. 67 (color online). Transient GAM–zonal-flow interplay in the Dimits shift regime $R/L_T = 3.83$ and above $R/L_T = 4.47$. From Miki *et al.*, 2007.

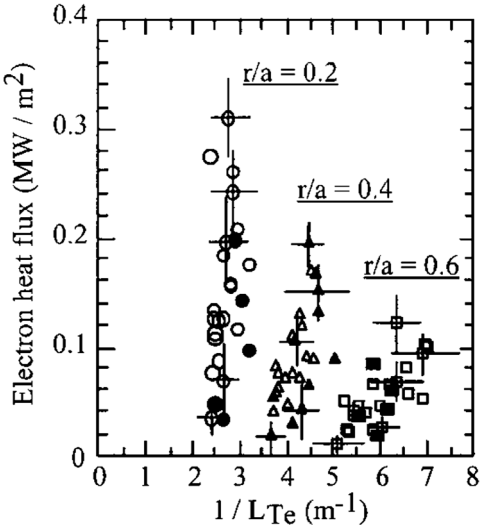

FIG. 68. Electron heat flux as a function of R/L_T showing the existence of critical electron temperature gradient. The open symbols correspond to $r/a = 0.2$, 0.4, and 0.6, respectively, and the full symbols correspond to another series of discharges. From Hoang *et al.*, 2001.

Direct numerical simulation of gyrokinetic ITG turbulence showed that, near the linear stability boundary, the ITG mode is completely stabilized. In the slightly unstable regime, the ITG grows initially but is quenched by the induced zonal flow. This zonal flow is strong enough to reduce ion thermal transport to the neoclassical level (Dimits *et al.*, 2000). The dynamics between zonal flow and turbulence upshifts the critical temperature gradient from that for linear stability, $R/L_{T\mathrm{clin}}$, to $R/L_{T\mathrm{clin}} + \Delta R/L_{Tc}$ as shown in Fig. 66, and $\Delta R/L_{Tc}$ is called the Dimits shift (Dimits *et al.*, 2000). In the Dimits shift regime ($R/L_{T\mathrm{clin}} < R/L_T < R/L_{T\mathrm{clin}} + \Delta R/L_{Tc}$), free energy from dT/dr is transferred mainly to zonal flow and not to ITG turbulence.

Miki *et al.* (2007) showed an interesting transient dynamical interplay between GAM and zonal flows in the Dimits shift regime and beyond by a Landau-fluid simulation with fixed profiles as shown in Fig. 67, which produces intermittent transport called GAM intermittency. In the Dimits shift regime, the zonal flow energy increases with time while the GAM and turbulence energies are reduced and quenched. On the other hand, GAM oscillation persists above the Dimits shift regime, giving quasisteady intermittent transport driven by the GAM. Ido *et al.* (2006) showed that the GAM-turbulence interaction can produce intermittent transport. Conway *et al.* (2011) showed that interplay between GAM and zonal flow is also important for the L- to H-mode transition. Plasma elongation has a stabilizing effect on the toroidal ITG mode both linearly and nonlinearly, and both the zonal flow and GAMs increase with elongation, which leads to a reduction of turbulent transport (Angelino *et al.*, 2008, 2009).

3. Electron temperature gradient turbulence

A significant departure of electron heat transport from neoclassical theory has been observed since the early experiments by Artsimovich (1972). Possible candidates for turbulent electron transport are the TEM (Kadomtsev *et al.*, 1971) ($k_\perp \rho_i \sim 1$ in TEM) and the toroidal ETG mode ($k_\perp \rho_e \sim 1$ in ETG). While ITG turbulence produces turbulent electron heat transport as well as ion heat transport, it is too small to explain the measured electron heat transport.

For the electron heat transport physics, important experimental work has been done at Tore Supra. The first observation of the existence of a critical temperature gradient $dT_e/dr|_c$ for electron transport was reported by Hoang *et al.* (2001) and showed dependence of $dT_e/dr|_c$ on the magnetic shear as $R/L_T = 5 + 10|s|/q$, where $s = rdq/dr/q$ is the magnetic shear (see Fig. 68).

Turbulent transport by ETG is thought to be much smaller than that by ITG due to its small scale $k_\theta \rho_e \sim 1$ until year 2000. Dorland *et al.* (2000) and Jenko *et al.* (2000a) showed a large level of ETG turbulent transport (60 times gyro Bohm transport) associated with a radially elongated streamer, whose saturation mechanism is explained as a Kelvin-Helmholtz instability, when the simulation is done with fixed profiles. Jenko *et al.* (2002) showed that the following theoretical critical temperature gradient dT_{ec}/dr in toroidal

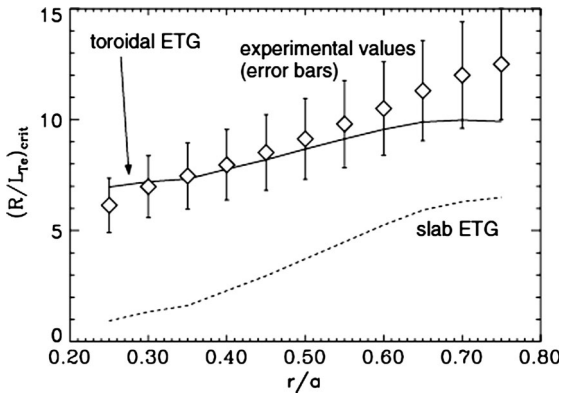

FIG. 69. Comparison of radial profile of $dT_e/dr|_c$ between theory and experiment. From Jenko *et al.*, 2002.

ETG is consistent with the measurement by Hoang *et al.* (2001) as shown in Fig. 69:

$$(R/L_{Te})_{\rm crit} = (1 + \tau_e)(1.33 + 1.91s/q), \tag{128}$$

where $\tau_e = Z_{\rm eff}T_e/T_i$, and s and q are the magnetic shear and safety factor, respectively.

An accurate simulation of ETG turbulence requires a large number of particles and consistent profile evolution. Since the scale length of toroidal ETG is much smaller than that of toroidal ITG, gyrokinetic simulations of ETG turbulence using the quasiballooning formalism by Idomura *et al.* (2005) attain sufficient accuracy more efficiently and allow consistent (but not flux-driven) profile evolution. The simulations showed that the initial turbulence level is close to the result of the flux tube simulation of Jenko, where neither zonal flow nor n coupling has a significant effect. Saturation of ETG turbulence is determined by the quasilinear modification of dT_e/dr close to $dT_e/dr|_c$.

a. Linear mode structure of toroidal electron temperature gradient modes

The ETG mode is characterized by a short wavelength, $k_\theta\rho_{te} \sim 1$ and $k_\theta\rho_{ti} \gg 1$, where k_θ is the poloidal wave number. In this mode, the kinetic ion response vanishes and the ion response becomes adiabatic (Idomura *et al.*, 2000; Jenko *et al.*, 2000b).

In the quasiballooning mode representation of Idomura *et al.* (2005), Φ is expressed as

$$\Phi(r, \theta, \zeta) = \sum_n \Phi_n(r, \theta)e^{-in\zeta + iS(\theta)}, \tag{129}$$

$$S(\theta) = nq(r_s)\chi(\theta), \tag{130}$$

$$\chi(\theta) = \frac{1}{q(r_s)} \int_0^\theta \frac{\boldsymbol{B}\cdot\nabla\zeta}{\boldsymbol{B}\cdot\nabla\theta'}\bigg|_{r=r_s} d\theta'. \tag{131}$$

Here $\Phi_n(r, \theta)$ becomes a slowly varying function, q is the safety factor, χ is a poloidal straight field line angle at $r = r_s$, and r_s is the radius of the reference magnetic surface where the ETG may be most unstable (namely, the radius where dT_e/dr is largest). In order to satisfy the periodic boundary condition in the poloidal direction, $\Phi_n(r, \theta)$ is solved under the boundary condition of $\Phi_n(r, 0) = \Phi_n(r, 2\pi)e^{iS(2\pi)}$.

Figure 70(a) shows a typical linear eigenmode structure of toroidal ETG in poloidal cross section. The mode shows a ballooning character, having a large amplitude in the outer part, and has a radially elongated structure similar to the eigenfunction of toroidal ITG but is much finer in the poloidal direction with typical length $\sim 100\rho_e$, which is well expressed by the ballooning eigenfunction. As shown in Fig. 70(b), poloidal harmonics densely overlap radially for positive shear. In the case of the NS plasma, the ETG eigenmode becomes almost a single mode if dT/dr is largest near the $q_{\rm min}$ location.

b. Streamer and zonal flow in the electron temperature gradient turbulence

In the NS configuration, the ETG shows two different structures, streamer and zonal flow. Figure 71 shows a nonlinear toroidal ETG simulation with the profile evolution in a NS plasma (Idomura *et al.*, 2005). In the positive-shear

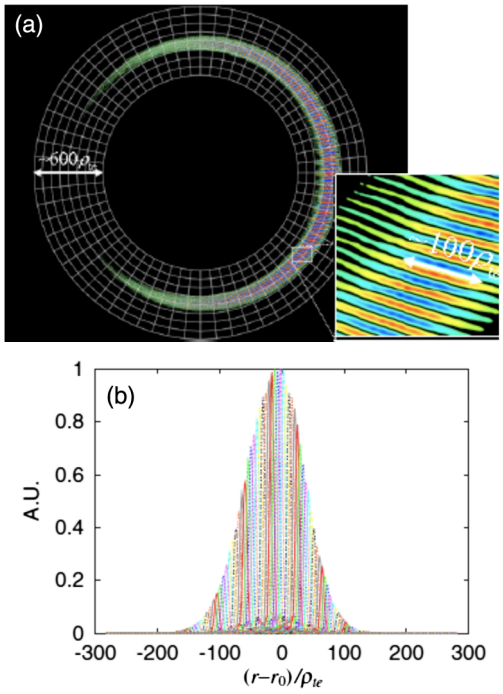

FIG. 70 (color online). (a) Poloidal cross section and (b) radial harmonics of the linear toroidal ETG eigenmode in positive shear. From Idomura *et al.*, 2005.

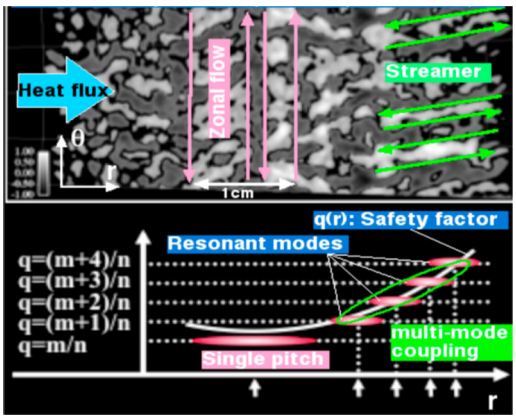

FIG. 71 (color online). ETG turbulence structures of zonal flow and streamers in NS plasma. From Idomura *et al.*, 2005.

region, nonlinear toroidal ETG turbulence produces a streamer through coupling among poloidal harmonics, which exhibits a 3D turbulence. While zonal flow is excited in ITG turbulence by the modulational instability in a positive-shear tokamak, the zonal flow generation is weak for ETG turbulence in the case of positive shear. However, near the $q_{\rm min}$ in the NS plasma, nonlinear ETG turbulence is dominated by a single poloidal mode, which produces zonal flow through an inverse cascade in 2D turbulence.

c. Zonal flow in $s \sim 0$ electron temperature gradient turbulence

When the distance between neighboring-mode rational surfaces is much larger than the electron gyroradius, $\Delta r \sim \rho_{te}/s \gg \rho_{te}$, the ETG turbulent structure becomes two dimensional. The electrostatic gyrokinetic Vlasov-Poisson system with gyrokinetic electron and adiabatic ion in the limit of

$k_\parallel \to 0$ gives a Hasegawa-Mima (HM) (Hasegawa *et al.*, 1977) type of equation for the electron dynamics (Idomura *et al.*, 2006),

$$\frac{\partial}{\partial t}(\rho_s^2\nabla_\perp^2\phi - \tau\phi) + \boldsymbol{b}\times\nabla_\perp\phi\cdot(\rho_s^2\nabla_\perp^2\phi + \ln n_0) = 0, \tag{132}$$

where the normalizations $x/\rho_{te} \to x$, $t\Omega_e \to t$, $e\phi/T_e \to \phi$, and $n_0/\langle n_0\rangle \to n_0$ are made and $\rho_s^2 = 1 + \lambda_{De}^2/\rho_{te}^2$ and $\tau = T_e/T_i$. Here it should be noted that the main nonlinearity in the original HM equation comes from $E\times B$ convection of the ion polarization drift. Nonlinearity for this electron HM (eHM) equation comes from the effects of Debye shielding, electron polarization, and finite electron Larmor radius.

This eHM equation conserves the energy $E = \frac{1}{2}\times\langle\rho_s^2(\nabla_\perp\phi)^2 + \tau\phi^2\rangle$ and the potential enstrophy $W = \frac{1}{2}\times\langle\rho_s^2(\nabla_\perp^2\phi)^2 + \tau(\nabla_\perp\phi)^2\rangle$. The nonlinear term $\boldsymbol{b}\times\nabla_\perp\phi\cdot\rho_s^2\nabla_\perp^2\phi$ leads to an inverse cascade. Balancing with the linear dn_0/dr term gives a critical radial wave number for energy condensation, $k_r \sim k_\beta$, equivalent to the Rhines scale length (Rhines, 1975), which is zonal flow in shearless ETG turbulence.

4. Trapped-electron mode and multiscale turbulence

a. Trapped-electron mode

In collisionless ITG turbulence, a passing electron behaves almost adiabatically while a trapped electron does not, as shown by Dannert *et al.* (2005) using the GENE code. As a result there is some modification of the ITG by the trapped electron. This trapped electron has an important effect in exciting TEMs, which is an ion-scale ($k_\perp\rho_i \sim 1$) instability. The TEM is destabilized by the resonance between the wave and the toroidal precessional drift of trapped electrons and usually rotates in the electron diamagnetic direction.

Gyrokinetic module developments are successful in including trapped-electron dynamics; examples are the linear stability comparison (Rewoldt *et al.*, 2007) between the GT3D code (Idomura *et al.*, 2003) and the GTC code (Lin *et al.*, 1998), quasilinear formulations related to particle transport (Bourdelle *et al.*, 2007; Fable *et al.*, 2008), and small-scale gyrokinetic turbulence simulation (Dannert *et al.*, 2005). Inclusion of trapped-electron dynamics in the gyrofluid code TGLF (Staebler *et al.*, 2005) has also been successful.

TEMs also have a critical temperature gradient R/L_{T_e}, which depends on R/L_{n_e} and the trapped-particle fraction f_t. For the flat density regime, the ITG is the most unstable electrostatic mode. For large R/L_{ne} (peaked density), the ITG tends to be stabilized while the TEM is destabilized by the density gradient. Depending on the local plasma parameters, ITG modes and TEMs may coexist, especially at large R/L_T as shown by Garbet *et al.* (2004) (see Fig. 72). Ryter *et al.* (2005) examined critical temperature gradient transport at ASDEX-U showing that the ETG is stable [the critical temperature gradient given by Eq. (128) is not exceeded in their case] and can be explained by TEMs.

Since the TEM is destabilized by the resonant interaction of the modes with the trapped electron in its toroidal precession, the TEM can be stabilized by modifying the toroidal precession by the finite-beta (or Shafranov shift) effect

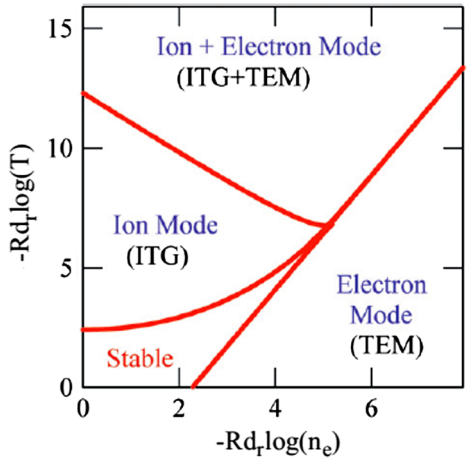

FIG. 72 (color online). Stability diagram of ITG and TEM modes for $T_e = T_i$, trapped-electron fraction of 0.3, and collisionless limit ($\nu_* = 0$). From Garbet *et al.*, 2004.

(Rosenbluth *et al.*, 1971). Here the toroidal precession frequency $\langle\dot{\zeta}\rangle$ is given by

$$\langle\dot{\zeta}\rangle = \frac{1}{e_a}\frac{\partial J/\partial\psi}{\partial J/\partial E}, \tag{133}$$

where $J = \int m_a v_\parallel dl_\parallel$, ψ, and E are the longitudinal adiabatic invariant, poloidal flux, and particle kinetic energy, respectively. Since NS also changes the trapped-electron precession drift, Beer *et al.* (1997) tried to explain the ERS improved confinement (Levinton *et al.*, 1995) by a combination of NS and Shafranov shift effects.

Recently, Camenen *et al.* (2007) found a factor of 2 improved electron confinement in L-mode discharges at TCV by negative triangularity. Marinoni *et al.* (2009) analyzed the effect of change in the trapped-electron precession drift by negative triangularity on TEM turbulent transport to explain this improved confinement.

b. Multiscale turbulence

In Secs. VI.A.2 and VI.A.3, we discussed the current understanding of ITG and ETG turbulence simulations, which assume an adiabatic electron for the ITG [$\delta f_e/F_M = e\delta\phi(\boldsymbol{x}, t)/T_e$] and an adiabatic ion for the ETG [$\delta f_i/F_M = -Z_i e\delta\phi(\boldsymbol{x}, t)/T_i$].

Candy *et al.* (2007) made a GYRO flux tube simulation of the whole spectrum of low-β instabilities (ITG, TEM, and ETG) showing that the adiabatic ion approximation in ETG turbulence is not always a good one. One of the important kinetic effects is zonal flow generation by a kinetic ion treatment. On the other hand, backreaction of the ETG on ITG turbulence is insignificant as predicted by Holland *et al.* (2004). Gorler *et al.* (2008a) showed scale separation between the electron and ion in their ITG-ETG multiscale simulation using the GENE code, and Gorler *et al.* (2008b) also showed the significance of kinetic ions in ETG turbulent transport. Multiscale gyrokinetic simulation of ITG, TEM, and ETG turbulence is an active field for further development.

5. Electromagnetic turbulence

An efficient steady-state tokamak reactor necessarily operates at high normalized beta. The thermal energy confinement time showed strong degradation of $\tau_{E_{\rm th}}$ with β, $\tau_{E_{\rm th}} \propto \beta^{-7/12}$, using a saturated-Ohmic and NB-heated L-mode database from ASDEX and JT-60 (Kikuchi, 1993). While the β dependence of empirical thermal H-mode confinement scaling is still evolving (Takizuka *et al.*, 2006; McDonald *et al.*, 2008), dedicated confinement scaling experiments on β by Urano *et al.* (2006) at JT-60U and Vermale *et al.* (2007) at ASDEX-U showed strong degradation of energy confinement with β close to the IPB98$(y,2)$ scaling of $B\tau_{E_{\rm th}} \propto \beta^{-0.9}$ (ITER Physics Expert Group, 1999).

Thus it is important to clarify the variation of turbulent transport with β. As the plasma β increases, the plasma turbulence exhibits an EM feature, which modifies especially the ITG turbulence. There are two candidates for EM turbulence, the kinetic ballooning mode (KBM) of Tang *et al.* (1980) and the microtearing mode of Drake *et al.* (1977).

The linear stability of the KBM with the ideal ballooning mode was analyzed by Hong *et al.* (1989), and its gyrofluid turbulence simulation was given by Snyder *et al.* (2001). Pueschel *et al.* (2008) showed that, depending on the parameters, the growth rate of the ITG is reduced as the plasma beta increases and the ITG-TEM transition occurs (say, at $\beta \sim 1\%$), and finally transition to the KBM occurs (say, at $\beta \sim 1.3\%$). Nonlinear turbulent simulation of finite-β ITG turbulence was undertaken by Pueschel *et al.* (2010), showing that the Dimits shift due to zonal flow becomes larger with β and stabilizes the ITG mode over a wide range of β. This tendency is opposite to the experimental observation of strong transport enhancement with β.

The microtearing mode was first studied by Drake *et al.* (1977); it is driven by dT/dr in the collisional or semicollisional regime and can be a potential candidate for electron anomalous transport due to a mechanism suggested by Richester *et al.* (1978) with $\tilde{B}_x/B_0 \sim \rho_e/L_{T_e}$ (Drake *et al.*, 1980). The importance of the microtearing mode was first noted by Kotschenreuther *et al.* (2000) in the spherical tokamak (ST). Applegate *et al.* (2007) clarified the key driving parameters as β and magnetic drift, which are not unique to the ST. Guttenfelder *et al.* (2011) showed that nonlinear gyrokinetic microtearing mode simulation gives transport comparable to results from NSTX (see Fig. 73).

Doerk *et al.* (2011) also showed through gyrokinetic microtearing mode simulation that electron heat transport by the microtearing mode follows the formula by Richester *et al.* (1978) and can be important in standard tokamaks. Understanding electromagnetic turbulent transport has just started and needs further development for the quantitative understanding of β degradation in thermal confinement.

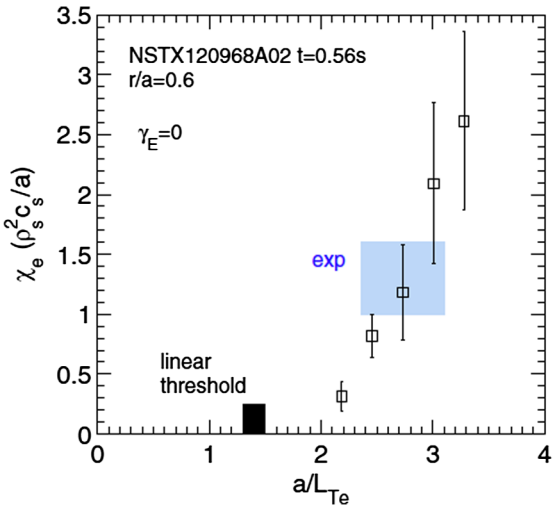

FIG. 73 (color online). Normalized electron thermal diffusivity vs a/L_{T_e} from gyrokinetic simulation compared with experiment. From Guttenfelder *et al.*, 2011.

B. Transport barriers

1. Turbulence suppression

a. Flow shearing of turbulence

The turbulence can be affected by the flow shear and also by the flow itself, the latter through the Coriolis and centrifugal forces. Flow shear suppression of turbulent transport was discovered by Biglari *et al.* (1990). Hahm *et al.* (1994, 1995) gave a condition for flow-shear-induced fluctuation suppression as follows:

$$\Delta\omega_T \le \omega_E, \tag{134}$$

$$\omega_E = \left| \frac{\Delta\psi}{\Delta\zeta} \frac{d^2\Phi(\psi)}{d\psi^2} \right|, \tag{135}$$

where $\Delta\omega_T$ and ω_E are the decorrelation rate of the ambient turbulence and the shearing rate due to flow shear, respectively. Here $\Delta r = \Delta\psi/RB_\theta$ and $R\Delta\zeta$ are radial and the toroidal correlation lengths of turbulence, respectively. The correlation length perpendicular to $\boldsymbol{B}$, $L_\perp$, is given as $L_\perp^{-1} \sim m/r = nq/R \sim B_\zeta/B_\theta\Delta\zeta R$. If the radial correlation length of turbulence $\Delta r \approx L_\perp$ (Waltz *et al.*, 1994), the shearing rate is given by $\omega_E = (R^2B_\theta^2/B)d^2\Phi/d\psi^2 = (RB_\theta/B)d[(d\Phi/dr)/RB_\theta]/dr$.

There are two sources of flow shear in tokamaks, namely, zonal flow driven by turbulence itself (Diamond *et al.*, 2005) and global E_r shear determined by the radial force balance. The zeroth-order radial force balance equation (74) [or Eq. (118)], which is robust even in turbulent plasma (Idomura *et al.*, 2009), plays an important role in the shearing

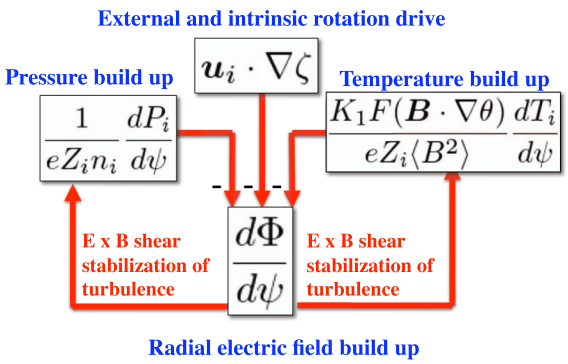

FIG. 74 (color online). Schematic diagram of positive feedback effect on E_r from dP_i/dr, dT_i/dr, and v_ζ.

rate ω_E in tokamaks as a positive feedback effect of turbulent transport suppression by flow shear (see Fig. 74).

When the ITB builds up, both $dP_i/d\psi$ and $dT_i/d\psi$ increase. If there is no change in external toroidal rotation drive, the radial electric field $d\Phi/d\psi$ builds up in response to $dP_i/d\psi$ and $dT_i/d\psi$. Therefore, E_r shear is enhanced when pressure curvature d^2P_i/dr^2 and/or temperature curvature d^2T_i/dr^2 is formed. Once E_r shear is enhanced, further turbulence decorrelation occurs to enhance the ITB. This positive feedback effect may lead to a steep ITB unstable to MHD instability.

Toroidal angular flow $\omega_t = \boldsymbol{u}_i \cdot \nabla\zeta$ driven by either external or intrinsic torque (by residual turbulence and turbulence spreading) further produces a radial electric field. The toroidal angular flow shear $d\omega_t/dr$ enters into the dynamics of the positive feedback loop in ITB formation.

b. Precession deresonance of trapped-electron modes

For trapped-particle instabilities, the Shafranov shift measured by $\alpha = -q^2 R d\beta/dr$, magnetic shear $[s = R(dq/dr)/q]$-and negative triangularity have important effects on the precession drift and are effective in reducing resonance between wave and trapped-electron precession.

Taylor *et al.* (1993) reported very high confinement (the so-called VH mode) at DIII-D associated with strong $E \times B$ flow shear. They also suggested that in this core improved confinement local shear reversal in the unfavorable curvature region, high β_p, and strong shaping are favorable for drift reversal of trapped particles and stabilization of trapped-particle modes. Recent TCV negative triangularity results (Camenen *et al.*, 2007; Marinoni *et al.*, 2009) support the effects of trapped-electron-drift modification on suppression of TEM turbulence.

2. Edge and internal transport barriers

The formation of an ETB is associated with the H mode. There are a number of review papers on the H mode (ASDEX team, 1989; Connor *et al.*, 2000) and radial electric field (Itoh *et al.*, 1996; Ida *et al.*, 1998). The ETB in the H mode is discussed in detail in the ITER physics basis (ITER Physics Expert Group, 1999; Doyle *et al.*, 2007) and has common features with the ITB. A larger ETB width is preferable to support large plasma energy with its pedestal. Recently, Urano *et al.* (2008) concluded that the scaling of ETB width follows $\Delta_{\rm ped} \propto a\rho *_{\rm pol}^{0.2} \beta_p^{0.5}$, where $\rho *_{\rm pol} = \rho_{\rm pol}/a$. This scaling also supports the high-β_p operation adopted in the SSTR design.

The ITB was first discovered by Koide *et al.* (1994) associated with core improved confinement with positive magnetic shear (see Fig. 52). Its characteristics have been discussed at WS by Koide *et al.* (1996), in a comparison between WS and NS by Koide *et al.* (1998a), and in a comparison between JT-60U and DIII-D NS by Koide *et al.* (1998b). Sometimes the improved confinement inside the $q = 1$ surface discussed by Kamada *et al.* (1992) and by Hugon *et al.* (1992) is also called ITB. A review of the ITB has been given by Wolf *et al.* (2003).

Figure 75 is a typical profile with an ITB in a NS plasma. Using the radial electric field expression (54), the $E \times B$ shearing rate calculated using measured profiles is of the

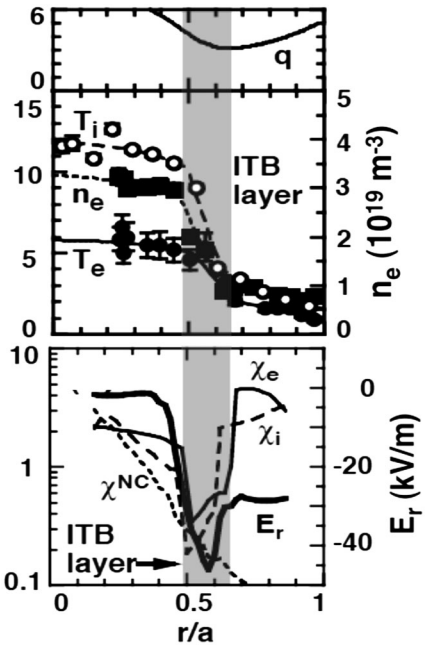

FIG. 75. ITB profiles in NS shear plasma and E_r, χ_i, and χ_e profiles. From Shirai *et al.*, 1999.

order of $\omega_E \sim 10^5$ s^{-1} as compared with $v_{ti}/R \sim 2.7 \times 10^5$ s^{-1}, the ion thermal diffusivity inside the ITB is close to neoclassical, and electron thermal diffusivity is also significantly reduced in the NS plasma (Shirai *et al.*, 1999, 2000). Here "neoclassical" means the formula obtained from the moment equation (8.134) in Kikuchi (2011b) since the Chang-Hinton formula (Chang *et al.*, 1986) overestimates the impurity effect. This steep ITB is associated with a jump in the E_r shear [see also Sakamoto *et al.* (2004)] due to the temperature curvature formation later discussed as a curvature transition by Ida *et al.* (2008).

A radial correlation measurement using a correlation reflectometer in a NS plasma by Nazikian *et al.* (2005) showed a long correlation length $L_r \sim 20$ cm in the L-mode phase and $L_r \leq 4$ mm in the ITB. These characteristics seem to be consistent with theoretical understanding of the avalanche and streamer in the L mode and the $E \times B$ flow shear turbulence decorrelation discussed above.

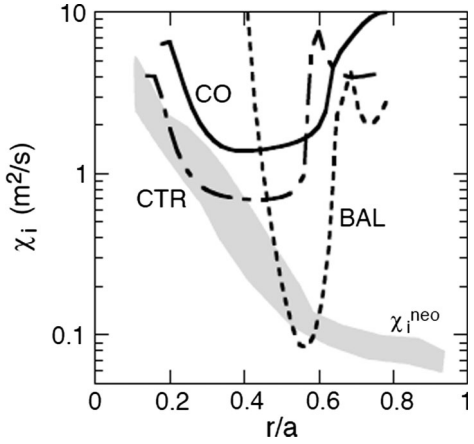

FIG. 76. Difference in χ_i of ITBs in balanced, co- and counter-NB injection in NS plasma. From Sakamoto *et al.*, 2001.

In the NS plasma, a steep ITB tends to be formed in balanced neutral injection, while a wider and weaker ITB is formed in the co-NB and counter-NB injection cases shown in Fig. 76 by Sakamoto *et al.* (2001). Since too strong ITB tends to trigger plasma disruption, control of the ITB strength through the toroidal rotation drive was pursued by Sakamoto *et al.* (2005).

The magnetic shear dependence of ITG heat transport studied by Waltz *et al.* (1995) showed no particular role of $q_{\min}$ but showed reduced transport with negative shear. Breakup of the eigenmode across the $q_{\min}$ surface was discussed as a possible cause of ITB formation in a NS plasma by Kishimoto *et al.* (1999) and in flux-driven gyrofluid simulations of ITG turbulence by Garbet *et al.* (2001, 2002), but it may not be relevant due to the omission of the nonresonant mode (Candy *et al.*, 2004; Miyato *et al.*, 2007). Miyato *et al.* (2007) indicated stronger zonal flow excitation at low $q_{\min}$ as an alternative candidate for ITB formation. At present, there is no quantitative explanation of ITB formation by gyrofluid and gyrokinetic simulations.

The formation of ITB starts at the central negative-shear region and propagates just before the $q_{\min}$ location shown by Koide *et al.* (1996) for the WS plasma and by Fujita *et al.* (1998) for the NS plasma. These observations may be consistent with the prediction by Lebedev *et al.* (1997) of a density ITB. Sauter *et al.* (2005) showed control of electron ITB through perturbation of the current profile at TCV.

VII. CONTROL ISSUES OF ADVANCED TOKAMAK OPERATION

A. Density profile control

Density profile control is an important subject for steady-state tokamak operation since dn/dr also drives the bootstrap current and the fusion power density $P_f \propto n^2$. For a fusion reactor such as the SSTR, the power and particle balance in the SOL requires high density outside the separatrix $n_e|_{\mathrm{SOL}} \sim (6\text{–}8) \times 10^{19}$ m^{-3} (Ueda *et al.*, 1992). But it is preferable to have a moderately peaked density gradient including a density ITB toward the core region.

Jenko *et al.* (2000a) found particle pinch (thermodiffusion) in a nonlinear simulation for a collisionless sheared slab plasma. Yancov (1994) proposed another mechanism called turbulent equipartition predicting a velocity proportional to the curvature of the magnetic field. Garbet *et al.* (2003) showed the existence of particle pinches in a gyrofluid simulation of ITG and TEM turbulence.

Thermodiffusion (or off-diagonal particle flux driven by dT/dr) was reported by Nagashima *et al.* (1995) using electron cyclotron resonance heating, which is the key for density peaking in the collisionless regime (Jenko *et al.*, 2000b). Hoang *et al.* (2003) reported the existence of particle pinch in the full CD plasma, where the neoclassical Ware pinch (Ware *et al.*, 1970) vanishes. This density peaking was found to be related to low collisionality (Angioni *et al.*, 2003) and has been confirmed in many tokamaks (see Fig. 77).

The quasilinear particle flux Γ_{QL} determined using the gyrokinetic equation was given by Angioni *et al.* (2009),

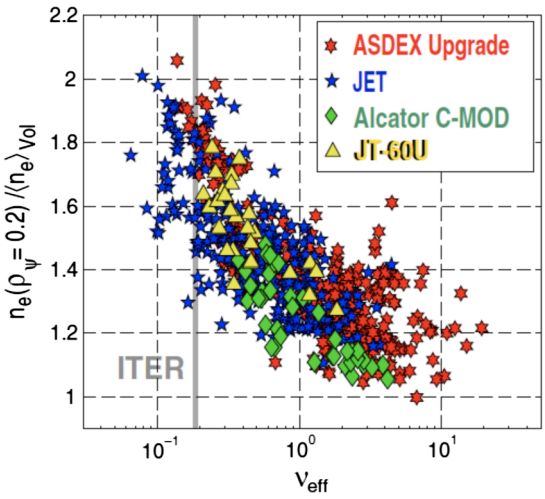

FIG. 77 (color online). Density peaking factor as a function of effective collisionality. From Angioni *et al.*, 2009.

$$R\Gamma_{\mathrm{QL}}/n_e = DR/L_n + D_T R/L_{T_e} + RV_p, \tag{136}$$

where Γ_{QL}, D, D_T, and V_p are the quasilinear particle flux, particle diffusion coefficient, thermodiffusion coefficient, and convective velocity, respectively. This gives the stationary condition of the density profile as $R/L_n = -(D_T/D_n)R/L_T - RV_p/D_n$.

Fable *et al.* (2006) observed strong coupling between the n_e and T_e profiles related to a strong inward pinch of a thermodiffusive type at TCV. A moderately peaked density profile is expected for ITER (Pereverzev *et al.*, 2005), which

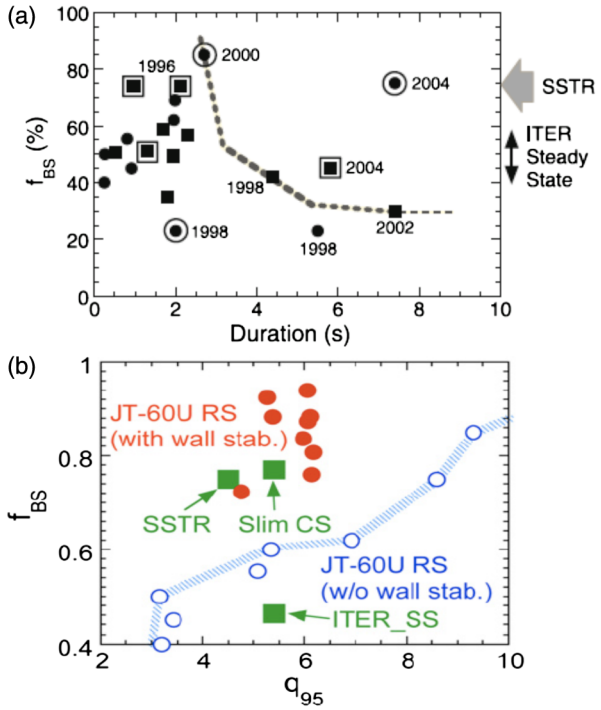

FIG. 78 (color online). (a) Extended high bootstrap current fraction discharge duration obtained by rotation control. From Sakamoto *et al.*, 2005. (b) Attainment of reactor-relevant moderate-q_{95} high bootstrap current fraction discharge with wall stabilization. From Sakamoto *et al.*, 2009.

is a good sign for SSTRs but further understanding of density profile physics and density ITB is required.

B. Control of internal transport barrier strength

An integrated demonstration of a fully noninductive operation with a large bootstrap current fraction is of primary importance in realizing the steady-state tokamak reactor. Significant progress has been made in large tokamaks such as JT-60U (Sakamoto *et al.*, 2005, 2009), as shown in Fig. 78, and DIII-D (Murakami *et al.*, 2006; Holcomb *et al.*, 2009) toward this goal. ITB-induced disruption works against maintenance of the reactor-relevant q_{95} regime [see Fig. 78(b)] (Sakamoto *et al.*, 2009) and further understanding of ITB transport physics and its control is required.

C. Edge bootstrap current

Excitation of the edge bootstrap current in a collisionless plasma (see Fig. 49) is problematic for the edge MHD stability. Active reduction of the edge bootstrap current is an important subject for future tokamak research. Fisch (1984) proposed a current drive by phased pellet injection, which could be applied to edge bootstrap current control. Helander *et al.* (2001, 2006) actually proposed control of the edge bootstrap current by up-down asymmetric heating and pellet injection. To improve edge stability, we have to control the edge bootstrap current.

VIII. SUMMARY

During the past 20 years, operating regimes relevant to the steady-state tokamak reactor have been extensively explored. We reviewed here mainly the physical understanding behind the experiments on parallel transport, MHD stability, and perpendicular transport related to the steady-state operation of the tokamak. Progress has been quite remarkable compared to that in the years before the creation of the reactor concepts.

In particular, collisional parallel transport such as the generalized Ohm's law and neoclassical rotation and ideal MHD including the continuous spectrum are now understood fairly well. Intrinsic rotation driven by the Reynolds stress is a new subject in parallel transport. The resistive and kinetic MHD modes are now generally well understood although some problems are left for future development. Gyrokinetic theory and simulations have led to great progress in understanding the physics of electrostatic turbulence. But further development is still needed in the area of multiscale turbulence. Also the investigation of electromagnetic turbulence has just started and EM turbulence seems somewhat different from electrostatic turbulence. Flow shear suppression of turbulence and the zonal and GAM flow paradigm help toward overall understanding. Great effort should be placed on the development of gyrokinetic EM multiscale turbulence simulations and on clarification of turbulent physics for testing against advanced tokamak experiments.

Figure 79 shows the control flow for steady-state tokamak operation. The plasma control knobs are CD, magnetic perturbation (MP), fueling, heating, and torque drive. These lead

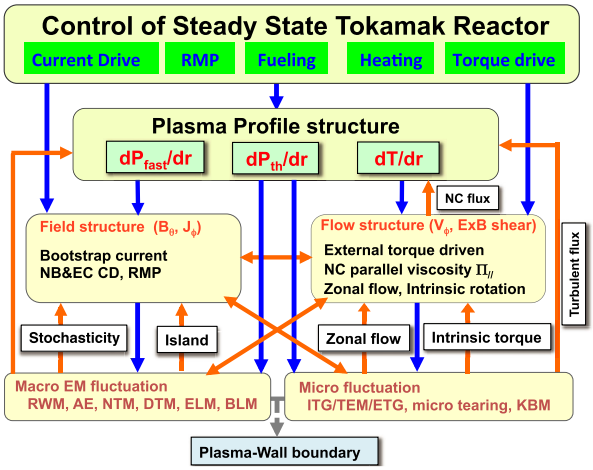

FIG. 79 (color online). Control flow for steady-state tokamak operation. Plasma profile, field, flow, macrofluctuations, and microfluctuations are interlinked and complex, while control knobs are not plentiful.

to the formation of pressure and temperature profiles, magnetic field structure, and flow structure. The plasma profile and field and flow structures lead to the excitation of macrofluctuations and microfluctuations and cause backreactions to the field and flow structures as well as the plasma profiles. These are closely related to each other and many processes are interlinked. Some physics elements are still not well known, such as electromagnetic turbulence and some kinetic MHD modes. To realize steady-state tokamak operation, further understanding of the physics of field and flow structures, microfluctuations, and macrofluctuations is necessary. Furthermore, detailed knowledge of the response of each element is necessary. Since advanced tokamak operation has various autonomous features and some conflicts between MHD and transport, resolution of the issues related to the ITB and ETB has to be addressed in parallel with individual understanding of the physics.

This review deals only with core physics due to our limited knowledge of edge, divertor, and plasma-wall interaction physics and also page limits. But steady-state operation requires control of divertor power handling, fueling, recycling, tritium inventory through SOL or divertor plasma control, and development of materials for the first wall and divertor. A review of these important issues should be undertaken in the near future to summarize the current status of physics behind magnetic fusion research in steady-state tokamak reactor concepts.

LIST OF SYMBOLS AND ABBREVIATIONS

ITER	Fusion experimental reactor under construction in France
JT-60U	JAERI tokamak 60 at Japan
JET	Joint European Torus at UK
TFTR	Tokamak Fusion Test Reactor at US
DIII-D	Advanced tokamak facility at US
ASDEX Upgrade	Tokamak facility at Germany
SSTR	Tokamak reactor design at Japan

ARIES-I	Tokamak reactor design at US
WS	Weak shear
NS	Negative shear
CH	Current hole
ETB	Edge transport barrier
ITB	Internal transport barrier
N-NBI	Negative-ion based NBI
NBCD	Neutral beam current drive
ECCD	Electron cyclotron current drive
NTM	Neoclassical tearing mode
DTM	Double tearing mode
RWM	Resistive wall mode
SAR	Shear Alfvén resonance
KAW	Kinetic Alfvén wave
RAF	Reduced activation ferritic steel
ELM	Edge localized mode
BLM	Barrier localized mode
RMP	Resonant magnetic perturbation
TAE	Toroidal Alfvén eigenmode
GAE	Global Alfvén eigenmode
RSAE	Reversed shear Alfvén eigenmode
SOC	Self-organized criticality
ITG	Ion temperature gradient
ETG	Electron temperature gradient
TEM	Trapped electron mode
KBM	Kinetic ballooning mode
GAM	Geodesic acoustic mode
SOL	Scrape off layer

ACKNOWLEDGMENTS

The authors acknowledge discussions in the past 20 years with R. Conn, Y. Seki, F. Najmabadi, K. Tobita, and K. Okano on reactor design; R. Hawryluk, R. Goldston, R. Stambaugh, T. Taylor, S. Ishida, Y. Kamada, M. Wade, and T. Luce on advanced tokamak research; R. Bickerton, M. Zarnstorff, and W. Houlberg on bootstrap currents; N. Fisch, K. Tani, M. Taguchi, T. Oikawa, S. Suzuki, A. Polevoi, C. Forest, M. Honda, K. Hamamatsu, and P. Helander on current drive; T. Oikawa and S. Suzuki on multistep ionization; Y. B. Kim and K. C. Shaing on toroidal rotation; P. Diamond, K. Ida, K. Itoh, J. Rice, K. Nagashima, and M. Yoshida on intrinsic rotation; S. Tokuda, T. Ozeki, J. Manickam, M. Hirota, and J. Shiraishi on ideal MHD; T. Fujita, C. Hawkes, and T. Takizuka on the current hole, Y. Koide, T. Fujita, H. Shirai, Y. Sakamoto, and H. Urano on the ITB and ETB; J. Callen, H. Zohm, A. Isayama, and N. Hayashi on NTMs; M. Takechi, S. Sabbagh, G. Matsunaga, G. Kurita, and T. Hender on RWMs; Y. Kamada, N. Oyama, N. Aiba, and N. Hayashi on ELMs; T. Evans on RMP; K.Wong, C. Z. Cheng, J. van Dam, H. Berk, H. Kimura, Y. Kusama, A. Fukuyama, R. Nazikian, K. Shinohara, M. Lesur, R. White, and G. Kramer on TAEs; Y. Ishii, S. Takeji, and Y. Kishimoto on DTMs; A. Hasegawa, P. Diamond, T. S. Hahm, Y. Idomura, Y. Kishimoto, X. Garbet, S. Itoh, A. Fujisawa, N. Miyato, K. Miki, G. Hoang, Z. Lin, G. Conway, T. Ido, and Y. Nagashima on drift wave turbulence; W. Gutterfelder on microtearing turbulence; and C. Angioni, K. Nagashima, and H. Takenaga on particle transport. The authors also acknowledge the referees for their valuable comments.

APPENDIX

1. Friction and viscosity matrix

The normalized friction matrix for electron, ion, impurity, and fast ion is as follows:

$$\hat{\boldsymbol{L}}=\begin{bmatrix} \hat{l}_{11}^{ee} & \hat{l}_{11}^{ei} & \hat{l}_{11}^{eI} & \hat{l}_{11}^{ef} & -\hat{l}_{11}^{ee} & -\hat{l}_{11}^{ei} & -\hat{l}_{11}^{eI} \\ \hat{l}_{11}^{ie} & \hat{l}_{11}^{ii} & \hat{l}_{11}^{iI} & \hat{l}_{11}^{if} & -\hat{l}_{11}^{ie} & -\hat{l}_{11}^{ii} & -\hat{l}_{11}^{iI} \\ \hat{l}_{11}^{Ie} & \hat{l}_{11}^{Ii} & \hat{l}_{11}^{II} & \hat{l}_{11}^{If} & -\hat{l}_{11}^{Ie} & -\hat{l}_{11}^{Ii} & -\hat{l}_{11}^{II} \\ \hat{l}_{11}^{fe} & \hat{l}_{11}^{fi} & \hat{l}_{11}^{fI} & \hat{l}_{11}^{ff} & 0 & 0 & 0 \\ -\hat{l}_{21}^{ee} & -\hat{l}_{21}^{ei} & -\hat{l}_{21}^{eI} & -\hat{l}_{21}^{ef} & \hat{l}_{22}^{ee} & \hat{l}_{22}^{ei} & \hat{l}_{22}^{eI} \\ -\hat{l}_{21}^{ie} & -\hat{l}_{21}^{ii} & -\hat{l}_{21}^{iI} & 0 & \hat{l}_{22}^{ie} & \hat{l}_{22}^{ii} & \hat{l}_{22}^{iI} \\ -\hat{l}_{21}^{Ie} & -\hat{l}_{21}^{Ii} & -\hat{l}_{21}^{II} & 0 & \hat{l}_{22}^{Ie} & \hat{l}_{22}^{Ii} & \hat{l}_{22}^{II} \end{bmatrix}. \quad \text{(A1)}$$

The normalized viscosity matrix for electron, ion, impurity, and fast ion is as follows:

$$\hat{\boldsymbol{M}}=\begin{bmatrix} \hat{\mu}_{e1} & 0 & 0 & 0 & \hat{\mu}_{e2} & 0 & 0 \\ 0 & \hat{\mu}_{i1} & 0 & 0 & 0 & \hat{\mu}_{i2} & 0 \\ 0 & 0 & \hat{\mu}_{I1} & 0 & 0 & 0 & \hat{\mu}_{I2} \\ 0 & 0 & 0 & \hat{\mu}_{f1} & 0 & 0 & 0 \\ \hat{\mu}_{e2} & 0 & 0 & 0 & \hat{\mu}_{e3} & 0 & 0 \\ 0 & \hat{\mu}_{i2} & 0 & 0 & 0 & \hat{\mu}_{i3} & 0 \\ 0 & 0 & \hat{\mu}_{I2} & 0 & 0 & 0 & \hat{\mu}_{I3} \end{bmatrix}. \quad \text{(A2)}$$

The friction coefficients between fast ions and thermal species are given partially by Kikuchi (1990b) for l_{11}^{af} and l_{11}^{fa} and full derivations of l_{ij}^{af} and l_{ij}^{fa} are given by Wang *et al.* (1994) and are summarized by Kikuchi *et al.* (1995b). The viscosity coefficient for thermal species is given in a velocity space partitioned form by Hirshman *et al.* (1977). Here the coefficients are given in a slightly different form (Kikuchi *et al.*, 1995b). The viscosity coefficient is proportional to the deflection frequency ν_D^a in the collisionless limit ($\nu_{\rm tot}^a \to \nu_D^a$). This is consistent with the physical explanation of the viscous force in Sec. IV.A.2 and is important for an evaluation including non-negligible impurity content. A slightly improved viscosity formula is given by Shaing *et al.* (1996) and used in the NCLASS package (Houlberg *et al.*, 1997). Since Hirshman's approximate Coulomb collision operator gives insufficient accuracy especially for the electron viscosity, Sauter *et al.* (1999) and Angioni *et al.* (2000) used a full Fokker-Planck collision operator to evaluate the approximate neoclassical formula.

2. Viscosity coefficients for fast ions

A viscosity coefficient for a fast particle using the Stix slowing down distribution function was obtained by Azumi *et al.* (1990). The basic procedure for derivation of a viscosity coefficient is to solve the drift kinetic equation (DKE) $(\boldsymbol{v}_\parallel + \boldsymbol{v}_D)\cdot\nabla f = C(f) + S$ successively by gyroradius ordering as $f = f^0 + f^1 + \cdots$. The lowest-order DKE and its solution are $\boldsymbol{v}_\parallel \cdot \nabla f^0 = C(f^0) + S(\psi)\delta(v - v_{f0})$ and

$$f^0(\psi, v) = \frac{\tau_s}{\tau_{th}} \frac{n_f}{4\pi(v^3 + v_c^3)} H(v_{f0} - v),$$

respectively. The fast-ion density is given by $n_f = 4\pi S\tau_{\rm th}$. Here H is the Heaviside function. This solution is called a Stix solution (Stix *et al.*, 1972).

By using

$$\boldsymbol{v}_D \cdot \nabla f^0 = v_\parallel \boldsymbol{b} \cdot \nabla\left[\frac{I v_\parallel}{\Omega}\frac{\partial f^0}{\partial \psi}\right],$$

the first-order DKE is given as

$$v_\parallel \boldsymbol{b} \cdot \nabla\left[f^1 + \frac{m_f I}{e_f B} v_\parallel \frac{\partial f^0}{\partial \psi}\right] = C(f^1). \tag{A3}$$

The solution of Eq. (A3) is also expanded as $f^1 = f_0^1 + f_1^1 + \cdots$ in orders of ν/ν_b and the lowest-and first-order DKEs are given as

$$v_\parallel \boldsymbol{b} \cdot \nabla\left[f_0^1 + \frac{m_f I}{e_f B} v_\parallel \frac{\partial f^0}{\partial \psi}\right] = 0, \tag{A4}$$

$$v_\parallel \boldsymbol{b} \cdot \nabla f_1^1 = C(f_0^1). \tag{A5}$$

The general solution of Eq. (A4) is

$$f_0^1 = -\frac{m_f I}{e_f B} v_\parallel \frac{\partial f^0}{\partial \psi} + g(\psi, v, \lambda)$$

and Eq. (A5) gives the solvability condition for f_0^1. If we define $v_\parallel = \zeta v$ and introduce G by $g = (m_f I v/e_f) \times (\partial f^0/\partial\psi)G$, we obtain the following equation for G:

$$\frac{1}{v^2}\frac{\partial}{\partial v}\left[(v^3 + v_c^3)\left(\left\langle\frac{B}{\zeta}\right\rangle G - H(\lambda_c - \lambda)\right)v\frac{\partial f^0}{\partial \psi}\right] + \hat{Z}\frac{v_c^3}{v^3} v \frac{\partial f^0}{\partial \psi}\frac{\partial}{\partial \lambda}\left[\lambda\left(2\langle\zeta\rangle\frac{\partial G}{\partial \lambda} + H(\lambda_c - \lambda)\right)\right] = 0. \tag{A6}$$

The solution of Eq. (A6) is easily obtained in both the pitch-angle scattering limit

$$G = -\frac{1}{2}\int_\lambda^{\lambda_c} \frac{d\lambda}{\langle\zeta\rangle}, \quad \frac{\hat{Z}v_c^3}{v^3} \ll 1,$$

and the slowing down limit

$$G = 1\Big/\left\langle\frac{B}{\zeta}\right\rangle, \quad \frac{\hat{Z}v_c^3}{v^3} \gg 1.$$

The definition of the parallel viscous force is given by $\langle \boldsymbol{B} \cdot \nabla \cdot \boldsymbol{\pi}\rangle = \langle B \int d^3 v m_f v_\parallel^2 \boldsymbol{b} \cdot \nabla f\rangle$. Using Eq. (A5), the parallel viscous force is given by $\langle \boldsymbol{B} \cdot \nabla \cdot \boldsymbol{\pi}\rangle = \langle B \int d^3 v m_f v_\parallel C(f^1)\rangle$. Following the technique of Hirshman *et al.* (1981) [Eq. (4.56)], we obtain the following expression for the parallel viscous force:

$$\langle \boldsymbol{B} \cdot \nabla \cdot \boldsymbol{\pi}\rangle = \frac{\pi m_f^2 I \langle B^2\rangle}{\tau_s e_f f_c}\int v dv \frac{\partial f^0}{\partial \psi}\int d\lambda \Sigma_\sigma \sigma G \cdot \left[f_t \hat{Z} v_c^3 - (v^3 + v_c^3)\left(\frac{\partial\langle|\zeta|\rangle}{\partial\lambda}\int_\lambda^{\lambda_c}\frac{d\lambda}{\langle|\zeta|\rangle} + f_c\right)\right]. \tag{A7}$$

If we define $G = \hat{G}(\psi, v)\int_\lambda^{\lambda_c} d\lambda/\langle|\zeta|\rangle$, the parallel viscous force and poloidal flow are given in the pitch-angle-scattering-dominant regime as follows

$$\langle \boldsymbol{B} \cdot \nabla \cdot \boldsymbol{\pi}\rangle = \frac{4\pi m_f^2 I}{3 e_f \tau_s} f_t \hat{Z} v_c^3 \int v \hat{G}\frac{\partial f^0}{\partial \psi} dv, \tag{A8}$$

$$u_\theta = \frac{4\pi m_f I}{3 e_f \tau_s} f_c \int v^4 \hat{G}\frac{\partial f^0}{\partial \psi} dv, \tag{A9}$$

and their ratio gives the viscosity.

REFERENCES

Aiba, N., *et al.*, 2006, Comput. Phys. Commun. **175**, 269.
Aiba, N., *et al.*, 2009, Nucl. Fusion **49**, 065015.
Aiba, N., *et al.*, 2011, Nucl. Fusion **51**, 073012.
Angelino, P., *et al.*, 2008, Phys. Plasmas **15**, 062306.
Angelino, P., *et al.*, 2009, Phys. Rev. Lett. **102**, 195002.
Angioni, C., *et al.*, 2000, Phys. Plasmas **7**, 1224.
Angioni, C., *et al.*, 2003, Phys. Rev. Lett. **90**, 205003.
Angioni, C., *et al.*, 2009, Plasma Phys. Controlled Fusion **51**, 124017.
Angioni, C., *et al.*, 2011, Phys. Rev. Lett. **107**, 215003.
Antonsen, T., *et al.*, 1982, Phys. Fluids **25**, 1295.
Appert, K., *et al.*, 1974, Phys. Fluids **17**, 1471.
Appert, K., *et al.*, 1982, Plasma Phys. **24**, 1147.
Applegate, D., *et al.*, 2007, Plasma Phys. Controlled Fusion **49**, 1113.
Artsimovich, L., 1972, Nucl. Fusion **12**, 215.
ASDEX team, 1989, Nucl. Fusion **29**, 1959.
Azumi, M., *et al.*, 1981, *Proceedings of the 8th International Conference on Plasma Physics and Controlled Nuclear Fusion Research (Brussels)* (IAEA, Vienna), Vol. 1, p. 293.
Azumi, M., *et al.*, 1990, Japan Atomic Energy Research Institute Technical Report No. JAERI-M 90-066, p. 178, http://jolissrch-inter.tokai-sc.jaea.go.jp/pdfdata/JAERI-M-90-066.pdf.
Bak, P., *et al.*, 1987, Phys. Rev. Lett. **59**, 381.
Barston, E., *et al.*, 1964, Ann. Phys. (N.Y.) **29**, 282.
Batha, S., *et al.*, 1997, Phys. Plasmas **4**, 3614.
Beer, M., *et al.*, 1997, Phys. Plasmas **4**, 1792.
Berk, H., *et al.*, 1992, Phys. Fluids B **4**, 1806.
Berk, H., *et al.*, 1995, Phys. Plasmas **2**, 3007.
Berk, H., *et al.*, 1999, Phys. Plasmas **6**, 3102.
Berk, H., *et al.*, 2001, Phys. Rev. Lett. **87**, 185002.
Berk, H., *et al.*, 2006, Nucl. Fusion **46**, S888.
Bernstein, I., *et al.*, 1958, Proc. R. Soc. A **244**, 17.
Betti, R., *et al.*, 1991, Phys. Fluids B **3**, 1865.
Betti, R., *et al.*, 1992, Phys. Fluids B **4**, 1465.
Bickerton, R., *et al.*, 1971, Nature (London) **229**, 110.
Biglari, H., *et al.*, 1990, Phys. Fluids B **2**, 1.
Biskamp, D., 1993, *Nonlinear Magnetohydrodynamics* (Cambridge University, Cambridge).
Biskamp, D., 2000, *Magnetic Reconnection in Plasmas* (Cambridge University, Cambridge).
Bonderson, A., *et al.*, 1997, Nucl. Fusion **37**, 1419.
Boozer, A., *et al.*, 2005, Rev. Mod. Phys. **76**, 1071.
Bortolon, A., *et al.*, 2006, Phys. Rev. Lett. **97**, 235003.
Bourdelle, C., *et al.*, 2007, Phys. Plasmas **14**, 112501.
Buttery, R., *et al.*, 2008, Phys. Plasmas **15**, 056115.
Camenen, Y., *et al.*, 2007, Nucl. Fusion **47**, 510.
Camenen, Y., *et al.*, 2009, Phys. Rev. Lett. **102**, 125001.
Camenen, Y., *et al.*, 2010, Phys. Rev. Lett. **105**, 135003.
Candy, J., *et al.*, 2003, Phys. Rev. Lett. **91**, 045001.
Candy, J., *et al.*, 2004, Phys. Plasmas **11**, 1879.
Candy, J., *et al.*, 2007, Plasma Phys. Controlled Fusion **49**, 1209.
Carrera, R., *et al.*, 1986, Phys. Fluids **29**, 899.

Cary, J., *et al.*, 1983, Ann. Phys. (N.Y.) **151**, 1.
Chang, C., *et al.*, 1986, Phys. Fluids **29**, 3314.
Chang, Z., *et al.*, 1995, Phys. Rev. Lett. **74**, 4663.
Chapman, I., *et al.*, 2011, Plasma Phys. Controlled Fusion **53**, 125002.
Chen, L., *et al.*, 2000, Phys. Plasmas **7**, 3129.
Chen, L., *et al.*, 2007, Nucl. Fusion **47**, S727.
Cheng, C., *et al.*, 1985, Ann. Phys. (N.Y.) **161**, 21.
Cheng, C., *et al.*, 1986, Phys. Fluids **29**, 3695.
Chew, G., *et al.*, 1956, Proc. R. Soc. A **236**, 112.
Chu, M., *et al.*, 1996, Phys. Rev. Lett. **77**, 2710.
Chu, M., *et al.*, 1999, Nucl. Fusion **39**, 2107.
Chu, M., *et al.*, 2004, Phys. Plasmas **11**, 4859.
Chu, M., *et al.*, 2010, Plasma Phys. Controlled Fusion **52**, 123001.
Clark, W., *et al.*, 1980, Phys. Rev. Lett. **45**, 1101.
Coda, S., *et al.*, 2008, *Proceedings of the 22nd IAEA Fusion Energy Conference (Geneva)* (IAEA, Vienna), EX/2.
Cohen, R., *et al.*, 1987, Phys. Fluids **30**, 2442.
Conn, R., *et al.*, 1991, *Proceedings of the 13th International Conference on Plasma Physics and Controlled Nuclear Fusion Research (Washington)* (IAEA, Vienna), Vol. 3, p. 659.
Connor, J., *et al.*, 1978, Phys. Rev. Lett. **40**, 396.
Connor, J., *et al.*, 2000, Plasma Phys. Controlled Fusion **42**, R1.
Conway, G., *et al.*, 2011, Phys. Rev. Lett. **106**, 065001.
Cordey, J., *et al.*, 1976, Nucl. Fusion **16**, 499.
Courant, R. D. H., 1953, *Methods of Mathematical Physics* (Interscience, New York).
Dannert, T., *et al.*, 2005, Phys. Plasmas **12**, 072309.
Degtyarev, L., *et al.*, 1997, Comput. Phys. Commun. **103**, 10.
Dewar, R., *et al.*, 1979, Princeton Plasma Physics Laboratory Report No. PPPL-1587.
Dewar, R., *et al.*, 1981, Nucl. Fusion **21**, 493.
Diamond, P., *et al.*, 1995, Phys. Plasmas **2**, 3640.
Diamond, P., *et al.*, 2005, Plasma Phys. Controlled Fusion **47**, R35.
Diamond, P., *et al.*, 2009, Nucl. Fusion **49**, 045002.
Dimits, A., *et al.*, 2000, Nucl. Fusion **40**, 661.
Dnestrovski, Y., *et al.*, 1988, Nucl. Fusion **28**, 267.
Doerk, H., *et al.*, 2011, Phys. Rev. Lett. **106**, 155003.
Dominguez, R., *et al.*, 1993, Phys. Fluids B **5**, 3876.
Dorland, W., *et al.*, 2000, Phys. Rev. Lett. **85**, 5579.
Doyle, E., *et al.*, 2007, Nucl. Fusion **47**, S18.
Drake, J., *et al.*, 1977, Phys. Fluids **20**, 1341.
Drake, J., *et al.*, 1980, Phys. Rev. Lett. **44**, 994.
Duong, H., *et al.*, 1993, Nucl. Fusion **33**, 749.
Evans, T., *et al.*, 1984, Phys. Rev. Lett. **53**, 1743.
Evans, T., *et al.*, 2005, Nucl. Fusion **45**, 595.
Evans, T., *et al.*, 2008, Nucl. Fusion **48**, 024002.
Fable, E., *et al.*, 2006, Plasma Phys. Controlled Fusion **48**, 1271.
Fable, E., *et al.*, 2008, Plasma Phys. Controlled Fusion **50**, 115005.
Fasoli, A., *et al.*, 1995, Phys. Rev. Lett. **75**, 645.
Ferron, J., *et al.*, 1990, Phys. Fluids B **2**, 1280.
Fisch, N., 1984, Nucl. Fusion **24**, 378.
Fisch, N., *et al.*, 1980, Phys. Rev. Lett. **45**, 720.
Fisch, N., *et al.*, 1987, Rev. Mod. Phys. **59**, 175.
Fitzpatrick, R., *et al.*, 1995, Phys. Plasmas **2**, 825.
Forest, C., *et al.*, 1994, Phys. Rev. Lett. **73**, 2444.
Fowler, R. o., 1979, Oak Ridge National Laboratory Technical Report No. ORNL/TM 5845.
Frieman, E., *et al.*, 1960, Rev. Mod. Phys. **32**, 898.
Fu, G., *et al.*, 1989, Phys. Fluids B **1**, 1949.
Fu, G., *et al.*, 1992, Phys. Fluids B **4**, 3722.
Fujisawa, A., 2009, Nucl. Fusion **49**, 013001.
Fujita, T., *et al.*, 1997a, *Proceedings of the 16th International Conference on Plasma Physics and Controlled Nuclear Fusion Research (Montreal)* (IAEA, Vienna), Vol. 1, p. 227.
Fujita, T., *et al.*, 1997b, Phys. Rev. Lett. **78**, 2377.
Fujita, T., *et al.*, 1998, Nucl. Fusion **38**, 207.
Fujita, T., *et al.*, 2001, Phys. Rev. Lett. **87**, 245001.
Fujita, T., *et al.*, 2005, Phys. Rev. Lett. **95**, 075001.
Fujita, T., *et al.*, 2010, Nucl. Fusion **50**, 113001.
Fukuyama, A., *et al.*, 1997, *Proceedings of the 5th IAEA TCM on Alpha Particles in Fusion Research (Abingdon)* (IAEA, Vienna).
Furth, H., *et al.*, 1963, Phys. Fluids **6**, 459.
Furth, H., *et al.*, 1973, Phys. Fluids **16**, 1054.
Galeev, A., *et al.*, 1971, Sov. Phys. JETP **32**, 752.
Gantenbein, G., *et al.*, 2000, Phys. Rev. Lett. **85**, 1242.
Garbet, X., *et al.*, 1998, Phys. Plasmas **5**, 2836.
Garbet, X., *et al.*, 2001, Phys. Plasmas **8**, 2793.
Garbet, X., *et al.*, 2002, Phys. Plasmas **9**, 3893.
Garbet, X., *et al.*, 2003, Phys. Rev. Lett. **91**, 035001.
Garbet, X., *et al.*, 2004, Plasma Phys. Controlled Fusion **46**, B557.
Garofalo, A., *et al.*, 2007, Nucl. Fusion **47**, 1121.
Garofalo, A., *et al.*, 2008, Phys. Rev. Lett. **101**, 195005.
Gimblett, C., *et al.*, 1986, Nucl. Fusion **26**, 617.
Giruzzi, G., *et al.*, 2003, Phys. Rev. Lett. **91**, 135001.
Glasser, H., *et al.*, 1975, Phys. Fluids **18**, 875.
Goelho, R., *et al.*, 2007, Phys. Plasmas **14**, 012101.
Goldston, R., *et al.*, 1994, Plasma Phys. Controlled Fusion **36**, B213.
Gorelenkov, N., *et al.*, 2003, Nucl. Fusion **43**, 594.
Gorelenkov, N., *et al.*, 2007, Phys. Lett. A **370**, 70.
Gorler, T., *et al.*, 2008a, Phys. Rev. Lett. **100**, 185002.
Gorler, T., *et al.*, 2008b, Phys. Plasmas **15**, 102508.
Gormezano, C., *et al.*, 1999, Nucl. Fusion **39**, 1875.
Gormezano, C., *et al.*, 2004, Plasma Phys. Controlled Fusion **46**, B435.
Gormezano, C., *et al.*, 2007, Nucl. Fusion **47**, S285.
Grimm, R., *et al.*, 1983, J. Comput. Phys. **49**, 94.
Groebner, R., *et al.*, 1986, Nucl. Fusion **26**, 543.
Gruber, R., *et al.*, 1981, Comput. Phys. Commun. **24**, 363.
Guo, S., *et al.*, 1993, Phys. Fluids B **5**, 520.
Gurcan, O., *et al.*, 2007, Phys. Plasmas **14**, 042306.
Gurcan, O., *et al.*, 2008, Phys. Rev. Lett. **100**, 135001.
Guttenfelder, W., *et al.*, 2011, Phys. Rev. Lett. **106**, 155004.
Hahm, T., *et al.*, 1989, Phys. Fluids B **1**, 1185.
Hahm, T., *et al.*, 1994, Phys. Plasmas **1**, 2940.
Hahm, T., *et al.*, 1995, Phys. Plasmas **2**, 1648.
Hahm, T., *et al.*, 2007, Phys. Plasmas **14**, 072302.
Hallatschek, K., *et al.*, 2001, Phys. Rev. Lett. **86**, 1223.
Hamamatsu, K., *et al.*, 2001, Fusion Eng. Des. **53**, 53.
Hameiri, E., *et al.*, 1983, Phys. Fluids **26**, 230.
Hao, G., *et al.*, 2011, Phys. Rev. Lett. **107**, 015001.
Hasegawa, A., *et al.*, 1974, Phys. Rev. Lett. **32**, 454.
Hasegawa, A., *et al.*, 1976, Phys. Fluids **19**, 1924.
Hasegawa, A., *et al.*, 1977, Phys. Rev. Lett. **39**, 205.
Hasegawa, A., *et al.*, 1979, Phys. Fluids **22**, 2122.
Hasegawa, A., *et al.*, 1987, Phys. Rev. Lett. **59**, 1581.
Hastie, R., *et al.*, 1981, Nucl. Fusion **21**, 187.
Hawkes, C., *et al.*, 2001, Phys. Rev. Lett. **87**, 115001.
Hawryluk, R., *et al.*, 1998, Rev. Mod. Phys. **70**, 537.
Hawryluk, R., *et al.*, 2009, Nucl. Fusion **49**, 065012.
Hayashi, N., *et al.*, 2004a, J. Plasma Fusion Res. **80**, 605.
Hayashi, N., *et al.*, 2004b, Nucl. Fusion **44**, 477.
Hayashi, N., *et al.*, 2005, Nucl. Fusion **45**, 933.
Hayashi, N., *et al.*, 2009, Nucl. Fusion **49**, 095015.
Heidbrink, W., *et al.*, 2008, Phys. Plasmas **15**, 055501.
Helander, P., *et al.*, 2001, Phys. Plasmas **8**, 1988.

Helander, P., *et al.*, 2006, Phys. Plasmas **13**, 102506.
Hender, T., *et al.*, 1989, Nucl. Fusion **29**, 1279.
Hinton, F., *et al.*, 1976, Rev. Mod. Phys. **48**, 239.
Hirota, M., *et al.*, 2008, Phys. Plasmas **15**, 122101.
Hirshman, S., 1978, Nucl. Fusion **18**, 917.
Hirshman, S., *et al.*, 1976, Phys. Fluids **19**, 1532.
Hirshman, S., *et al.*, 1977, Phys. Fluids **20**, 418.
Hirshman, S., *et al.*, 1981, Nucl. Fusion **21**, 1079.
Hoang, G., *et al.*, 2001, Phys. Rev. Lett. **87**, 125001.
Hoang, G., *et al.*, 2003, Phys. Rev. Lett. **90**, 155002.
Holcomb, C., *et al.*, 2009, Phys. Plasmas **16**, 056116.
Holland, C., *et al.*, 2004, Phys. Plasmas **11**, 1043.
Honda, M., *et al.*, 2012, Nucl. Fusion **52**, 023021.
Hong, B., *et al.*, 1989, Phys. Fluids B **1**, 1589.
Horton, W., *et al.*, 1999, Rev. Mod. Phys. **71**, 735.
Hoshino, K., *et al.*, 1992, Phys. Rev. Lett. **69**, 2208.
Houlberg, W., *et al.*, 1997, Phys. Plasmas **4**, 3230.
Howl, W., *et al.*, 1992, Phys. Fluids B **4**, 1724.
Hugon, M., *et al.*, 1992, Nucl. Fusion **32**, 33.
Hutchinson, I., *et al.*, 1976, Nucl. Fusion **16**, 447.
Huysmans, G., *et al.*, 2001, Phys. Rev. Lett. **87**, 245002.
Huysmans, G., *et al.*, 2007, Nucl. Fusion **47**, 659.
Hwa, T., *et al.*, 1992, Phys. Rev. A **45**, 7002.
Ida, K., *et al.*, 1995, Phys. Rev. Lett. **74**, 1990.
Ida, K., *et al.*, 1998, Plasma Phys. Controlled Fusion **40**, 1429.
Ida, K., *et al.*, 2008, Phys. Rev. Lett. **101**, 055003.
Ido, T., *et al.*, 2006, Nucl. Fusion **46**, 512.
Idomura, Y., *et al.*, 2000, Phys. Plasmas **7**, 3551.
Idomura, Y., *et al.*, 2003, Nucl. Fusion **43**, 234.
Idomura, Y., *et al.*, 2005, Nucl. Fusion **45**, 1571.
Idomura, Y., *et al.*, 2006, Phys. Plasmas **13**, 080701.
Idomura, Y., *et al.*, 2009, Nucl. Fusion **49**, 065029.
Isayama, A., *et al.*, 2000, Plasma Phys. Controlled Fusion **42**, L37.
Isayama, A., *et al.*, 2007, Nucl. Fusion **47**, 773.
Ishida, S., *et al.*, 1992, Phys. Rev. Lett. **68**, 1531.
Ishida, S., *et al.*, 1997, Phys. Rev. Lett. **79**, 3917.
Ishii, Y., *et al.*, 1998, Plasma Phys. Controlled Fusion **40**, 1607.
Ishii, Y., *et al.*, 2000, Phys. Plasmas **7**, 4477.
Ishii, Y., *et al.*, 2002, Phys. Rev. Lett. **89**, 205002.
Ishii, Y., *et al.*, 2003, Nucl. Fusion **43**, 539.
Ishii, Y., *et al.*, 2009, Nucl. Fusion **49**, 085006.
Ishikawa, M., *et al.*, 2007, Nucl. Fusion **47**, 849.
ITER Physics Expert Group, 1999, Nucl. Fusion **39**, 2175.
Itoh, K., *et al.*, 1996, Plasma Phys. Controlled Fusion **38**, 1.
Janev, R., 1987, *Elementary Processes in Hydrogen-Helium Plasmas, Cross Sections and Reaction Rate Coefficients* (Springer, Berlin).
Janev, R., *et al.*, 1993, *Atomic and Plasma-material Interaction Data for Fusion*, Nucl. Fusion Supplement Vol. 4 (IAEA, Vienna).
Janev, R., *et al.*, 1989, Nucl. Fusion **29**, 2125.
Janvier, X., *et al.*, 2011, Phys. Rev. Lett. **107**, 195001.
Jenko, F., *et al.*, 2000a, Phys. Plasmas **7**, 514.
Jenko, F., *et al.*, 2000b, Phys. Plasmas **7**, 1904.
Jenko, F., *et al.*, 2002, Phys. Rev. Lett. **89**, 225001.
JET team, 1989, *Proceedings of the 12th Conference on Plasma Physics and Controlled Nuclear Fusion Research (Nice)* (IAEA, Vienna), Vol. 1, p. 41.
JET team, 1997, Plasma Phys. Controlled Fusion **39**, B1.
Kadomtsev, B., *et al.*, 1971, Nucl. Fusion **11**, 67.
Kamada, Y., *et al.*, 1992, Phys. Fluids B **4**, 124.
Kamada, Y., *et al.*, 2000, Plasma Phys. Controlled Fusion **42A**, A247.
Keilhacker, M., *et al.*, 2001, Nucl. Fusion **41**, 1925.
Kelliher, D., *et al.*, 2005, Plasma Phys. Controlled Fusion **47**, 1459.
Kennel, C., *et al.*, 1966, Phys. Fluids **9**, 2377.
Kessel, C., *et al.*, 1994, Phys. Rev. Lett. **72**, 1212.
Kikuchi, M., 1990a, Nucl. Fusion **30**, 265.
Kikuchi, M., 1990b, Nucl. Fusion **30**, 343.
Kikuchi, M., 1991, *Proceedings of the 3rd IAEA TM on H-mode Physics* (JET, Culham, UK).
Kikuchi, M., 1993, Plasma Phys. Controlled Fusion **35**, B39.
Kikuchi, M., 2011a, in *38th European Conference on Controlled Fusion and Plasma Physics*, edited by A. Becoulet, T. Hoang, and U. Stroth (European Physical Society, Strasbourg, France), Vol. 35G, p. 4.115.
Kikuchi, M., 2011b, *Frontier in Fusion Research—Physics and Fusion* (Springer, London).
Kikuchi, M., *et al.*, 1991, Fusion Eng. Des. **16**, 253.
Kikuchi, M., *et al.*, 1993, *Proceedings of the 14th International Conference on Plasma Physics and Controlled Nuclear Fusion Research (Wurzburg)* (IAEA, Vienna), Vol. 1, p. 189.
Kikuchi, M., *et al.*, 1995a, *Proceedings of the 15th International Conference on Plasma Physics and Controlled Nuclear Fusion Research (Seville)* (IAEA, Vienna), Vol. 1, p. 31.
Kikuchi, M., *et al.*, 1995b, Plasma Phys. Controlled Fusion **37**, 1215.
Kim, Y. B., 1991, "Neoclassical Poloidal and Toroidal Rotations in Tokamak Plasmas," Sherwood International Fusion Theory Conference, Seattle, WA, 1991.
Kim, Y., *et al.*, 1991, Phys. Fluids B **3**, 2050.
Kimura, H., *et al.*, 1998, Nucl. Fusion **38**, 1303.
Kishimoto, H., *et al.*, 2005, Nucl. Fusion **45**, 986.
Kishimoto, Y., *et al.*, 1996, Phys. Plasmas **3**, 1289.
Kishimoto, Y., *et al.*, 1999, Plasma Phys. Controlled Fusion **40**, A663.
Kittel, C., 1971, *Introduction of Solid State Physics* (Wiley, New York).
Koide, Y., *et al.*, 1994, Phys. Rev. Lett. **72**, 3662.
Koide, Y., *et al.*, 1996, Plasma Phys. Controlled Fusion **38**, 1011.
Koide, Y., *et al.*, 1998a, Plasma Phys. Controlled Fusion **40**, 641.
Koide, Y., *et al.*, 1998b, Plasma Phys. Controlled Fusion **40**, 97.
Kotschenreuther, M., *et al.*, 2000, Nucl. Fusion **40**, 677.
Kramer, G., *et al.*, 1998, Phys. Rev. Lett. **80**, 2594.
Kurita, G., *et al.*, 1994, Nucl. Fusion **34**, 1497.
Kurita, G., *et al.*, 2006, Nucl. Fusion **46**, 383.
Kusama, Y., *et al.*, 1998, Nucl. Fusion **38**, 1215.
Kwon, M., *et al.*, 2011, Nucl. Fusion **51**, 094006.
La Bombard, B., *et al.*, 2004, Nucl. Fusion **44**, 1047.
La Haye, R., *et al.*, 2006, Phys. Plasmas **13**, 055501.
La Haye, R., *et al.*, 2009, Phys. Plasmas **16**, 022107.
La Haye, R., *et al.*, 2010, Phys. Plasmas **17**, 056110.
Lao, L., *et al.*, 2001, Nucl. Fusion **41**, 295.
Lebedev, V., *et al.*, 1997, Phys. Plasmas **4**, 1087.
Lesur, M., *et al.*, 2009, Phys. Plasmas **16**, 092305.
Lesur, M., *et al.*, 2010, Phys. Plasmas **17**, 122311.
Levinton, F., *et al.*, 1995, Phys. Rev. Lett. **75**, 4417.
Li, J., *et al.*, 2011, Nucl. Fusion **51**, 094007.
Liang, Y., *et al.*, 2007, Phys. Rev. Lett. **98**, 265004.
Lilley, M., *et al.*, 2009, Phys. Rev. Lett. **102**, 195003.
Lin, Z., *et al.*, 1998, Science **281**, 1835.
Lin-Liu, Y., *et al.*, 1997, Phys. Plasmas **4**, 4179.
Lin-Liu, Y., *et al.*, 2003, Phys. Plasmas **10**, 4064.
Litaudon, X., *et al.*, 1996, Plasma Phys. Controlled Fusion **38**, 1603.
Loarte, A., *et al.*, 2003, Plasma Phys. Controlled Fusion **45**, 1549.
Luce, T., *et al.*, 2003, Nucl. Fusion **43**, 321.
Mailloux, J., *et al.*, 2002, Phys. Plasmas **9**, 2156.
Manickam, J., *et al.*, 1992, Phys. Fluids B **4**, 1901.

Manickam, J., *et al.*, 1987, Nucl. Fusion **27**, 1461.
Manickam, J., *et al.*, 1994, Phys. Plasmas **1**, 1601.
Manickam, J., *et al.*, 1999, Nucl. Fusion **39**, 1819.
Mantica, P., *et al.*, 2009, Phys. Rev. Lett. **102**, 175002.
Mantica, P., *et al.*, 2011, Phys. Rev. Lett. **107**, 135004.
Marinoni, A., *et al.*, 2009, Plasma Phys. Controlled Fusion **51**, 055016.
Martynov, A., *et al.*, 2003, Phys. Rev. Lett. **91**, 085004.
Matsunaga, G., *et al.*, 2009, Phys. Rev. Lett. **103**, 045001.
McDonald, D., *et al.*, 2008, Plasma Phys. Controlled Fusion **50**, 124013.
McGuire, K., *et al.*, 1988, Plasma Phys. Controlled Fusion **30**, 1391.
Medvedev, S., *et al.*, 2006, Plasma Phys. Controlled Fusion **48**, 927.
Mett, R., *et al.*, 1992, Phys. Fluids B **4**, 2885.
Miki, K., *et al.*, 2007, Phys. Rev. Lett. **99**, 145003.
Miyato, N., *et al.*, 2004, Phys. Plasmas **11**, 5557.
Miyato, N., *et al.*, 2005, Nucl. Fusion **45**, 425.
Miyato, N., *et al.*, 2007, Nucl. Fusion **47**, 929.
Murakami, M., *et al.*, 1979, Phys. Rev. Lett. **42**, 655.
Murakami, M., *et al.*, 2006, Phys. Plasmas **13**, 056106.
Nagashima, K., *et al.*, 1994, Nucl. Fusion **34**, 449.
Nagashima, K., *et al.*, 1995, Nucl. Fusion **35**, 994.
Najmabadi, F., *et al.*, 1998, Fusion Eng. Des. **41**, 365.
Nazikian, R., *et al.*, 1997, Phys. Rev. Lett. **78**, 2976.
Nazikian, R., *et al.*, 2003, Phys. Rev. Lett. **91**, 125003.
Nazikian, R., *et al.*, 2005, Phys. Rev. Lett. **94**, 135002.
Newcomb, W., *et al.*, 1960, Ann. Phys. (N.Y.) **10**, 232.
Ohkawa, T., 1976, General Atomics Technical Report No. GA-A 13847.
Oikawa, T., *et al.*, 2000, Nucl. Fusion **40**, 435.
Oikawa, T., *et al.*, 2001, Nucl. Fusion **41**, 1575.
Oikawa, T., *et al.*, 2005, Nucl. Fusion **45**, 1101.
Okano, K., *et al.*, 1998, Fusion Eng. Des. **41**, 511.
Oyama, N., *et al.*, 2007, Plasma Phys. Controlled Fusion **49**, 249.
Ozeki, T., *et al.*, 1993a, *Proceedings of the 14th International Conference on Plasma Physics and Controlled Nuclear Fusion Research (Wurzburg)* (IAEA, Vienna), Vol. 2, p. 187.
Ozeki, T., *et al.*, 1993b, Nucl. Fusion **33**, 1025.
Ozeki, T., *et al.*, 1995, Nucl. Fusion **35**, 861.
Ozeki, T., *et al.*, 2003a, Plasma Phys. Controlled Fusion **45**, 645.
Ozeki, T., *et al.*, 2003b, in *Proceedings of the 30th European Conference on Controlled Fusion and Plasma Physics*, edited by R. Koch and S. Lebedev (European Physical Society, St. Petersburg, Russia), Vol. 27A, p. 2.111.
Pankin, A., *et al.*, 2004, Comput. Phys. Commun. **159**, 157.
Parker, S., *et al.*, 1993, Phys. Rev. Lett. **71**, 2042.
Peeters, A., *et al.*, 2007, Phys. Rev. Lett. **98**, 265003.
Pereverzev, G., *et al.*, 1991, Max Planck Institute for Plasma Physics Report No. IPP 5/42.
Pereverzev, G., *et al.*, 2005, Nucl. Fusion **45**, 221.
Petty, C., *et al.*, 2002, Nucl. Fusion **42**, 1366.
Petty, C., *et al.*, 2003, Nucl. Fusion **43**, 700.
Pietrzyk, Z., *et al.*, 2001, Phys. Rev. Lett. **86**, 1530.
Pletzer, A., *et al.*, 1991, J. Plasma Phys. **45**, 427.
Poincaré, H., 1885, Sur les courbes définies par uné equation différentielle, J. de Math. Pures et Appl., Série IV 1, p. 167.
Polevoi, A., *et al.*, 2010, in *Proceedings of the 37th European Conference on Controlled Fusion and Plasma Physics*, edited by C. McKenna (European Physical Society, Dublin, Ireland), Vol. 34A, p. 2.187.
Prater, R., *et al.*, 2004, Phys. Plasmas **11**, 2349.
Pritchett, P., *et al.*, 1980, Phys. Fluids **23**, 1368.
Pueschel, M., *et al.*, 2008, Phys. Plasmas **15**, 102310.
Pueschel, M., *et al.*, 2010, Phys. Plasmas **17**, 062307.
Ramos, J., 1991, Phys. Fluids B **3**, 2247.
Reimerdes, H., *et al.*, 2007, Phys. Rev. Lett. **98**, 055001.
Rewoldt, G., *et al.*, 2007, Comput. Phys. Commun. **177**, 775.
Rhines, P., 1975, J. Fluid Mech. **69**, 417.
Rice, J., *et al.*, 1997, Nucl. Fusion **37**, 421.
Rice, J., *et al.*, 2007, Nucl. Fusion **47**, 1618.
Rice, J., *et al.*, 2011, Phys. Rev. Lett. **106**, 215001.
Richester, A., *et al.*, 1978, Phys. Rev. Lett. **40**, 38.
Riviere, A., *et al.*, 1971, Nucl. Fusion **11**, 363.
Robinson, D., *et al.*, 1979, Nucl. Fusion **19**, 115.
Rodrigues, P., *et al.*, 2005, Phys. Rev. Lett. **95**, 015001.
Rodrigues, P., *et al.*, 2007, Phys. Rev. Lett. **99**, 125001.
Romanelli, F., *et al.*, 1989, Phys. Fluids B **1**, 1018.
Romanelli, F., *et al.*, 1993, Phys. Fluids B **5**, 4081.
Rosenbluth, M., *et al.*, 1971, Phys. Fluids **14**, 1725.
Rosenbluth, M., *et al.*, 1998, Phys. Rev. Lett. **80**, 724.
Rutherford, P., *et al.*, 1973, Phys. Fluids **16**, 1903.
Ryter, F., *et al.*, 2005, Phys. Rev. Lett. **95**, 085001.
Sabbagh, S., *et al.*, 2006, Phys. Rev. Lett. **97**, 045004.
Sakamoto, K., *et al.*, 2007, Nat. Phys. **3**, 411.
Sakamoto, Y., *et al.*, 2001, Nucl. Fusion **41**, 865.
Sakamoto, Y., *et al.*, 2004, Nucl. Fusion **44**, 876.
Sakamoto, Y., *et al.*, 2005, Nucl. Fusion **45**, 574.
Sakamoto, Y., *et al.*, 2009, Nucl. Fusion **49**, 095017.
Sauter, O., *et al.*, 1997, Phys. Plasmas **4**, 1654.
Sauter, O., *et al.*, 1999, Phys. Plasmas **6**, 2834.
Sauter, O., *et al.*, 2000, Phys. Rev. Lett. **84**, 3322.
Sauter, O., *et al.*, 2002, Plasma Phys. Controlled Fusion **44**, 1999.
Sauter, O., *et al.*, 2005, Phys. Rev. Lett. **94**, 105002.
Sauter, O., *et al.*, 2010, Plasma Phys. Controlled Fusion **52**, 025002.
Sauthoff, N., *et al.*, 1978, Nucl. Fusion **18**, 1445.
Scarabosio, A., *et al.*, 2006, Plasma Phys. Controlled Fusion **48**, 663.
Scott, B., 2003, Phys. Lett. A **320**, 53.
Scott, B., *et al.*, 2010, Phys. Plasmas **17**, 112302.
Sedlacek, Z., 1971, J. Plasma Phys. **5**, 239.
Seki, S., *et al.*, 1987, Nucl. Fusion **27**, 330.
Seki, Y., *et al.*, 1991a, *Proceedings of the 13th International Conference on Plasma Physics and Controlled Nuclear Fusion Research (Washington)* (IAEA, Vienna), Vol. 3, p. 473.
Seki, Y., *et al.*, 1991b, Fusion Reactor System Laboratory, Japan Atomic Energy Research Institute Technical Report No. JAERI-M 91-081, http://jolissrch-inter.tokai-sc.jaea.go.jp.pdfdata/JAERI-M-91-081.pdf.
Shafranov, V., 1958, Sov. Phys. JETP **6**, 545.
Shaing, K., *et al.*, 1983, Phys. Fluids **26**, 3315.
Shaing, K., *et al.*, 1996, Phys. Plasmas **3**, 965.
Shaing, K., *et al.*, 1997, Phys. Rev. Lett. **79**, 3652.
Shaing, K., *et al.*, 2003, Phys. Plasmas **10**, 1443.
Sharapov, S., *et al.*, 2001, Phys. Lett. A **289**, 127.
Shinohara, K., *et al.*, 2001, Nucl. Fusion **41**, 603.
Shirai, H., *et al.*, 1999, Nucl. Fusion **39**, 1713.
Shirai, H., *et al.*, 2000, Plasma Phys. Controlled Fusion **42**, A109.
Shiraishi, J., *et al.*, 2011, Nucl. Fusion **51**, 053006.
Sips, A., *et al.*, 2002, Plasma Phys. Controlled Fusion **44**, B69.
Smolyakov, A., *et al.*, 2001, Plasma Phys. Controlled Fusion **43**, 1661.
Snyder, P., *et al.*, 2001, Phys. Plasmas **8**, 744.
Snyder, P., *et al.*, 2002, Phys. Plasmas **9**, 2037.
Snyder, P., *et al.*, 2009, Nucl. Fusion **49**, 085035.
Snyder, R., *et al.*, 2007, Nucl. Fusion **47**, 961.
Solomon, W., *et al.*, 2007, Plasma Phys. Controlled Fusion **49**, B313.

Spitzer, L., 1962, *Physics of Fully Ionized Gases* (Interscience, New York).
Staebler, G., *et al.*, 2005, Phys. Plasmas **12**, 102508.
Stambaugh, R., *et al.*, 1985, *Proceedings of the 10th International Conference on Plasma Physics and Controlled Nuclear Fusion Research (London)* (IAEA, Vienna), Vol. 1, p. 217.
Stambaugh, R., *et al.*, 1995, *Proceedings of the 15th International Conference on Plasma Physics and Controlled Nuclear Fusion Research (Seville)* (IAEA, Vienna), Vol. 1, p. 83.
Start, D., *et al.*, 1980, Phys. Fluids **23**, 1477.
Stix, T., 1962, *The Theory of Plasma Waves* (McGraw-Hill, New York).
Stix, T., *et al.*, 1972, Plasma Phys. **14**, 367.
Stix, T., *et al.*, 1976, Phys. Rev. Lett. **36**, 521.
Strachan, J., *et al.*, 1987, Phys. Rev. Lett. **58**, 1004.
Strait, E., *et al.*, 1995, Phys. Rev. Lett. **75**, 4421.
Suttrop, W., *et al.*, 2011, Phys. Rev. Lett. **106**, 225004.
Suzuki, S., *et al.*, 1998, Plasma Phys. Controlled Fusion **40**, 2097.
Suzuki, T., *et al.*, 2004a, Nucl. Fusion **44**, 699.
Suzuki, T., *et al.*, 2004b, J. Plasma Fusion Res. **80**, 511.
Suzuki, T., *et al.*, 2011, Nucl. Fusion **51**, 083020.
Taguchi, M., 1983, J. Phys. Soc. Jpn. **52**, 2035.
Taguchi, M., *et al.*, 1989, Plasma Phys. Controlled Fusion **31**, 241.
Takase, Y., *et al.*, 2006, *Proceedings of the 21st IAEA Fusion Energy Conference (Chengdu)* (IAEA, Vienna), EX/1.
Takechi, M., *et al.*, 2005, Phys. Plasmas **12**, 082509.
Takechi, M., *et al.*, 2007, Phys. Rev. Lett. **98**, 055002.
Takeji, S., *et al.*, 1997, Phys. Plasmas **4**, 4283.
Takeji, S., *et al.*, 2002a, Nucl. Fusion **42**, 5.
Takeji, S., *et al.*, 2002b, Fusion Sci. Technol. **42**, 278 [http://www.new.ans.org/pubs/journals/fst/a_229].
Takizuka, T., 2002, J. Plasma Fusion Res. **78**, 1282.
Takizuka, T., *et al.*, 2002, Plasma Phys. Controlled Fusion **44**, A423.
Takizuka, T., *et al.*, 2006, Plasma Phys. Controlled Fusion **48**, 799.
Tang, W., *et al.*, 1978, Nucl. Fusion **18**, 1089.
Tang, W., *et al.*, 1980, Nucl. Fusion **20**, 1439.
Tang, W., *et al.*, 1982, Nucl. Fusion **22**, 1079.
Tani, K., *et al.*, 1992, J. Comput. Phys. **98**, 332.
Taylor, T., *et al.*, 1993, *Proceedings of the 14th International Conference on Plasma Physics and Controlled Nuclear Fusion Research (Wurzburg)* (IAEA, Vienna), Vol. 1, p. 167.
Taylor, T., *et al.*, 1997, Plasma Phys. Controlled Fusion **39**, B47.
Terry, F., *et al.*, 2000, Rev. Mod. Phys. **72**, 109.
Tokuda, S., *et al.*, 1997, J. Plasma Fusion Res. **73**, 1141 [http://ci.nii.ac.jp/naid/110003826781/].
Tokuda, S., *et al.*, 1999, Phys. Plasmas **6**, 3012.
Troyon, F., *et al.*, 1984, Plasma Phys. Controlled Fusion **26**, 209.
Tsang, K., *et al.*, 1976, Phys. Fluids **19**, 667.
Turnbull, A., *et al.*, 1998, Nucl. Fusion **38**, 1467.
Turri, G., *et al.*, 2008, Plasma Phys. Controlled Fusion **50**, 065010.
Uberoi, C., *et al.*, 1972, Phys. Fluids **15**, 1673.
Ueda, N., *et al.*, 1992, Nucl. Fusion **32**, 1037.
Urano, H., *et al.*, 2006, Nucl. Fusion **46**, 781.
Urano, H., *et al.*, 2008, Nucl. Fusion **48**, 045008.
van Houtte, D., *et al.*, 2004, Nucl. Fusion **44**, L11.
Vermale, L., *et al.*, 2007, Nucl. Fusion **47**, 490.
Wade, M., *et al.*, 2004, Phys. Rev. Lett. **92**, 235005.
Waelbloeck, F., *et al.*, 2001, Phys. Rev. Lett. **87**, 215003.
Wagner, F., *et al.*, 1982, Phys. Rev. Lett. **49**, 1408.
Waltz, R., *et al.*, 1994, Phys. Plasmas **1**, 2229.
Waltz, R., *et al.*, 1995, Phys. Plasmas **2**, 2408.
Wang, J., *et al.*, 1994, Nucl. Fusion **34**, 231.
Wang, S., *et al.*, 2004, Phys. Rev. Lett. **93**, 155007.
Wang, W., *et al.*, 2010, Phys. Plasmas **17**, 072511.
Wang, W., *et al.*, 2011, Phys. Plasmas **18**, 042502.
Wang, Z. X., *et al.*, 2007, Phys. Rev. Lett. **99**, 185004.
Ware, A., *et al.*, 1970, Phys. Rev. Lett. **25**, 916.
Weisen, H., *et al.*, 1989, Phys. Rev. Lett. **63**, 2476.
White, R., *et al.*, 1995, Phys. Plasmas **2**, 2871.
Wilson, H., *et al.*, 2002, Phys. Plasmas **9**, 1277.
Winsor, N., *et al.*, 1968, Phys. Fluids **11**, 2448.
Wolf, R., *et al.*, 2003, Plasma Phys. Controlled Fusion **45**, R1.
Wong, K., *et al.*, 1991, Phys. Rev. Lett. **66**, 1874.
Wong, K., *et al.*, 1999, Plasma Phys. Controlled Fusion **41**, R1.
Yamada, T., *et al.*, 2008, Nat. Phys. **4**, 721 [http://www.nature.com/nphys/journal/v4/n9/full/nphys1029.html].
Yancov, V., 1994, JETP Lett. **60**, 171.
Yoshida, M., *et al.*, 2008, Phys. Rev. Lett. **100**, 105002.
Yoshioka, Y., *et al.*, 1984, Nucl. Fusion **24**, 565.
Yoshizawa, A., *et al.*, 2001, Plasma Phys. Controlled Fusion **43**, R1.
Zakharov, L., *et al.*, 1979, *Proceedings of the 7th International Conference on Plasma Physics and Controlled Nuclear Fusion Research (Innsbruck)* (IAEA, Vienna), Vol. 1, p. 689.
Zarnstorff, M., *et al.*, 1984, Phys. Rev. Lett. **53**, 454.
Zarnstorff, M., *et al.*, 1988, Phys. Rev. Lett. **60**, 1306.
Zarnstorff, M., *et al.*, 1989, *Proceedings of the 12th International Conference on Plasma Physics and Controlled Nuclear Fusion Research (Nice)* (IAEA, Vienna), Vol. 1, p. 183.
Zarnstorff, M., *et al.*, 1990, Phys. Fluids B **2**, 1852.
Zehrfeld, H., *et al.*, 1972, Nucl. Fusion **12**, 569.
Zhu, W., *et al.*, 2006, Phys. Rev. Lett. **96**, 225002.
Zonca, C., *et al.*, 1992, Phys. Rev. Lett. **68**, 592.